Quality Assurance of CsI(Tl) Crystals for the BABAR Electromagnetic Calorimeter, and a Monte Carlo Study of the CP-Violating Channel $B^0 \to \pi^+\pi^-\pi^0$ for the BABAR Detector

Theresa J. Champion

A thesis submitted for the degree of Doctor of Philosophy
at Brunel University, June 1999.

Abstract

The BABAR high energy physics experiment has been designed to study CP violation in the neutral B meson system. Data-taking began at the $PEP\text{-}II$ asymmetric e^+e^- collider in Spring 1999. The B-physics program for BABAR involves the reconstruction of the wide range of exclusive final states needed for CP studies. This places stringent requirements on the performance of the detector. Since many of the modes of interest include $\pi^0 s$, it is essential to achieve excellent energy and position resolution for the CsI(Tl) electromagnetic calorimeter.

CsI(Tl) crystals for the BABAR electromagnetic calorimeter were supplied by several manufacturing companies. Collaborative work was undertaken with one of these companies, Hilger Crystal Materials, to ensure that the crystals met the high specifications required by BABAR. A new production process was established in order to generate the large size and number of CsI(Tl) crystals needed. The resulting change of scale (larger furnaces, extended growth/cooling periods, increased mass/material handling) presented considerable challenges for all aspects of the production environment in order to achieve the necessary production rate and quality of crystals. The existing working practices were assessed and redesigned to suite the BABAR crystal production.

A new purpose-built quality assurance (QA) testing laboratory at Hilger was created, where the trapezoidal crystals were to be precisely dimensioned, tuned for light output, and wrapped. Specialised QA instrumentation was needed for BABAR crystals, and this was built locally, based on a design from SLAC. The operational procedures for quality assurance were established, and new staff were trained in these procedures. The unique characteristics of Hilger crystals required the careful design of tuning methods to optimise light uniformity and overall light yield. Detailed studies of factors affecting crystal properties were carried out, including effects of furnace temperature gradients on growth rate and structural defects, and lattice orientation and distortion in seeds.

The first analysis of the $B^0 \to \pi^+\pi^-\pi^0$ channel using fully reconstructed Monte Carlo events has been carried out. The channel is a rare decay, with an estimated branching ratio of $\sim 10^{-5}$. Theoretical models indicate that it will play a central role in the determination of the CP angle α. However, the backgrounds for α channels ($2\pi, 3\pi, 4\pi$) are expected to be high from continuum events, and so the usefulness of $B^0 \to \pi^+\pi^-\pi^0$ for CP studies will be largely determined by the level of background suppression which can be achieved. Methods for reducing the background contamination were developed, and a set of tools were designed for this purpose. The tools make use of a large number of discriminating variables, and employ several multivariate analysis techniques in order to optimise discriminating power. The background-fighting procedure can be applied directly to any analysis within the BABAR software environment. The essential information which must be extracted from selected events is the Δz distribution which represents the difference in the decay time distributions of the B^0 and $\overline{B}^0$. In order to obtain a good resolution on Δz, a detailed study of methods for vertexing the B candidates was performed. Finally, a fit to the CP angle α was carried out for the $B^0 \to \pi^+\pi^-\pi^0$ channel using the two-body analysis of $B^0 \to \rho\pi$ modes.

Acknowledgments

There are many people who have contributed to the successful completion of this work through their valued support and advice. I wish to offer my sincere thanks to the following:

My supervisor, Adrian McKemey, whose enthusiasm and unique style of supervision I have come to appreciate greatly over the years, and my second supervisor, Peter Hobson, for his unwavering reliability.

This work would not have been possible without the steadfast support and invaluable advice of Paul Harrison, who provided insight and inspiration to explore the wonders of physics. I offer him my deepest gratitude.

The financial support for this work was provided by PPARC, and was administered with consideration and patience beyond the call of duty by Maggie Biltcliffe and Ravi Rathod. I was fortunate that my PPARC studentship included a CASE award, with Hilger Crystal Materials. Working with Hilger was an interesting and enlightening experience.

For the 3π analysis I have particularly enjoyed the rewarding collaboration which developed with Sophie Versillé and François LeDiberder, and also the many stimulating interactions with Art Snyder and Helen Quinn.

For their cheerful willingness to help with technical issues, I am indebted to Jane Tinslay for all the filtering, to Georges Vasseur for his fortran expertise, and to Sabah Salih for his help at Brunel.

In recent months, I have appreciated the efforts of Chris Hawkes, Dave Aston, Ben Brau and Charlie Young to ease my commitments during the completion of this work.

I wish to thank all my friends for their companionship and support, especially Pom, Susan, Gabriella and Masahiro.

Finally, to my Mum, who has been totally dependable and unconditionally supportive throughout all my studies - thank you.

Contents

List of Figures

List of Tables

1

CP Violation in the B Meson System

1.1 Introduction

CP violation was first observed in the decays of neutral K mesons, by Christenson *et al.*, in 1964 [1], where it was shown that both long-lived and short-lived kaon states decayed to the CP-even $\pi^+\pi^-$ state. Since that time, a well-formulated theory [2] has been developed which offers the prospect of many possible tests of CP violation.

In the field theory description, CP violation is accommodated by terms in the Lagrangian which are asymmetric under a CP transformation, where the complex coupling constants cannot be removed by any phase redefinitions. These terms originate in the weak sector. CPT is taken to be a good symmetry in the Standard Model, under the assumptions of locality and Lorentz-invariance in field theories. One consequence of CPT conservation is that particles and their antiparticles should have the same mass and lifetime, and this is well supported by experimental observations [3].

1.1.1 The Importance of CP Violation

The most striking observation of an asymmetry between matter and antimatter is that the Universe is essentially made of matter (the baryon:antibaryon ratio being $\sim 10^9$)[4]. Physicists are reluctant to account for this imbalance through a carefully selected set of initial conditions for the big bang, although that is one possible explanation. It is

more feasible, however, that the Universe was initially matter-antimatter symmetric, and that the imbalance developed through some physical processes which have yet to be established.

CP violation provides a possible mechanism to account for some or all of the matter/ antimatter imbalance in the Universe. In 1967, Sakharov [5] stated that, in order for the imbalance to occur, the following conditions must have been met simultaneously at some stage in the evolution of the Universe :

1. A baryon number violating process – so that net universal baryon number can change, since, if baryon number (B) were an exact symmetry of nature, the present baryon asymmetry must simply reflect initial conditions.
2. CP violation – so that (1.) proceeds differently for baryons and antibaryons, since B is odd under C and CP, any change in B requires C and CP non-invariance.
3. The Universe out of thermal equilibrium – so that the rates of baryon production and annihilation are not balanced, since B is also odd under T, and non-equilibrium conditions are necessary to break T invariance by providing an arrow of time.

This argument indicates that CP violation has important cosmological significance. However, the source of CP violation in the Standard Model is not large enough to account fully for the universal matter/antimatter asymmetry, which suggests there may be other sources of CP violation beyond the Standard Model [6].

Within the Standard Model, CP violation is related to some of the most fundamental questions facing present understanding. CP violation enters the Standard Model through a single parameter, a phase in the CKM matrix. The CKM phase is one of the least constrained parameters in the Standard Model. Many observables are dependent on this parameter, so a desirable experimental situation exists in which many independent tests are possible. This can provide an over-determination of the Standard Model which, in

turn, allows checks to be made for inconsistencies. It is the aim of BABAR to carry out such an experimental program by studying CP-violating effects in the B system.

The CKM matrix itself is related to the mechanism through which fermions acquire mass in the Standard Model, and to the existence of three generations of fermions [7]. A better understanding of CP violation in the Standard Model may therefore provide some insight into these issues. Furthermore, it is not difficult to extend the Standard Model to accommodate new sources of CP violation; all that is required is that any new terms in the Lagrangian are not constrained to be CP symmetric.

1.1.2 The Origin of *CP* Violation

CP violation is a purely quantum mechanical effect which will occur in any process in which interference takes place between different amplitudes for the same process. The necessary and sufficient conditions for CP violating process are that two or more intermediate states must exist, whose amplitudes transform under the CP operation, and have non-zero relative phase [8]. There are three situations for which these conditions can be met :

- Direct CP violation – in decay, if a process and its CP conjugate have different amplitudes,
- Indirect CP violation – in the mixing of neutral mesons when the mass eigenstates of a neutral meson system are not equal to CP eigenstates,
- CP violation in the interference between decay and mixing – in decays to final states common to a meson and antimeson.

Direct CP violation effects are expected in a number of charged meson (K, B and D) decays, but it would be hard to extract information about the weak phase from them. Indirect CP violation occurs in the mixing of neutral mesons, K, B and D. In the B system,

the combination of large $B^0\overline{B}^0$ mixing [9], and the long half-life compared to mixing time [10],[11], offers experimental opportunities for measuring significant asymmetries.

1.2 *CP* Violation in Decay

The simplest experimental consequence of a CP-violating process is that the decay rates of a particle to some final state f, and its antiparticle to the CP conjugate state $\overline{f}$ should be different. So for B mesons, CP violation would imply,

$$A_f = \langle f|\mathcal{H}|B\rangle \neq \overline{A}_{\overline{f}} = \langle \overline{f}|\mathcal{H}|\overline{B}\rangle, \tag{1.1}$$

and hence,

$$\left|\frac{\overline{A}_{\overline{f}}}{A_f}\right| \neq 1 \quad \text{or} \quad |A_f|^2 \neq |\overline{A}_{\overline{f}}|^2. \tag{1.2}$$

The action of the CP operator on the states $|B>$ and $|f>$ is defined by,

$$CP|B\rangle = e^{2i(\xi_B)}|\overline{B}\rangle, \tag{1.3}$$

$$CP|f\rangle = e^{2i(\xi_f)}|\overline{f}\rangle, \tag{1.4}$$

where $e^{2i(\xi_B)}$ and $e^{2i(\xi_f)}$ are the intrinsic phase factors associated with the states $|B>$ and $|f>$ respectively [12].

In the Standard Model, a single amplitude A differs from its CP conjugate amplitude $\overline{A}$ only by a phase factor, which would not result in an observable CP asymmetry. If several amplitudes contribute to $B \to f$, each with an overall CP-violating phase, then the total amplitude is a linear superposition of the sub-amplitudes,

$$A_f = \sum_i A_i e^{i(\delta_i+\phi_i)}, \tag{1.5}$$

$$\overline{A}_{\overline{f}} = e^{2i(\xi_f-\xi_B)} \sum_i A_i e^{i(\delta_i-\phi_i)}. \tag{1.6}$$

where ϕ_i are phases which change sign under CP transformation, *i.e.,* weak phases from the CKM matrix, and δ_i are non-CP-violating phases, such as those arising from final state

strong interactions. The term $e^{2i(\xi_f - \xi_B)}$ allows for the phase freedom described above, and therefore has no observable effect. Now the ratio of the amplitudes becomes,

$$\left|\frac{\overline{A}_{\overline{f}}}{A_f}\right| = \left|\frac{\sum_i A_i e^{i(\delta_i - \phi_i)}}{\sum_i A_i e^{i(\delta_i + \phi_i)}}\right|, \tag{1.7}$$

and the difference in the amplitudes is given by,

$$|A_f|^2 - |\overline{A}_{\overline{f}}|^2 = -2\sum_{i,j} A_i A_j \sin(\phi_i - \phi_j)\sin(\delta_i - \delta_j). \tag{1.8}$$

This expression summarises clearly the three conditions for CP violation to occur (see section 1.2.1). For the difference in amplitudes to be non-zero, there must be differences between the ϕ_i phases, and also between the δ_i phases.

Direct CP violation is expected to occur in both charged and neutral B decays, and is indicated by a non-zero asymmetry between the measured rates for a decay and its CP conjugate, *e.g.*, for charged B decays,

$$a_f = \frac{\Gamma(B^+ \to f) - \Gamma(B^- \to \overline{f})}{\Gamma(B^+ \to f) + \Gamma(B^- \to \overline{f})} \neq 0. \tag{1.9}$$

For neutral B decays $a_f \neq 0$ cannot unambiguously be attributed to CP violation in decay, since it competes with the two other types of CP violating effects.

In B decays, purely leptonic and semileptonic channels are dominated by a single term, so are unlikely to exhibit any measurable direct CP violation. Non-leptonic decays often have two terms (tree + penguin), so could exhibit significant direct CP violation, but it is very difficult to have a clean relationship between measured asymmetries and CKM phases. Strong phase shifts and absolute values of various amplitudes are model dependent (long distance physics).

1.3 *CP* Violation in Neutral Meson Mixing

Neutral pseudoscalar mesons, which consist of self-conjugate quark pairs, exhibit spontaneous oscillation between particle and antiparticle states. This phenomenon provides a mechanism for producing interfering amplitudes, and thus offers conditions with the potential for CP violation to occur. The size of mixing effects varies greatly in different meson systems, with $B^0\overline{B}^0$ providing the most promising area for study. Substantial effects have been observed for both $K^0\overline{K^0}$ and $B^0\overline{B}^0$, but to date no mixing has been seen in the $D^0\overline{D}^0$ system, where the effects are expected to be small[1].

The formalism for mixing in the neutral kaon system is the same as that for the neutral B mesons, except for the distinction that the kaon eigenstates differ markedly in lifetime, while the B eigenstates have similar lifetimes. The formalism for mixing is shown below with reference to the B system.

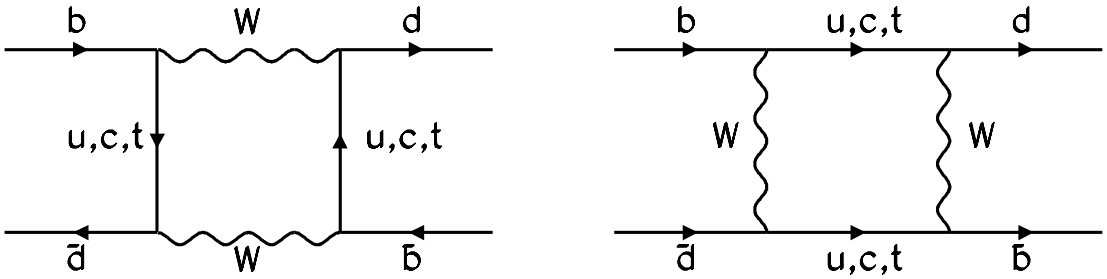

Figure 1-1. *Box diagrams for $B^0\overline{B}^0$ mixing.*

In the B rest frame, the time evolution of basis states B^0 and $\overline{B}^0$, is governed by,

$$i\frac{d}{dt}\begin{pmatrix} B^0 \\ \overline{B}^0 \end{pmatrix} = \mathcal{H}\begin{pmatrix} B^0 \\ \overline{B}^0 \end{pmatrix} \equiv \begin{pmatrix} \mathcal{H}_{11} & \mathcal{H}_{12} \\ \mathcal{H}_{21} & \mathcal{H}_{22} \end{pmatrix}\begin{pmatrix} B^0 \\ \overline{B}^0 \end{pmatrix} \equiv (\mathcal{M} - \frac{i}{2}\Gamma)\begin{pmatrix} B^0 \\ \overline{B}^0 \end{pmatrix} \qquad (1.10)$$

[1]The size of the the *CP* effect depends inversely on the width of the process under study, which for D mesons is Cabbibo allowed, ($c \to s$) and therefore large.

Here, the effective Hamiltonian is a non-Hermitian matrix, as only a subset of final states, which are common to both B^0 and $\overline{B}^0$, is being considered. $\mathcal{M}$ and Γ, however, are Hermitian, and are the mass and decay matrices respectively. CPT invariance constrains the masses and lifetimes of the particles to be the same, so that $\mathcal{M}_{11} = \mathcal{M}_{22}$ and $\Gamma_{11} = \Gamma_{22}$.

The eigenstates and eigenvalues of $\mathcal{H}$ can then be found by rewriting the Hamiltonian in the form,

$$\mathcal{H} = \mathcal{H}_{11} I + \begin{pmatrix} 0 & \mathcal{H}_{12} \\ \mathcal{H}_{21} & 0 \end{pmatrix}. \tag{1.11}$$

Expressing the eigenvectors in the form,

$$|B_L^0\rangle = p|B^0\rangle + q|\overline{B}^0\rangle\,, \tag{1.12}$$

$$|B_H^0\rangle = p|B^0\rangle - q|\overline{B}^0\rangle\,, \tag{1.13}$$

where q and p are complex, and $|q|^2 + |p|^2 = 1$ for normalisation,

and solving the eigenvalue equation,

$$\begin{pmatrix} 0 & \mathcal{H}_{12} \\ \mathcal{H}_{21} & 0 \end{pmatrix} \begin{pmatrix} p \\ q \end{pmatrix} = \mu \begin{pmatrix} p \\ q \end{pmatrix} \tag{1.14}$$

gives,

$$\left(\frac{q}{p}\right)^2 = \left(\frac{\mathcal{H}_{21}}{\mathcal{H}_{12}}\right) \quad , \quad \mu^2 = \mathcal{H}_{12}\mathcal{H}_{21}\,. \tag{1.15}$$

If CP is conserved, then q/p is a pure phase factor. So the condition for CP violation in mixing is then,

$$\left|\frac{q}{p}\right|^2 = \left|\frac{\mathcal{H}_{21}}{\mathcal{H}_{12}}\right| = \left|\frac{M_{12}^* - \frac{i}{2}\Gamma_{12}^*}{M_{12} - \frac{i}{2}\Gamma_{12}}\right| \neq 1\,. \tag{1.16}$$

CP violation in the neutral kaon system has already been measured in semileptonic kaon decays:

$$a_K(\ell) = \frac{\Gamma(K_L^0 \to \pi^-\ell^+\nu_\ell) - \Gamma(\overline{K}_L^0 \to \pi^+\ell^-\overline{\nu}_\ell)}{\Gamma(K_L^0 \to \pi^-\ell^+\nu_\ell) + \Gamma(\overline{K}_L^0 \to \pi^+\ell^-\overline{\nu}_\ell)}, \tag{1.17}$$

$$a_K(\mu) = (3.04 \pm 0.25) \times 10^{-3}, \quad a_K(e) = (3.33 \pm 0.14) \times 10^{-3}\,. \tag{1.18}$$

The experimental result is entirely consistent with CP violation due to mixing alone.

1.4 *CP* Violation in the Interference between Decay and Mixing

The most promising area for observing a large CP asymmetry in the B system is expected to be in the interference between decay and mixing, where amplitudes are comparable in magnitude. This situation occurs in decays into final states which are common to B^0 and $\overline{B}^0$,

$$B^0_{\rm phys} \;\to\; f\,, \tag{1.19}$$

$$\overline{B}^0_{\rm phys} \;\to\; B^0_{\rm phys} \to f\,, \tag{1.20}$$

where the notation $B^0_{\rm phys}(\overline{B}^0_{\rm phys})$ denotes an initially pure $B^0(\overline{B}^0)$ state.

The decay amplitudes for these processes are defined, respectively, by,

$$A_f = \langle f|H|B^0_{\rm phys}\rangle\,, \tag{1.21}$$

$$\overline{A}_f = \langle f|H|\overline{B}^0_{\rm phys}\rangle\,. \tag{1.22}$$

Squaring the modulus of each amplitude gives the corresponding decay rate,

$$\begin{aligned} R_{B^0_{\rm phys}} &= |\langle f|H|B^0_{\rm phys}\rangle|^2 \\ &= e^{-\Gamma t}|A|^2\{1+|\lambda_f|^2+(1-|\lambda_f|^2)\,\cos(\Delta m_B t) - 2\,\mathcal{I}m\,\lambda_f\,\sin(\Delta m_B t)\}, \end{aligned} \tag{1.23}$$

$$\begin{aligned} R_{\overline{B}^0_{\rm phys}} &= |\langle f|H|\overline{B}^0_{\rm phys}\rangle|^2 \\ &= e^{-\Gamma t}|A|^2\{1+|\lambda_f|^2-(1-|\lambda_f|^2)\,\cos(\Delta m_B t) + 2\,\mathcal{I}m\;\lambda_f\,\sin(\Delta m_B t)\}, \end{aligned} \tag{1.24}$$

where,

$$\lambda_f \equiv \frac{q}{p}\,\frac{\overline{A}_f}{A_f} = \left|\frac{q}{p}\right| \cdot \left|\frac{\overline{A}_f}{A_f}\right| e^{i\Delta\phi}, \tag{1.25}$$

and $\Delta\phi = \phi_M - \phi_D$ is the relative phase between q/p and $\overline{A}_f/A_f$.

The rate time-dependent asymmetry is,

$$a_f(t) = \frac{R_{B^0_{\rm phys}} - R_{\overline{B}^0_{\rm phys}}}{R_{B^0_{\rm phys}} + R_{\overline{B}^0_{\rm phys}}} = C_f \ \cos(\Delta m_B t) + S_f \ \sin(\Delta m_B t), \tag{1.26}$$

where,

$$C_f = \frac{1 - |\lambda_f|^2}{1 + |\lambda_f|^2} \qquad \text{and,} \qquad S_f = \frac{-2 \ \mathcal{I}m\, \lambda_f}{1 + |\lambda_f|^2}\,. \tag{1.27}$$

If CP is conserved,

$$|\lambda_f| = 1\,, \ \ \left(\left|\frac{q}{p}\right| = 1 \ \ \text{and} \ \ \left|\frac{\overline{A}_f}{A_f}\right| = 1\right), \ \text{and} \ \ \Delta\phi = 0\,. \tag{1.28}$$

Therefore,

$$\lambda_f \neq \pm 1 \ \ \text{implies } CP \text{ violation.} \tag{1.29}$$

$a_f \neq 0$ if any of the 3 types of CP violation are present. For decays with $|\lambda_f| = 1$, CP violation will occur if $\mathcal{I}m\, \lambda_f \neq 0$, in which case,

$$a_f(t) = -\mathcal{I}m\, \lambda_f \ \sin(\Delta m_B t)\,. \tag{1.30}$$

1.4.1 Comparing *CP* Asymmetry for Coherent and Incoherent $B\overline{B}$ States

Two methods for producing B mesons can be considered. At a e^+e^-B Factory operating at the $\Upsilon(4\mathrm{S})$ resonance, the $B^0\overline{B}^0$ pair are produced in a coherent $L = 1$ state, with an antisymmetric wave function, (whereas, at a hadron collider, the $B^0\overline{B}^0$ pair are produced incoherently).

Each B meson evolves in time according to the model described in section 1.3, but with the constraint that the two Bs oscillate in phase, so that the time evolution of the system is given by,

$$S(t_1, t_2) \ \ = \tfrac{1}{\sqrt{2}} e^{-(\Gamma/2 + iM)(t_1 + t_2)} \{B^0_{\rm phys}(t_1)\overline{B}^0_{\rm phys}(t_2) - \overline{B}^0_{\rm phys}(t_1)B^0_{\rm phys}(t_2)\}, \tag{1.31}$$

where t_1 and t_2 are the proper times associated with each of the B mesons, and assuming that the $B^0\overline{B}^0$ pair are aligned with the z-axis. Expressing this in terms of the flavour eigenstates,

$$\begin{aligned} S(t_1,t_2) &= \tfrac{1}{\sqrt{2}}e^{-(\Gamma/2+iM)(t_1+t_2)}\{\cos[\Delta m_B(t_1-t_2)/2](B_1^0\overline{B^0}_2 - \overline{B^0}_1 B_2^0) \\ &\quad -i\sin[\Delta m_B(t_1-t_2)/2](\tfrac{p}{q}B_1^0 B_2^0 - \tfrac{q}{p}\overline{B^0}_1\overline{B^0}_2)\}\,. \end{aligned} \tag{1.32}$$

For the coherent $B^0\overline{B}^0$ system, the $|B^0_{\rm phys}\rangle$ and $|\overline{B}^0_{\rm phys}\rangle$ oscillate in phase, so that at any time there is always exactly one B^0 and one $\overline{B}^0$, since $t_1 = t_2$. However, following the decay of one of the two $B^0\overline{B}^0$, the other continues to evolve until it decays, and $t_1 = t_2$ no longer holds; this introduces a non-zero sine term, in general, which is the source of CP violation in mixing.

The total amplitude for a decay in which one of the Bs decays to a final state f_1 at time t_1, and the other decays to a final state f_2 at time t_2, is given by,

$$\begin{aligned} A(t_1,t_2) = \frac{1}{\sqrt{2}}e^{-(\Gamma/2+iM)(t_1+t_2)}&\cos(\Delta m_B(t_1-t_2)/2)(A_1\overline{A_2} - \overline{A_1}A_2) \\ &-i\sin(\Delta m_B(t_1-t_2)/2)\left(\frac{p}{q}A_1A_2 - \frac{q}{p}\overline{A_1A_2}\right) \end{aligned} \tag{1.33}$$

where A_i is the amplitude for a B^0 to decay to the final state f_i and $\overline{A_i}$ is the amplitude for a $\overline{B^0}$ to decay to the same final state f_i.

The time-dependent rate for producing combined final states f_1 and f_2 is,

$$\begin{aligned} R(t_1,t_2) &= Ce^{-\Gamma(t_1+t_2)}|\overline{A}_1|^2|A_2|^2\{1+|\lambda_2|^2 \\ &+ (1-|\lambda_2|^2)\ \cos[\Delta m_B(t_2-t_1)] - 2\ \mathcal{I}m(\lambda_2)\ \sin[\Delta m_B(t_2-t_1)]\} \end{aligned} \tag{1.34}$$

The time-dependent CP asymmetry is,

$$a_2(t_2-t_1) = C_2\ \cos(\Delta m_B(t_2-t_1)) + S_2\ \sin(\Delta m_B(t_2-t_1)) \tag{1.35}$$

This expression can be integrated over the variable $(t_1 + t_2)$, which for $t_1 \geq 0$ and $t_2 \geq 0$ can take values in the range $|t_1 - t_2|$ to infinity [13],

$$\int_{-(t_1+t_2)}^{+(t_1+t_2)} a_2 \; dt = C_2 \int_{-(t_1+t_2)}^{+(t_1+t_2)} \cos(\Delta m_B(t_2 - t_1)) \; dt \tag{1.36}$$

Thus, the dependence on the variable $t_1 - t_2$ can be fitted without a measurement of the $\Upsilon(4\mathrm{S})$ decay time. This is the main motivation for building an energy-asymmetric collider for the B Factory, since, if it were necessary to integrate over $t_1 - t_2$, all information on the coefficient of $\sin(\Delta m_B(t_1 - t_2))$ would be lost, and the experiment would be sensitive only to those CP-violating effects with $|\lambda| \neq 1$. This is a consequence of the coherent production of the two B states, (in a hadronic environment, where the Bs are produced incoherently, time-integrated rates are always integrals from $t = 0$ to infinity and hence retain information about the $\sin(\Delta m_B t)$ behaviour).

1.5 *CP* Violation in the Standard Model

1.5.1 The CKM Matrix

The CKM (Cabbibo-Kobayashi-Maskawa) matrix is the matrix of weak couplings between the quarks, and must be unitary if only three generations of quarks exist. The three magnitudes and one phase of the matrix may be parameterised in many different ways. The standard parameterisation [14] is given by,

$$\begin{pmatrix} V_{ud} & V_{us} & V_{ub} \\ V_{cd} & V_{cs} & V_{cb} \\ V_{td} & V_{ts} & V_{tb} \end{pmatrix} = \begin{pmatrix} c_{12}c_{13} & s_{12}c_{13} & s_{13}e^{-i\delta} \\ -s_{12}c_{23} - c_{12}s_{23}s_{13}e^{i\delta} & c_{12}c_{23} - s_{12}s_{23}s_{13}e^{i\delta} & s_{23}c_{13} \\ s_{12}s_{23} - c_{12}c_{23}s_{13}e^{i\delta} & -c_{12}s_{23} - s_{12}c_{23}s_{13}e^{i\delta} & c_{23}c_{13} \end{pmatrix}, \tag{1.37}$$

where $c_{ij} = \cos\theta_{ij}$ and $s_{ij} = \sin\theta_{ij}$, and i and j represent generation labels. The four parameters are θ_{12}, θ_{23} and θ_{31} and δ. With three generations CP violation arises from

a single phase, δ in the CKM matrix. This parameterisation has the advantages that it is an exact representation, and it is readily generalised to more than three generations of quarks. The magnitudes of the elements of the matrix have been determined from a range of processes, but the uncertainty on these measurements varies greatly, see table 1.38.

Table 1-1. *Current measurements of elements of the CKM matrix [13]*

Matrix element	Process	Measurement
$\|V_{ud}\|$	nuclear β decay compared to μ decay	0.9744 ± 0.0010
$\|V_{us}\|$	semileptonic kaon decays	0.2205 ± 0.0018
$\|V_{ub}\|$	$B \to X_u \ell \nu$	$0.08 \pm 0.005 \pm 0.02_{th}$
$\|V_{cd}\|$	$\nu\overline{\nu}$ charm production from d	0.204 ± 0.017
$\|V_{cs}\|$	$\nu\overline{\nu}$ charm production from s	1.01 ± 0.18
$\|V_{cb}\|$	$B \to D^* \ell \nu$	$0.039 \pm 0.0027 \pm 0.0013_{th}$

A useful approximation to the CKM matrix was proposed by Wolfenstein [15]. This expresses the elements in terms of powers of the Cabibbo angle [16], λ, up to $\mathcal{O}(\lambda^3)$, which emphasises their relative magnitudes. The phase is given by η.

$$V_{CKM} = \begin{pmatrix} 1 - \frac{\lambda^2}{2} & \lambda & A\lambda^3(\rho - i\eta) \\ -\lambda & 1 - \frac{\lambda^2}{2} & A\lambda^2 \\ A\lambda^3(1 - \rho - i\eta) & -A\lambda^2 & 1 \end{pmatrix} + \mathcal{O}(\lambda^4) \tag{1.38}$$

1.5.2 The Unitarity Triangle

The unitarity of the CKM matrix, under the assumption of only three generations, produces the following relations,

$$V_{ud}V_{us}^* + V_{cd}V_{cs}^* + V_{td}V_{ts}^* = 0, \tag{1.39}$$

$$V_{us}V_{ub}^* + V_{cs}V_{cb}^* + V_{ts}V_{tb}^* = 0, \tag{1.40}$$

$$V_{ud}V_{ub}^* + V_{cd}V_{cb}^* + V_{td}V_{tb}^* \quad = \quad 0. \tag{1.41}$$

These relations can be represented graphically as triangles in the complex plane. There are six such triangles, with the property that they all have the same area, which is proportional to the amount of CP violation in the Standard Model. Equation 1.39 is most closely related to CP violating phenomena in the K system, and equation 1.40 is related to the B_s system. CP violation in the B_d system is related to equation 1.41.

The triangle corresponding to equation 1.41 relates easily to the Wolfenstein parameterisation, where the phase is present in the terms V_{ub} and V_{td}. Dividing (1.41) by $A\lambda^3$ normalises the base of the triangle to unity, and places the triangle apex at the point $(\overline{\rho}, \overline{\eta})$ in the ρ, η plane. The angles, α, β, γ, and sides, R_b, R_t, of this Unitarity Triangle are given by,

$$\alpha \equiv \arg\left[-\frac{V_{td}V_{tb}^*}{V_{ud}V_{ub}^*}\right], \quad \beta \equiv \arg\left[-\frac{V_{cd}V_{cb}^*}{V_{td}V_{tb}^*}\right], \quad \gamma \equiv \arg\left[-\frac{V_{ud}V_{ub}^*}{V_{cd}V_{cb}^*}\right], \tag{1.42}$$

$$R_b \equiv \sqrt{\overline{\rho}^2 + \overline{\eta}^2} = \frac{1 - \lambda^2/2}{\lambda}\left|\frac{V_{ub}}{V_{cb}}\right|, \quad R_t \equiv \sqrt{(1-\overline{\rho})^2 + \overline{\eta}^2} = \frac{1}{\lambda}\left|\frac{V_{td}}{V_{cb}}\right|. \tag{1.43}$$

A diagram of the Unitarity Triangle in the Wolfenstein parameterisation is given in Fig.1-2.

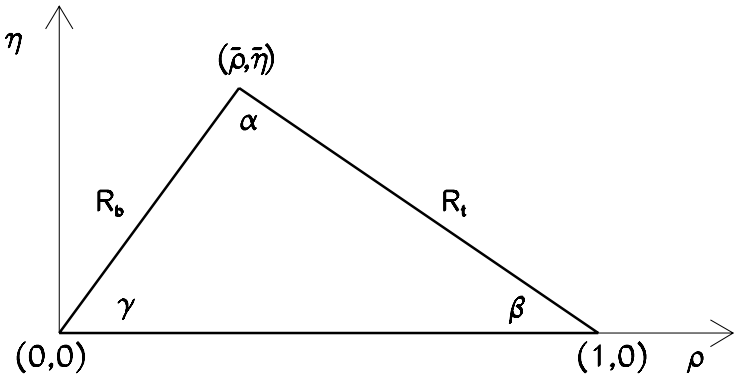

Figure 1-2. *The Unitarity Triangle in the Wolfenstein Parameterisation.*

1.5.3 Constraints on the Unitarity Triangle

In the Wolfenstein parameterisation, the four CKM parameters are λ, A, ρ, η, where λ is taken to be equal to $|V_{us}|$. Of these, only λ is known to within 1% accuracy, while ρ and η are the least well-determined, so it is useful to illustrate the current constraints on the CKM parameters in the ρ, η plane, Fig.1-3. The overlap region of all the shaded zones represents the likely Standard Model allowed region for the triangle apex, with the experimental measurements shifted within 2σ for each constraint.

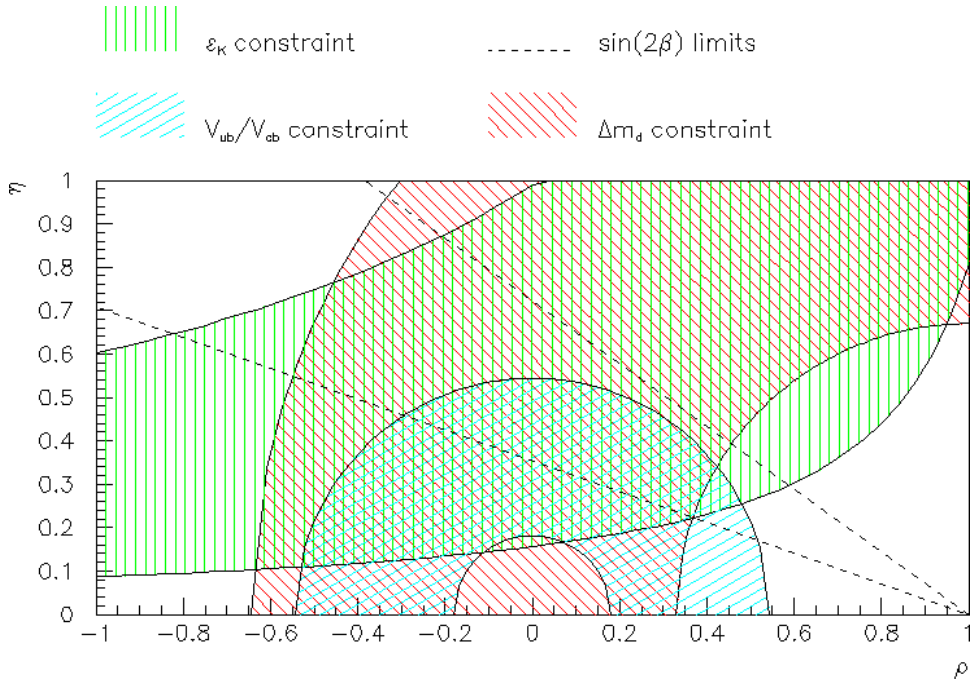

Figure 1-3. *Diagram of the ρ, η plane showing constraints on the Unitarity Triangle.*

In $B^0\overline{B}^0$ mixing, the splitting between B mass eigenstates, Δm_{B_d}, depends on ${m_t}^2$ and $|V_{td}|^2$, since the top quark dominates the box diagrams. Since $|V_{td}|$ is proportional to $|1 - \rho - i\eta|$, constraints on Δm_{B_d} produce a circular arc in the (ρ, η) plane, centred on (1,0).

The ratio $\left|\frac{V_{ub}}{V_{cb}}\right|$ has been estimated from studying the charged lepton spectra in semileptonic B decays to determine the relative contributions of $b \to u\overline{\nu}_e e^-$ and $b \to c\overline{\nu}_e e^-$. The charmless decay mode is rare compared to the charmful one, indicating that $|V_{ub}| << |V_{cb}|$. However, these events can be isolated by identifying leptons with energies above the kinematic limit for $b \to c\overline{\nu}_e e^-$. ARGUS [17] and CLEO [18] have shown that charmless events occur in $\sim 2\%$ of cases. The uncertainty is dominated by theoretical uncertainty in the ratio $\frac{m_c}{m_b}$. Some model dependency is introduced in the fitting technique, and after allowing for this the result is,

$$\left|\frac{V_{ub}}{V_{cb}}\right| = 0.08 \pm 0.02 \quad ; \quad (\rho^2 + \eta^2)^{1/2} = 0.36 \pm 0.09 \tag{1.44}$$

Hence, in the ρ, η plane this constraint appears as a semicircle (for positive η) centred on (0,0).

Information from CP violation in the kaon system can also be incorporated in the overall constraints, provided it is borne in mind that this implies the origin of CP violation in the K system is the same as that for the B system. Recent results from the KTeV experiment [19] have determined the ratio $\frac{\varepsilon'}{\varepsilon}$ to be large; $\mathcal{R}e(\frac{\varepsilon'}{\varepsilon}) = 28.0 \pm 4.1 \times 10^{-4}$. This result, which is nearly 7 standard deviations from zero, provides the first strong evidence for direct CP violation in K decays.

$\frac{\varepsilon'}{\varepsilon}$ is a poorly predicted quantity within the Standard Model since it depends sensitively on the cancellation of two unknown bag factors[2], whose difference must be small, and could be zero. Present estimates of these quantities combined with the large value of the KTeV measurement give stringent constraints on the unitarity triangle. However, an improvement in the theoretical uncertainties is needed before conclusions can be drawn about the consequences for the Standard Model.

The hyperbolae produced by the ε constraint limit the unitarity triangle apex to have a non-zero value of η. However, if CP violation in kaon decay is due to a different source,

[2] B_6 from QCD penguins and B_8 from electroweak penguins

then the possibility of $\eta = 0$ still exists. The recent results by CDF [20] appear to rule out that possibility, with a constraint on $\sin 2\beta$ from the decay of $B^0 \to J/\psi K^0_S$.

Table 1-2. *Experimental inputs to the constraints on the Unitarity Triangle*

Observable	Process	Measurement
$\|V_{ub}\ /V_{cb}\|$	$B \to X_u \ell \nu$	$0.08 \pm 0.005 \pm 0.02_{th}$
λ	$K^+ \to \pi^0 e^+ \nu$	0.2205 ± 0.0018
Δm_{B_d}	$B^0_d - \overline{B}^0_d$ oscillations	0.472 ± 0.018 ps^{-1}
ϵ_K	CP violation in $K^0 - \overline{K}^0$ mixing	$(2.285 \pm 0.019) \times 10^{-3}$
Δm_{B_s}	$B^0_s - \overline{B}^0_s$ oscillations	> 10.2 ps^{-1} @ 95% CL

1.6 Summary

A brief history of the development of CP physics has been given, with a discussion of its importance and relevance to an understanding of the Universe. The phenomenology of CP violation was introduced in a model-independent way using the neutral B system. Finally, the role of CP violation in the Standard Model was discussed, and the present constraints on the unitarity triangle were shown.

2

The PEP–II B Factory and the BaBar Detector

2.1 Introduction

The study of CP violating asymmetries in the B meson system provides an opportunity for testing the Standard Model explanation of CP violation. While CP violation is expected to be high in B system, due to the large rate of $B^0\overline{B}^0$ mixing [21], the branching ratios for decays to CP eigenstates are small (typically $\sim \mathcal{O}(10^{-4})$. Prior to 1983, it seemed unlikely that the experimental testing of CP violation in the B system was feasible. However, the subsequent discovery of the long B lifetime [10], [11] presented the prospect of being able to resolve the decay vertices of the Bs with existing technology. This is possible only if the $B\overline{B}$ pair are boosted in the laboratory frame, which, if produced at the $\Upsilon(4\mathrm{S})$ resonance, requires an asymmetric collider [22].

A B Factory has been developed at SLAC using an asymmetric e^+e^- storage ring, PEP–II [23]. The machine operates at the centre-of-mass energy of the $\Upsilon(4\mathrm{S})$ resonance, which decays to a pair of B mesons essentially at rest in the $\Upsilon(4\mathrm{S})$ rest frame. This boosts the B mesons in the z direction in the laboratory frame, giving a separation of $\sim 200\,\mu\mathrm{m}$ between their subsequent decays. Vertex reconstruction is then used to measure the separation, and thus the time difference of the $B\overline{B}$ decays.

The experiment aims to reconstruct B mesons into a wide range of final CP eigenstates [24], [25]. For the PEP–II machine this means a high integrated luminosity. The design

requirements of high luminosity and asymmetry for the PEP–II B Factory have, in turn, had a strong impact on the design of the detector [26],[27]. In order to reconstruct the many proposed exclusive final states the BABAR detector must provide precision vertexing, excellent particle identification (PID), and high quality tracking and calorimetry [28]. Since, for CP studies, the final state is common to both B^0 and $\overline{B}^0$ decays, the flavour of the B at the time of its decay is not directly known. The method for establishing the B^0_{CP} flavour is known as tagging : for certain decay modes (most notably semi-leptonic decays) the flavour of the other B meson which was produced from the $\Upsilon(4\mathrm{S})$ can be determined, and this is used to infer the flavour of the B^0_{CP} at the time when the first of the Bs decays. The time difference between the decays of the two Bs, together with the tag sign ($\pm$ according to the charge of the b quark of the B^0_{CP}), provide the information necessary for extracting a CP asymmetry.

An overview of the PEP–II B Factory and the BABAR detector is given below, and the aims of the experiment are discussed. The roles of the individual subsystems are reviewed, and features of their design are described. The electromagnetic calorimeter is then discussed in some detail, including the requirements which are placed on the properties of its constituent crystals in order that performance for physics is optimised.

2.2 *PEP–II B* Factory

The PEP–II B Factory is a high luminosity asymmetric e^+e^- collider which is supplied from the SLAC linear accelerator. The centre of mass energy is $\sqrt{s}$ = 10.58 GeV, which corresponds to the $\Upsilon(4\mathrm{S})$ resonance. The beam energies are 9.0 GeV for e^- and 3.1 GeV for e^+, which provides a boost of $\beta\gamma = 0.56$ for the B meson system. The initial design luminosity is $3 \times 10^{33}\,\mathrm{cm}^{-2}\mathrm{s}^{-1}$, which corresponds to $B\overline{B}$ production ~ 3 Hz. The luminosity is given by,

$$\mathcal{L} = 2.17\ 10^{34}\ \xi\ (1 + \frac{\sigma_y}{\sigma_x})\ \left(\frac{I\,E}{\beta^*_y}\right)_{+-}\ \mathrm{cm}^{-2}\mathrm{s}^{-1}\,,$$

where the terms are defined in table 2-1.

Table 2-1. *PEP–II Parameters.*

Machine Parameters		
Luminosity $\mathcal{L}$ ($\mathrm{cm^2 s^{-1}}$)	3×10^{33}	
Tune shift ξ	0.03	
Number of bunches	1658	
Bunch spacing (m)	1.26	
Beam crossing angle	0 (head-on)	
σ_x (μm at IP)	155	
σ_y (μm at IP)	6.2	
Beam Parameters	e^+	e^-
σ_z (cm)	1.0	1.15
Beam energy E (GeV)	3.1	9.0
Beam current I (A)	2.14	0.98
β_y^* (cm)	1.5	2.0
ϵ_x (ϵ_y)(nm)	64(2.6)	48(1.9)

The high luminosities needed to achieve the physics goals at BABAR are achieved by a combination of strong beam focusing and high beam currents. This has necessitated the design of unusual beam optics, with a number of machine elements coming very close to the interaction region. The beam current is divided into a large number of bunches, each having a low current, so that beam instability is reduced.

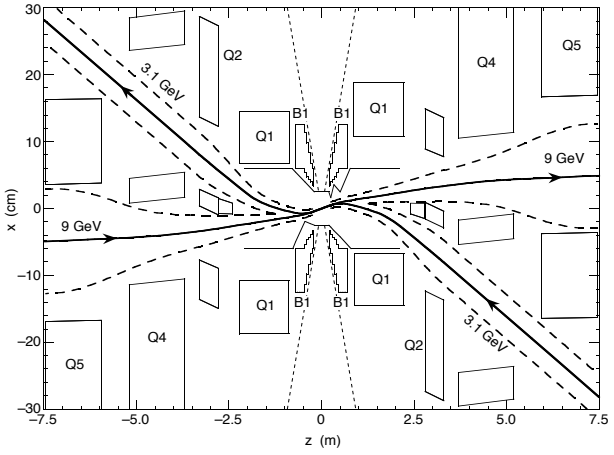

Figure 2-1. *Plan view of the PEP–II interaction region, showing the focusing of the beams in the magnetic field.*

The PEP–II interaction region is illustrated in Fig.2-1. The strong focusing of the beams is provided by the Q1 quadrupoles close to the interaction point. The asymmetry of the collider means that the beams must be well-separated even in the regions very close to the interaction point. This is achieved using a series of magnets which provide further focusing. The B1 magnets provide horizontal separation of the beams. The Q2 magnets provide focusing of the low energy beam, and Q4 and Q5 focus the high energy beam.

The beam pipe which houses the interaction region is constructed from cooled Beryllium tubing. It consists of two concentric tubes, the inner one of diameter 50 mm and thickness 0.8 mm, and the outer one of diameter 54 mm and thickness 0.4 mm. A cylindrical support tube of diameter 430 mm surrounds the beam pipe, and provides the mounting point for the Q1 and B1 magnets, as well as the silicon vertex tracker. The assembly of these components is illustrated in Fig.2.2.

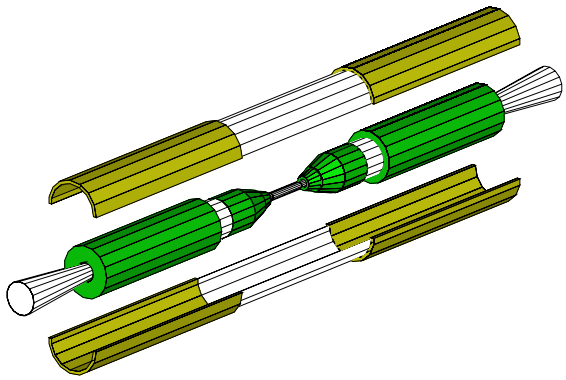

Figure 2-2. *Three-dimensional view of the $PEP-II$ interaction region, showing the inner magnets (green) and beam support tube (yellow), (diameter 430 mm).*

The high currents of PEP–II mean that machine backgrounds will be significant, and typically an order of magnitude larger than previous machines. The main sources of machine background are synchrotron radiation, and lost beam particles from beam gas interactions, from bremsstrahlung or Coulomb scattering. The two main consequences for the detector performance are high occupancy levels and potential radiation damage. The trigger system has been designed to cope with the high occupancy levels, and is

discussed in section 2.10. The problem of radiation damage is a particular concern for the electromagnetic calorimeter and is discussed in section 2.7.

2.2.1 Production Cross-Sections at $\Upsilon(4S)$

The cross-sections for the production of fermion pairs at the $\Upsilon(4S)$ are shown in table 2-2. The cross-sections for quark production are approximately proportional to the square of the quark charge. At the $\Upsilon(4S)$ resonance, the production of $b\overline{b}$ is further enhanced by about a factor three. A scan of the $\Upsilon(4S)$ resonance [29] is shown in Fig.2-3, together with the $\Upsilon(3S)$; here, R is the ratio of $e^+e^- \rightarrow q\overline{q}$ to $e^+e^- \rightarrow \mu\mu$ events, measured for a range of centre-of-mass energies. The $\Upsilon(4S)$ resonance signals the threshold for $b\overline{b}$ production, hence the increase in the (non-resonant) value of R above the $\Upsilon(4S)$.

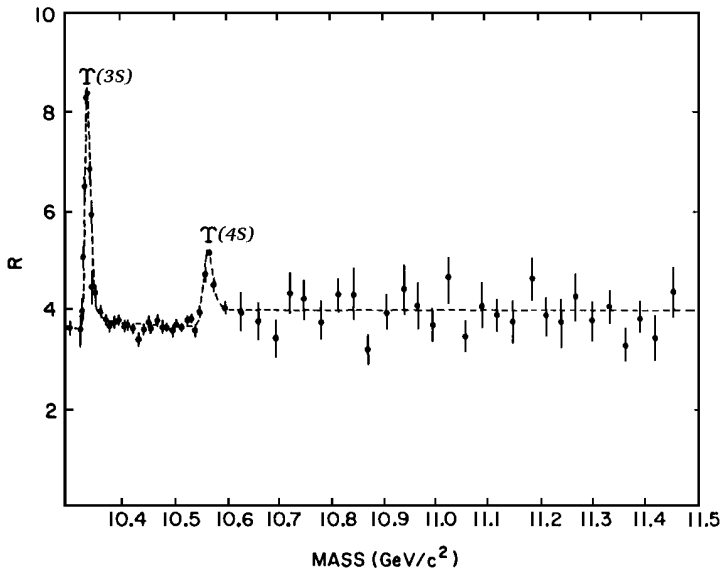

Figure 2-3. $R = \mathrm{BR}(e^+e^- \rightarrow q\overline{q})/\mathrm{BR}(e^+e^- \rightarrow \mu\mu)$ *as a function of centre-of-mass energy in the region of the b-flavour threshold.*

Table 2-2. *Production cross-sections at $\sqrt{s} = M_{\Upsilon(4S)}$. The e^+e^- cross-section is the effective cross-section expected within the experimental acceptance.*

$e^+e^- \rightarrow$	Cross-section σ (nb)	number of events for 30 fb^{-1}
$b\overline{b}$	1.05	3.15 10^7
$c\overline{c}$	1.30	4.33 10^7
$s\overline{s}$	0.35	1.17 10^7
$u\overline{u}$	1.39	4.63 10^7
$d\overline{d}$	0.35	1.17 10^7
$\tau^+\tau^-$	0.94	3.13 10^7
$\mu^+\mu^-$	1.16	3.87 10^7
e^+e^-	~ 40	132 10^7

2.3 The BABAR Detector

2.3.1 Design Requirements

The design of the BABAR detector is dominated by the asymmetry of the collider, and the need to accommodate machine components close to the interaction region. In order to achieve the aims of the CP physics programme, the following design attributes are required for the detector :

- The maximum possible acceptance in the center-of-mass system.

  The asymmetry of the beams in BABAR causes the decay products to be boosted forward in the laboratory frame. This puts the solid angle in the forward direction at a premium. Although the boost is relatively small, optimizing the detector acceptance leads to an asymmetric detector.

- Excellent vertex resolution

  The B mesons travel almost parallel to the z-axis, so that their decay time difference is measured via a difference in the z-components of their decay positions. The experiment needs to achieve high-precision vertex information in order to help in the discrimination of beauty, charm and light quark vertices. Vertex resolution is

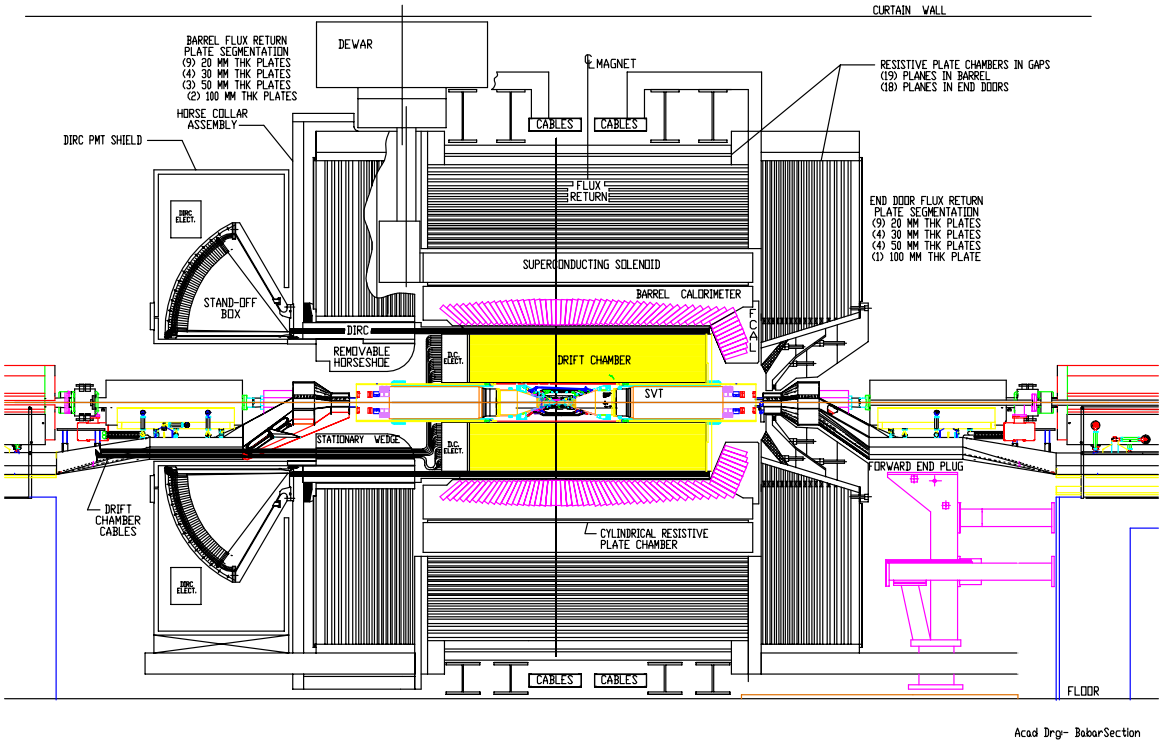

Figure 2-4. *A cross-sectional view of the BABAR detector (length 6.29 m).*

degraded by multiple scattering effects, so the design must also address minimising multiple scattering by reducing material in front of the main tracking systems.

- Optimal tracking over a wide range of momenta ($\sim 60\,\mathrm{MeV} < \mathrm{p_t} <\sim 4\,\mathrm{GeV}$), in order to reconstruct exclusive final states which require tracking.
- Efficient neutral particle reconstruction, which requires that the calorimeter to have excellent energy and position resolution. Photons and π^0 s need to be detected over the wide energy range $\sim 20\,\mathrm{MeV} < \mathrm{E} <\sim 5\,\mathrm{GeV}$.
- Excellent PID is needed to discriminate between e, μ, π, K and p over a wide kinematic range, and is necessary for the correct tagging of the flavour of the B-mesons. Additionally, $\pi - K$ discrimination at high momenta (2–4 GeV) is essential in order to distinguish between the decay channels $B^0 \to \pi^+\pi^-$ and $B^0 \to K^\pm\pi^\mp$,

$B^0 \to \rho\pi$ and $B^0 \to K\rho$ and $B^0 \to K^*\pi$. Neutral hadron identification capability is also required.

A cross-sectional view of the BABAR detector is shown in Fig.2-4. The asymmetry of the detector can clearly be seen. The high energy e^- beam enters from the left, and the low energy e^+ beam from the right.

The BABAR detector consists of six major subsystems :

1. A Silicon Vertex Tracker (SVT), which provides precise position information for charged tracks, and is the sole tracking device for very low energy charged particles.
2. A Drift Chamber (DCH), which gives the main charged track momentum measurement, and contributes to PID by measuring energy losses.
3. A Detector of Internally Reflected Čerenkov light (DIRC), which is a uniquely designed device for πK discrimination, and charged hadron PID.
4. An Electromagnetic Calorimeter (EMC), for the detection of neutral electromagnetic particles, efficient electron identification, and information for neutral hadron identification.
5. A superconducting magnet, providing a 1.5 T solenoidal magnetic field.
6. An Instrumented Flux Return (IFR), which offers muon identification $(\geq 0.6GeV)$ and neutral hadron identification.

The main features of each of the subsystems are described in the following sections.

2.4 The Silicon Vertex Tracker

2.4.1 Design Requirements

The primary purpose of the silicon vertex tracker is to provide precise measurements of the decay vertices of the two B mesons, which are required to establish the separation in time of their decays. Given the boost of the $\Upsilon(4\mathrm{S})$ and the B lifetime, the mean vertex separation is $\sim 250\,\mu\mathrm{m}$. Therefore the design resolution on the B separation required by the SVT is of the order of $80\,\mu\mathrm{m}$, which is a precision of better than one half the mean separation. This resolution is readily achievable with silicon micro-strip detectors. However, obtaining a better precision will assist with pattern recognition, vertex reconstruction and background rejection. The silicon vertex tracker was designed to reach the best resolution within practical constraints. Multiple scattering sets the lower limit for the useful point resolution: resolutions of 10–15 $\mu\mathrm{m}$ for the inner layers, and 30–40 $\mu\mathrm{m}$ for the outer ones, will ensure that the impact parameter resolution will be dominated by the uncertainty given by multiple scattering [30].

As the impact parameter resolution is dominated by the precision of the measurement closest to the interaction point, both high efficiency and good point resolution are needed for the inner layers, requiring redundancy for this measurement. Also an outer point redundant measurement is needed to allow a better alignment with the drift chamber measurements. The third detector, placed in the middle region, will help the track reconstruction in particular when the tracks' helices are completely contained in the silicon vertex tracker volume.

The reliability of the detector and its ability to withstand the high radiation environment of $PEP\text{–}II$, have been given particularly high priority, since the detector has been mounted in an area of poor accessibility.

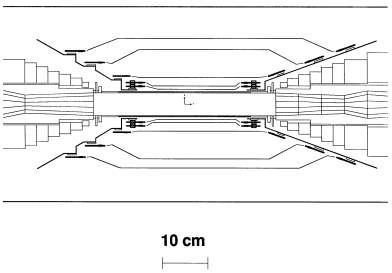

Figure 2-5. *Side-view diagram of the SVT.*

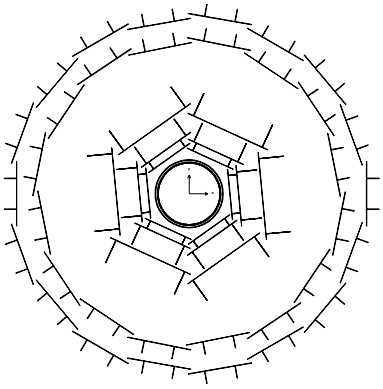

Figure 2-6. *Cross-section diagram of the SVT.*

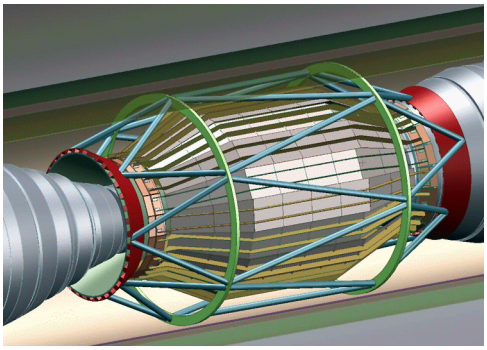

Figure 2-7. *A three-dimensional view of the silicon vertex tracker mounted around the interaction region*

2.4.2 Structure

The SVT has five layers of double-sided silicon strip detectors surrounding the beampipe. Each layer is divided in azimuth into modules. The inner three layers have six detector modules, and are traditional barrel-style structures. The outer two consist respectively of 16 and 18 detector modules, and employ a new arch structure in which the detectors are electrically connected across an angle. The bend in the arch modules increases the solid angle coverage and avoids very large track incidence angles. The inner sides of the detectors have strips oriented perpendicular to the beam direction to measure the z coordinate (z-side), whereas the outer sides, with longitudinal strips, allow the ϕ coordinate measurement (ϕ-side).

2.5 The Drift Chamber

2.5.1 Design Requirements

The drift chamber provides the main tracking system for BABAR. It provides up to 40 coordinate measurements per track, ensuring high reconstruction efficiency for tracks with transverse momentum greater than 100 $\mathrm{MeV/c}$.

The performance goals of the drift chamber, are to provide spatial resolution better than 140 μm, averaged over the cell in the R-ϕ plane, and to supply PID for low momentum tracks by $\mathrm{d}E/\mathrm{d}x$, with a resolution of 7% (for 40 measurements). For tracks with momentum above 1 $\mathrm{GeV/c}$, a resolution of $\sigma_{p_t} \approx 0.3\% \times p_t$ is expected. The angular acceptance in the forward region must extend down to the beam-line components, *i.e.,* 300 mr. In addition, the drift chamber is designed to provide one of the principal triggers for the experiment.

For low momentum tracks, the momentum resolution is limited by the multiple scattering in the inner cylinder of the drift chamber as well as in the silicon vertex tracker. The material in the drift chamber also affects the performance of the DIRC and the electromagnetic calorimeter. The mechanical structure of the drift chamber is built using light materials and the gas mixture is Helium-isobutane, to provide good spatial and $\mathrm{d}E/\mathrm{d}x$ resolution and reasonably short drift time, while minimizing the material.

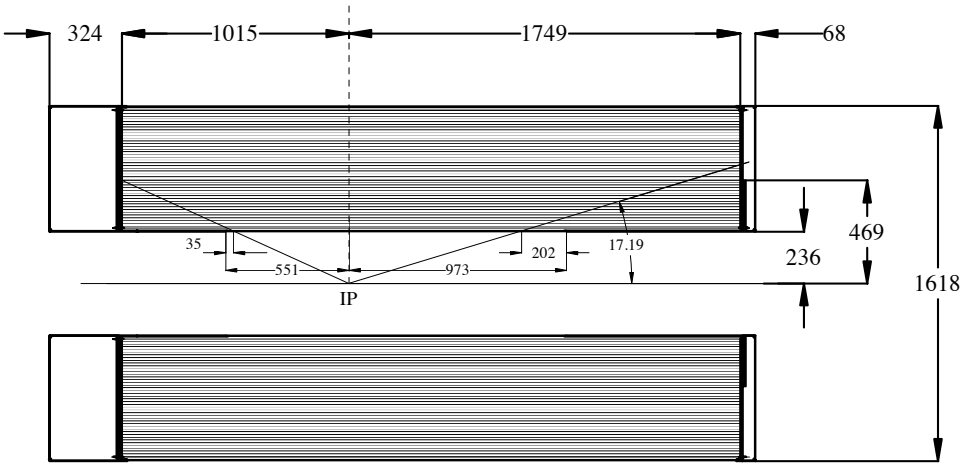

Figure 2-8. *A two-dimensional view of the drift chamber*

2.5.2 Structure

The BABAR drift chamber is a 280 cm-long cylinder, with an inner radius of 23.6 cm and an outer radius of 80.9 cm. The flat endplates are made of aluminum. Since the BABAR events will be boosted in the forward direction, the design of the detector is optimized to reduce the material in the forward end. The forward endplate is made thinner (12 mm) in the acceptance region of the detector compared to the rear endplate (24 mm), and the readout electronics is mounted on the rear endplate to minimize the material in the forward region. The inner cylinder is made of 1 mm beryllium, which corresponds to 0.28% radiation lengths (X_0). The outer cylinder consists of 2 layers of carbon fiber on a Nomex

core, corresponding to 1.5% X_0. The drift cells are arranged in 10 superlayers, each consisting of 4 layers set in axial and stereo orientations.

2.6 The DIRC

2.6.1 Design Requirements

The DIRC (Detection of Internally Reflected Čerenkov light) is a new type of Čerenkov-based detector [31] devoted to PID. In particular, the DIRC is designed to provide excellent kaon identification, both for tagging, where kaon momenta extend up to about $2.0\,\mathrm{GeV/c}$, and also at higher momenta for reconstruction of rare decays. A good π/K separation therefore requires resolutions on the Čerenkov angle for a track of $2\,\mathrm{mr}$ or better. The single photoelectron resolution, intrinsically limited by geometry and quartz achromaticity, is of order $9\,\mathrm{mr}$, largely independent of the track momentum and dip angle. Designed track resolutions are obtained by combining measurements from the large number of photoelectrons generally observed for each track. As an example, the expected number of photoelectrons for an ultrarelativistic particle at 60° of dip angle is larger than 50. This number drops to around 25 at some smaller dip angles, but momentum spectra are then much softer.

The DIRC performance depends also on the accuracy of extrapolated track parameters and their errors, as provided by the tracking software. The best accuracy is obtained with a Kalman filter fit, which takes into account correctly the effects of scattering and energy loss in the material along the trajectory, including the material between the last drift chamber hit and the quartz bar. At low momenta, the uncertainty on the track direction due to multiple scattering in the drift chamber outer wall, the DIRC supports and the bar itself, actually dominates the error on the Čerenkov angle measurement. Čerenkov

resolutions are greatly improved at low momenta by a full constrained fit of the Čerenkov image. This is particularly relevant for μ/π separation below $750\,\mathrm{MeV/c}$.

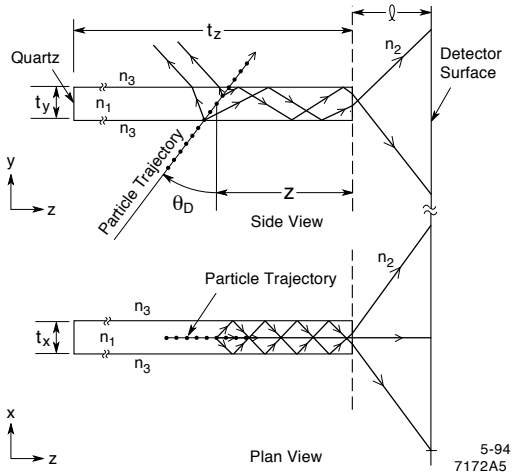

Figure 2-9. *Diagram showing the total internal reflection of Čerenkov light inside the quartz bars*

2.6.2 Structure

The DIRC uses 144 long thin quartz bars as both radiator and light guide, arranged in a 12-sided polygon around the beam line with an internal radius of $80\,\mathrm{cm}$. At the end of the bar the light emerges and forms a cone on the detector surface which maintains the information on the Čerenkov angle, up to a certain number of discrete ambiguities, some of which can be resolved by the photon arrival-time measurement. Remaining ambiguities are dealt with by the pattern recognition during Čerenkov angle reconstruction. The refractive index of quartz is close to 1.474. In a quartz radiator, the Čerenkov threshold for kaons ($\sim 460\,\mathrm{MeV/c}$) is well below the value of momentum for which a pion and a kaon may be unresolved due to ionization loss measurement ($\mathrm{d}E/\mathrm{d}x$) in the drift chamber ($\sim 700\,\mathrm{MeV/c}$). The DIRC and drift chamber together form a complementary system for π/K separation.

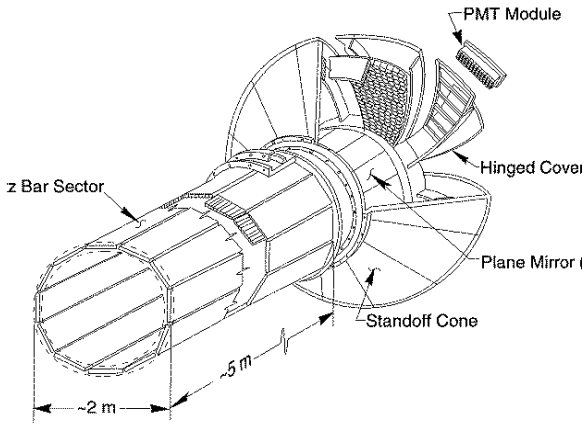

Figure 2-10. *A three-dimensional view of the DIRC detector showing the quartz bars and the standoff box supporting the PMT modules*

2.7 The Electromagnetic Calorimeter

2.7.1 Design Requirements

The design of the electromagnetic calorimeter is based on CsI(Tl) crystals with a quasi-projective geometry over a solid angle corresponding to $-0.775 \leq \cos\theta \leq 0.962$ in the laboratory frame, and $-0.916 \leq \cos\theta \leq 0.895$ in the center-of-mass frame. Useful physics coverage is slightly less since one has to stay away from the forward and backward edges to avoid excessive shower leakage. The properties of CsI(Tl) are summarized in Table 2-3. In comparison with other scintillating crystals commonly used in calorimetry CsI(Tl) has high density, excellent light output and long decay constant. The crystal scintillation light is read-out by photodiodes, because of the strong magnetic field in which the calorimeter lies.

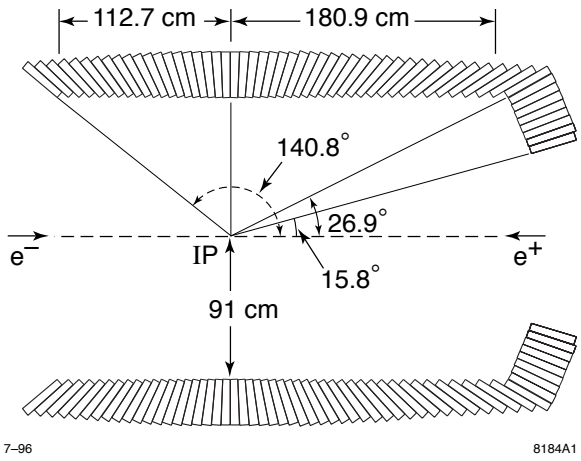

Figure 2-11. *Side-view of the electromagnetic calorimeter showing the distribution of crystals about the interaction point*

The target energy resolution for photons at a polar angle of 90° is [1],

$$\frac{\sigma_E}{E} = \frac{1\%}{\sqrt[4]{\mathrm{E(\,GeV)}}} \oplus 1.2\%.$$

The contributing factors to the energy resolution include electronic noise, shower leakage, absorption by inactive material in front of and between crystals, and shower fluctuations which result in measurement uncertainties due to crystal non-uniformity, and inter-calibration errors between crystals.

The angular resolution is determined by the transverse crystal size and average distance to the interaction point,

$$\sigma_{\theta,\phi} = \frac{3\mathrm{mrad}}{\sqrt[2]{\mathrm{E(\,GeV)}}} + 2\mathrm{mrad}.$$

The electromagnetic calorimeter must have excellent energy resolution in order to be able to reconstruct the many photons and $\pi^0\,s$ for studying exclusive B decays. To detect photons at low energy the system must have low noise, while high energy photons require long crystals for shower containment ($\sim$ 18 radiation lengths). The leakage must be

[1]The 4th root of energy in this expression is based on empirical observations, see for example [32].

Table 2-3. *Properties of Thallium-doped CsI.*

Properties	CsI(Tl)
Radiation Length (cm)	1.85
Molière Radius (cm)	3.6
Absorption Length for 5 GeV pions (cm)	41.7
Density (g/ cm^3)	4.53
$\mathrm{d}E/\mathrm{d}x\|_{mip}$ (MeV/cm)	5.6
Light Yield (Photons/ $\mathrm{MeV}\times 10^3$)	40–50
Light Yield Temperature Coef. (%/°C)	0.1
Peak Emission (nm)	565
Refractive Index at Emission Maximum	1.79
Decay Time (ns)	940
Hygroscopic	slight
Radiation Hardness (rad)	10^3–10^4

$\lesssim$ 5% to achieve decent energy resolution. It is also important to minimise inactive material between the crystals.

2.7.2 Structure

The calorimeter consists of a barrel and a forward conic endcap. A backward endcap was not included as the boost prevents all but a small fraction of neutral particles from travelling in the extreme backward direction ($-0.775 \leq \cos\theta_{lab} \leq 0.962$).

For a typical crystal, the light output varies with the position inside the crystal. Since there are stochastic fluctuations in the development of electromagnetic showers for an incident photon of a given energy, this dependence on position can affect energy resolution. The fluctuations can occur in the longitudinal starting point of the shower, and in its overall length, and width. The fluctuations in start point are greater for low energy photons, so non-uniformity affects low-energy resolution. For high energy photons, fluctuations in start point affect the total containment of the shower. For this reason, the ideal light output

profile for a crystal, rather than being flat, would benefit from a slight increase towards the rear of the crystal to compensate for energy leakage associated with fluctuations.

CsI has shown adequate radiation tolerance in previous experiments, however, the new environment will be harsher, with much higher beam currents, beam gas interactions and off-axis beam particles. Radiation damage appears mainly as a loss of scintillation light yield. This is thought to be due to the creation of absorption bands, which cause a decrease in light attenuation length, rather than due to a change in the scintillation mechanism itself. The absorption bands appear as a result of formation of colour centres where impurities or defects are present in the crystal. Another effect of radiation damage is increased fluorescence and/or phosphorescence in the crystal. This can cause problems with readout, especially in high event rate systems.

2.8 The Instrumented Flux Return

2.8.1 Design Requirements

The instrumented flux return (IFR) consists of the large iron structure which is segmented and instrumented with Resistive Plate Counters (RPCs). The iron is needed to act as a yoke for the magnetic field, and the RPCs provide muon identification for particle momenta above 400 MeV. Below this value charged particles do not reach the IFR because of the effect of the magnetic field. The DIRC can in this case be used to cover the momentum range 250-400 MeV and the SVT for the momentum range 50-130 MeV. Neutral hadron detection is also provided via the IFR and calorimeter.

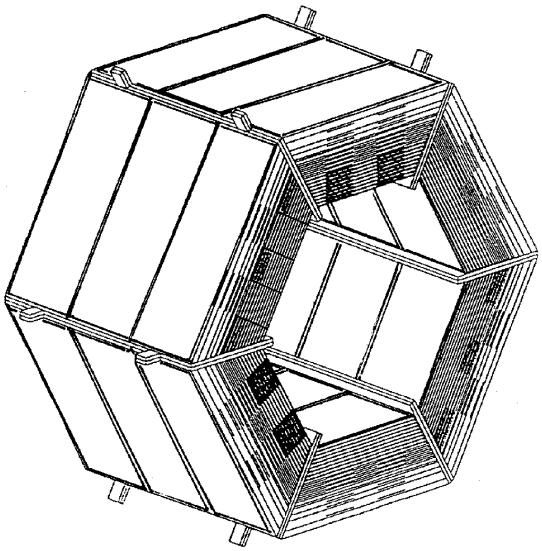

Figure 2-12. *Three-dimensional view of the IFR (length 6.29* m*).*

2.8.2 Structure

The IFR is a collection of iron plates whose thickness increases with the distance from the beamline. The strip type IFR active detectors, the Resistive Plate Chambers, are inserted in the slots between the iron plates, and provide a digital two-dimensional readout.

The IFR is divided into a Barrel and two Endcaps, which complete the solid angle coverage down to 300 mr in the forward direction and 400 mr in the backward direction. The barrel is composed of six sections longitudinal with the beamline, and each barrel section is divided into 19 detector layers. The endcaps have 6 different shape sectors, and each endcap section includes 18 detector layers orthogonal to the beam line.

2.9 The Superconducting Magnet

A uniform magnetic field is required by the drift chamber in order to achieve high momentum and mass resolution. The superconducting magnet produces a magnetic field of 1.5 Tesla, which is uniform in the drift chamber to within $\sim \pm 2\%$.

The magnet is a superconducting solenoid which is housed inside the IFR, see Fig. 2-13. Supercooling with liquid helium provides an operating temperature of 4.5K.

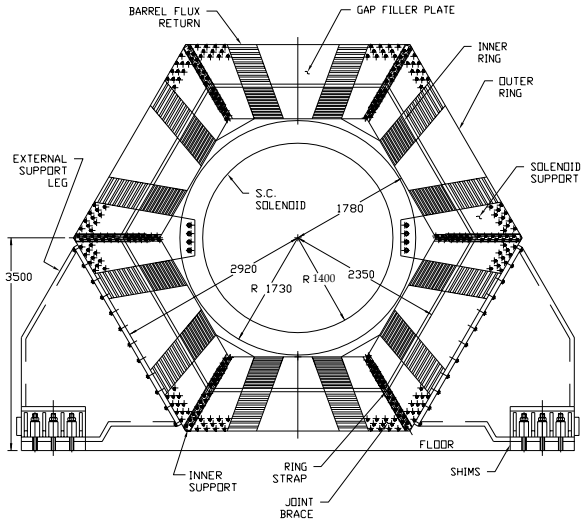

Figure 2-13. *Diagram showing the superconducting magnet housed inside the IFR, (end view).*

2.10 The Trigger

Event selection for physics analysis is controlled by the trigger [33]. The trigger rate must be limited by the data acquisition system bandwidth (2 kHz), and the maximum capacity for data storage, with a rate of 100 Hz. The primary performance measure of a trigger system is its efficiency for benchmark physics processes. The Level 1 trigger system is designed to achieve very high efficiency and good understanding of the efficiency. The

charged track trigger requires at least two tracks in the drift chamber: one long track with $p_{\rm t} > 0.18$ GeV/c and one short track with $p_{\rm t} > 0.12$ GeV/c. The energy trigger requires two clusters in the electromagnetic calorimeter, both with reconstructed energy deposits above a threshold that is efficient for muons. The orthogonality of the requirements allows good cross-calibration of trigger efficiency. Under nominal background conditions, this 'open trigger' is simulated to produce a rate of 1.5 KHz, while yielding 100% efficiency inside the fiducial region of the detector for B and τ physics and $> 99\%$ for $\gamma\gamma$ physics.

There are three drift chamber trigger objects: long tracks, short tracks and long tracks with a configurable cut on $p_{\rm t}$. The calorimeter trigger reports three main trigger objects, corresponding to three configurable energy thresholds for clusters. The energy lowest threshold object defaults to $> 0.12\,\mathrm{GeV}$.

The global trigger selects events using any combination of these objects, using requirements on the number of objects, optionally subject to separation cuts in azimuth and to matching between tracks and clusters.

The complete trigger consists of both hardware (Level 1) and software (Level 3) components. The Level 3 trigger consists of a range of tools for reducing backgrounds while maintaining the selection of good physics events. A hierarchy of increasingly complex algorithms obtain accurate precision on track impact parameters from the Level 1 trigger track segments, the drift chamber hits and the silicon vertex tracker hits. The Level 3 trigger is not expected to reduce significantly the efficiencies provided by Level 1. If machine backgrounds become so high that Level 1 trigger rate exceeds the data acquisition limit of 2 kHz then a Level 2 trigger will become necessary.

2.11 Summary

The physics goals for the programme of CP violation studies in the B meson system has placed stringent requirements on the design and performance of the PEP–II B Factory

and the BABAR detector. The key aspects of this design have been described, and some details of the requirements of each subsystem have been provided.

3

Crystal Production and Quality Control for the BaBar Calorimeter

3.1 Introduction

The CsI(Tl) crystals for the electromagnetic calorimeter were supplied from several commercial crystal manufacturers. The production of crystals is described with reference to one of the crystal manufacturing companies commissioned by the BABAR Experiment – Hilger Crystal Materials. The techniques traditionally employed by the company for growing crystals required re-examination, and considerable development, in order to provide crystals of the correct specification for BABAR, and methods for quality assurance and control have been implemented at all stages of production. A particular aspect of crystal growth - seed quality - has been studied in detail. In addition, specialised crystal tuning techniques have been designed in order to ensure that the crystals conform to the required levels of light output and uniformity.

The research work undertaken at Hilger took place in the context of a busy manufacturing environment facing challenging production targets and deadlines. Material shortages were also significant throughout the project, which limited the availability of samples for study. The primary objective of this work, and main contribution to the project, was to improve the yield of crystals of adequate quality through studies of the complex crystal growing process. All of these factors necessarily compromised the rigour and depth of the research

methodology, since changes which were identified as potentially beneficial were often implemented before thorough studies to establish cause and effect had been carried out.

3.1.1 The Requirements of BABAR

The supply of crystals for the BABAR calorimeter was managed through contracts with several commercial companies (Crismatec, Kharkov, Beijing, Hilger). This was both necessary and desirable, since no single manufacturer was capable of meeting the entire production schedule, and a distribution of the production allowed some flexibility in the allocation of production targets throughout the duration of the project.

Hilger was responsible for the production of 10% of the barrel (500 crystals) and 50% of the endcap (400 crystals). This constituted production of 18 different sizes and shapes of trapezoidal crystals, ranging in length from 30 cm to 32.5 cm. The monthly production targets set by BABAR detailed the number of each type of crystal to be produced, with typically several different types of crystal required for a particular shipment. This was necessary for the overall project schedule in order to assemble the electromagnetic calorimeter module-by-module in a timely way, since each individual module contained several types of crystal. It did however, place additional time constraints on production, due to the lead time involved in re-tooling machinery for crystals of different types.

There are two important quality criteria for the BABAR electromagnetic calorimeter : the crystals must have excellent light output properties, and they must be have adequate radiation hardness in order to withstand the radiation environment of the experiment for a number of years. The addition of Thallium as a dopant to CsI(Tl) considerably improves the light yield, however, Thallium-doped CsI(Tl) is less radiation hard than pure CsI [34]. The most significant factor in determining the radiation hardness of a given crystal is the raw material used to produce it, since impurities can dramatically affect the scintillation properties [35][36]. Thus, in order to ensure some level of consistency in

the crystal quality between companies, the raw material, CsI salt, was supplied to all the manufacturers from a single source (APL).

3.1.2 The Capabilities of Hilger

Hilger Crystal Materials manufactures synthetic crystals for use in infra-red imaging and radiation detection applications. The company has over 60 years experience of crystal growing, and has specialised in the production of small, high quality crystals for optical instrumentation. CsI(Tl) crystals have been produced since 1975. The BABAR project presented the Company with a series of new challenges which placed considerable demands on the existing production methods. This resulted in a need for extensive re-evaluation and re-design to be undertaken. Two key aspects of the BABAR contract can be identified as significant : Firstly, the large dimension (especially length) of the crystals was beyond Hilger's previous manufacturing capability, which generated a number of technical problems. Secondly, the BABAR contract required a much greater rate and volume of production than historically, resulting in new issues of capacity and production management.

In preparation for BABAR production a number of new and existing resources were allocated to the project. These included 5 new furnaces and 11 existing furnaces, and a dedicated clean room with a full-time technician for crystal quality checks, tuning, dimensioning and wrapping.

3.2 The Crystal Growth Process

The CsI(Tl) crystal growth process is one of melt flux growth under gravity, and is based on the traditional Kyropoulus Method [37]. A diagram showing the typical arrangement of a Hilger furnace employing this method is given in Fig. 3-1. CsI salt, with Thallium added as Thallous Iodide, is heated in a ceramic crucible inside the furnace to an initial

temperature of 700°C. The furnace is covered with a metal cap so that the melt is enclosed. This helps to limit Thallium evaporation, and to maintain a Nitrogen-enriched atmosphere[1]. A seed crystal is secured inside a chuck and lowered onto the melt surface to melt off its bottom face. Its vertical position is then adjusted until surface contact is just maintained. The crystal grower ensures that full contact is made by checking for an unbroken meniscus around the seed – this is done by eye with the aid of a torch through a small observation window in the furnace lid.

Controlled cooling of the melt then takes place, at an initial rate of 5°/hour until the CsI melting point temperature of 621°C is approached. Once the first growth has been established, and the crystal is about 12 cm in diameter, the temperature gradient is reduced to 0.5°/hour. When the crystal diameter is close to the diameter of the crucible, the temperature gradient is further reduced to 0.1°/hour. The process up to this point takes about one week to complete. The crystal boule[2] is then allowed to cool naturally to room temperature, which takes a further week. The crucible must then be broken to remove the boule.

Several variations of the Kyropoulus Method are used in practice: the seed may be pulled slowly from the melt as the crystal forms, or allowed to emerge naturally as the surface level of the melt falls due to accumulation of solid material. In some processes the seed is rotated slowly during growth, as this helps to reduce effects from temperature fluctuations in the melt, and allows a slower and steadier rate of crystal growth.

3.2.1 Issues with the Growth of Crystals for BABAR

Prior to the BABAR contract, Hilger was able to demonstrate its capability to grow boules which could yield trapezoidal crystals of up to 25 cm in length. These crystals were

[1] the uptake of oxygen by CsI(Tl) is thought to contribute to poor radiation hardness

[2] the term *boule* refers to the large crystal grown in a furnace, from which one or more BABAR trapezoidal crystals are cut

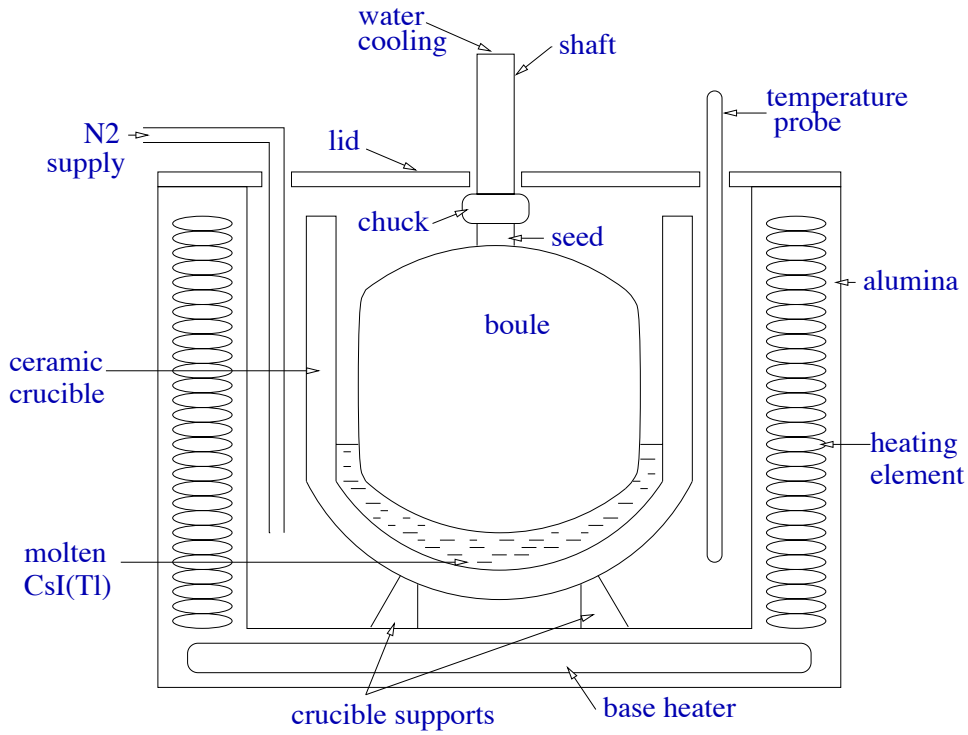

Figure 3-1. *Diagram of a crystal growing furnace at Hilger using the Kyropoulus Method.*

obtained from vertical sections through a boule. Following this, attempts were made to grow larger boules in the existing furnaces (of diameter 16 inches), but although boules of the required depth were attained, a length limit for trapezoidal crystals was imposed by the presence of unacceptable impurities and polycrystalline regions at the base of a boule. These features were a result of the power of the heating elements and resulting temperature profiles of the existing furnaces, rather than their physical size.

As a result, Hilger opted to design a new set of furnaces dedicated to BABAR production, with a greater capacity (of diameter 20–22 inches), so that wider boules could be accommodated, and BABAR crystals of the required length could be cut horizontally from the top of the boule where the crystal quality was consistently highest. It was estimated that production targets could be met if a yield of 2-4 BABAR crystals/boule could be achieved.

The decision to modify the method of producing crystals necessarily raised issues concerning the properties of the resulting BABAR crystals. The prototype crystals supplied to BABAR by Hilger prior to the start of production were cut vertically, and the properties of these crystals had been assessed. However, the new method produced crystals whose properties were not known *a priori*. The most significant effect on the crystal properties was due to the differences in the amount and distribution of Thallium which occur in a horizontally-cut crystal compared to a vertically-cut crystal. The uptake of Thallium by the boule during growth is sensitive to ambient conditions, and needs careful monitoring to obtain some level of consistency of doping throughout the crystal. Thallium has a much lower melting point (440°C) than CsI, so it evaporates rapidly from the melt. However, a more dominant factor in the absorption of Thallium is the preference of a crystal to maintain its lattice structure, and remain pure. So, during the initial growth phase, the abundance of CsI allows the crystal to grow with little Thallium uptake, so that the relative concentration of Thallium to CsI increases as the melt is used up. Thus, there is a gradient of Thallium concentration within the boule which is dependent on its growth over time. In particular, the lowest concentration of Thallium is at the top of the boule. The horizontally-cut crystals from the top of a boule had both a lower overall Thallium concentration, and a more uniform profile than vertically-cut crystals, affecting both light output and uniformity properties. This had consequences for the crystal tuning process, described in section 3.5.

Another feature of the crystal growth process which has been limited by the increased size of boules is that of rotating the seed during growth. It was found that using rotation caused the seed to shear when the boule approached full-grown size. It was not known whether this was due to resistance due to the high viscosity of the melt at this point, or from the boule coming into contact with the sides of the crucible. In the event of a seed breaking, the falling boule would tend to damage the furnace beyond repair, and clearly such a situation must be avoided. Two solutions were adopted to overcome this problem: seeds of increasing diameter were tested (30, 50, 75, 90 mm), with the largest of these being

chosen for future production, and rotation was stopped before the boule approached full size. However, stopping the rotation during boule growth created a sudden increase in growth rate, resulting in poor crystal structure. Therefore, rotation was stopped just after initial growth had been established.

3.3 Seed Quality

The structural quality of a given boule depends strongly on the quality of the seed used to grow it. It is essential that the seed has a single crystal structure, with no inherent defects, at the face from which the boule is grown. Both the intrinsic quality of the seed, and the way it is handled at various stages of production, are significant. Several aspects of seed quality were investigated to determine where improvements could be made in the production of boules. Seeds for growing new boules are obtained routinely from the offcuts of old boules, if these are suitable, or occasionally from a dedicated boule which has been grown purely for making seeds. In a situation where the availability of good quality crystal material becomes scarce there is a compromise between the pressure to meet production targets and the need to maintain a good stock of seeds. If general seed quality is allowed to degrade then this leads to worse overall crystal yield, and so on.

The orientation of the crystal lattice in the seed used to grow a given boule is known to play a major role in the resulting pattern of growth [37]. CsI has a body-centred cubic structure, and has no natural cleavage planes. The orientation of the cubic crystal lattice with respect to the bottom face of a seed is of interest, since this is the face from which the boule grows. There are three possible simple orientations which can be defined. These can be identified using the notation of Miller indices as [100], [110] and [111], and are illustrated in Fig.3-2.

The rate of growth of a crystal depends on the lattice orientation, since the crystal will tend to growth most rapidly in directions parallel to its lattice planes, where the least change

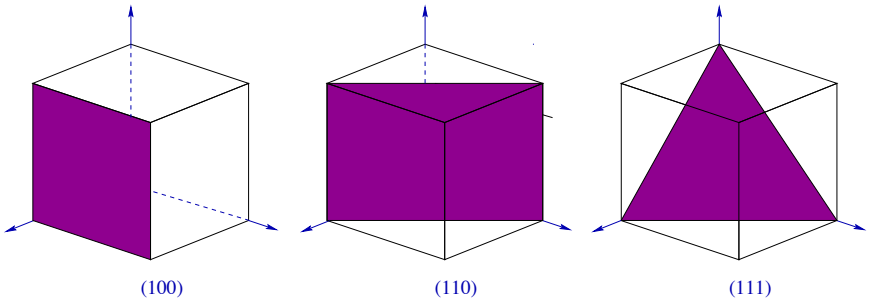

Figure 3-2. *Orientations and Miller Indices for a cubic crystal lattice[38]: the shaded surface represents a surface parallel to the bottom face of the seed, and the cube shows the relative orientation of the crystal lattice.*

in binding energy occurs from the adsorption of atoms to the surface[37]. The [111] orientation clearly represents the case of highest symmetry, and a seed with this property will tend to grow with more radial uniformity than seeds with different orientations. As CsI has no cleavage planes, the lattice orientation is identified by manually indenting the surface of the seed with a sharp object to produce cleavage lines. The appearance of three radial lines with similar length and opening angles is an indication of [111] orientation, (this can be visualised from Fig.3-2 if looking directly at the bottom face of the seed). All seeds were required to have the [111] property.

3.3.1 Factors Affecting Seed Distortion

An ideal seed would consist of a single crystal, *i.e.*, with the crystal lattice intact throughout. This is best achieved in practice by ensuring that the seed is as small as possible, as larger seeds are more likely to have a variety of non-uniformities in their structure, and these are passed on in the subsequent crystal growth. However, a strong constraint is placed on the size of the seeds used to grow the large CsI(Tl) boules, as the seed must be capable of supporting the weight of the fully grown boule. It is unfortunate that such a purely mechanical constraint should compromise the level of consistent crystal quality which can be achieved, but there appear to be no other means of supporting the

boule during the growth. The increase in seed size which has been necessary for the BABAR production has resulted in a greater occurrence of seeds with imperfections in their structure.

A cylindrical seed of CsI was secured in a chuck using three grub screws, which are positioned evenly around its circumference. Usually, the seed was enclosed in a brass sleeve for protection, so that the screws did not cause any deep indentations in the material. However, all seeds which were inspected after completion of boule growth showed significant indentations and marks. Seeds were further examined under polarised light, in order to highlight any internal distortions due to the indentations. Among the seeds studied, a correlation was seen between the occurrence of distortion and the relative orientation of the crystal lattice to the position of the indentations. When an indentation coincided with an edge of the lattice the seed had developed a polycrystalline structure originating from that point; the boule made from such a seed was also polycrystalline. The evidence for this effect was somewhat anecdotal due to the small number of seeds which were available for study, so no firm conclusions could be drawn. A new design for the seed and its support was recommended and implemented, in which the seed and brass sleeve were slightly tapered towards the base, so that the applied load was spread more evenly.

3.3.2 Investigation into the Cause of Tilted Boules Using Seed Properties

One of the significant causes of low yield during production was the occurrence of boules growing with their top face tilted at an angle to the horizontal. Examples of non-tilted and tilted boules are shown in Figs.3-3 and 3-4.

The effect of tilt was to reduce the size of the region at the top of the boule from which BABAR crystals were cut, due to regions of undercutting (indentations in the sides of the boule) developing during crystal growth. If the tilt angle was larger than $\sim 30^{\circ}$ then no

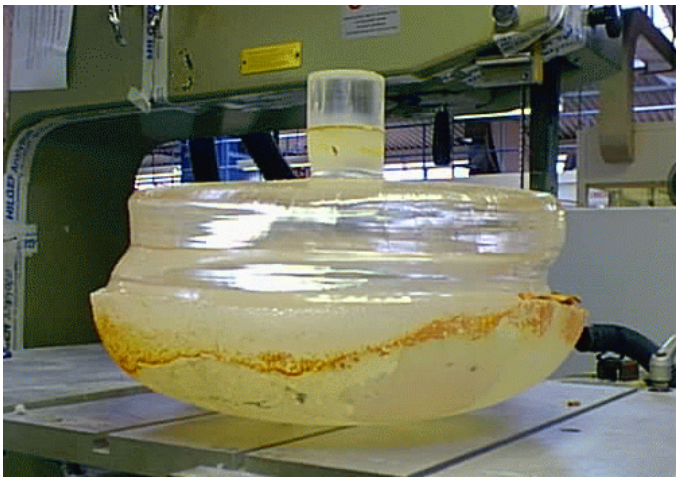

Figure 3-3. *Example of a boule which does not suffer from "tilt".*

Figure 3-4. *Example of a boule which suffers from moderate "tilt"; a region in which undercutting has occurred during crystal growth is clearly shown on the left-hand side of the boule.*

BABAR crystals could be obtained. This situation occurred in about 20% of cases. Also, boules with large tilt tended to be polycrystalline as a result of their uneven growth.

In order to address this problem, several possible causes of tilt were identified and studied. The initial focus of the investigation was on factors which may affect the orientation of the crystal lattice in the seed during growth, since this is known to cause a preferred growth direction; the resulting uneven distribution of weight may in turn pull the boule down on one side. As part of this study, 23 seeds were collected after boule growth. While a seed was still attached to a boule, a scoreline was marked around the seed (using a pair of callipers) which was parallel to the top surface of the boule, indicating its tilt. The seed was then detached from the boule. The lattice orientation of each seed was checked against the tilt direction, but due to the uncertainty and poor repeatability of the method used to identify lattice orientation (described in section 3.3), there was found to be no clear relationship. However, it was noted that five of the seeds had a characteristic ridge (lack of meniscus) at their base, which indicated that full contact had not been achieved between the seed and the melt during growth. (Other seeds in the sample had been cut too high from the boule so the information was lost). A diagram illustrating the scoreline and ridge on a typical seed is shown in Fig.3-5.

For each of the five seeds, the vertical distance from the top of the seed to the tilt scoreline was measured at intervals around the circumference. The location of the ridge was also noted. The results are shown in Fig.3-6, where the region between the dotted lines indicates the ridge location on the seed circumference. The results show that the boule tilt was aligned with the ridge position, with the highest point on the side of the ridge. This is consistent with the growth rate for the boule being much higher on the side opposite the ridge, where good contact was achieved, with the tilt resulting from the consequent uneven weight distribution.

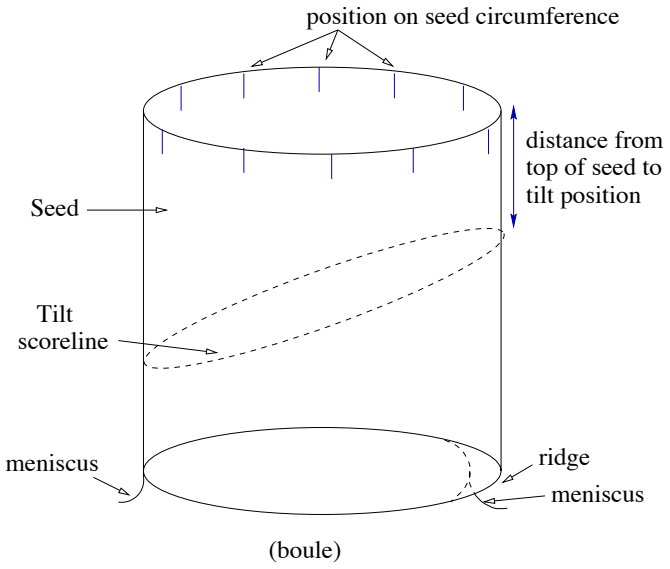

Figure 3-5. *Schematic diagram of a seed (sideview) showing "tilt" and "ridge" information.*

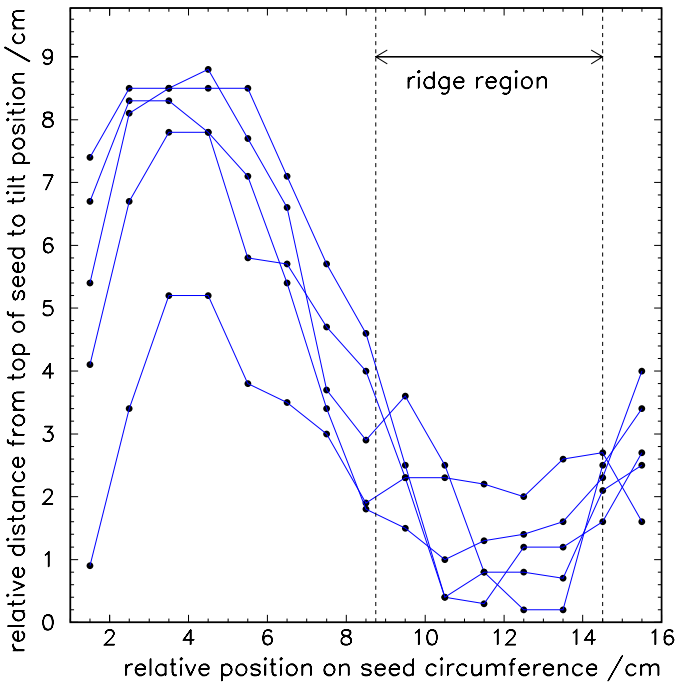

Figure 3-6. *Plots showing the correlation between the direction of boule tilt and the position of an undercut (ridge) region at the base of a seed.*

The results of this study were discussed with crystal growers, so that extra care could be taken in checking for full seed contact with the melt prior to crystal growth. No further cases of badly tilted boules were reported.

3.4 Cutting, Dimensioning and Polishing BABAR Trapezoidal Crystals

Following the crystal growth process, a boule was extracted from the furnace using a mechanical lifting device, and placed on a platform for visual inspection. A torch was used to highlight possible defects, such as polycrystalline regions or the inclusion of impurities. At this stage, any region suitable for yielding a trapezoidal crystal was mapped out. Also at this stage, in order to carry the seed studies discussed in the previous section, the crystal grower was asked to mark the seed orientation relative to the boule before the seed was removed.

The boule was then passed to a horizontal milling machine where it was cut into rough blocks from which the trapezoidal crystals would be produced. Several custom-made jigs were required for each trapezoid type in order to cut the faces at the correct angles. A jig was mounted onto the milling machine platform using a vacuum seal, and a block was placed on top of this so that the required angle of cutting was achieved. The milling machine cutting head was then driven slowly across the surface of the block. Milling was continued in such steps until the trapezoid was of the correct shape, and about $2\,\mathrm{mm}$ oversize in each dimension.

A polishing surface was prepared using a chamois leather cloth dampened with water and placed on a polishing block. Each face of a trapezoidal crystal was then wiped firmly across the surface with repeated strokes. The high solubility of CsI in water resulted in a saturated solution of CsI developing in the cloth, and this proved to be a highly effective system for polishing the crystal surface. The initial over-sizing of the trapezoids at the cutting stage allowed for some loss of material during the polishing stage.

Each crystal was then precisely dimensioned using a purpose-built rig which placed eight position gauges at key points around the crystal and compared the values obtained with those of a template crystal. The crystal was then wrapped in two layers of Tyvek, and one layer of aluminium foil, and placed in a dark storage area prior to tuning.

3.5 Tuning Methods for Crystal Quality Control

In order to maintain good energy resolution and linearity in the BABAR electromagnetic calorimeter, it is necessary for the crystal light response to be uniform over the entire crystal axis. In addition, the crystals must have high absolute light yield. The bulk effects which contribute to these properties (*i.e.*, single crystal structure and Thallium concentration) have been discussed in previous sections. There is also a contribution from surface effects, and this can be used to "tune" the crystal properties to within specifications. The tuning process is one of fine adjustment, and cannot be used to compensate for very poor bulk properties.

Both the light yield and the uniformity of a crystal were measured using purpose-built apparatus. The original design of this apparatus for all the crystal suppliers took place at SLAC. The version for Hilger was built and commissioned entirely at Brunel University. Following this, the apparatus was transported to Hilger, and comprehensive training in its use was provided. A diagram of the apparatus is shown in Fig.3-7. It consisted of a radioactive source (Na22, 10 μCi) in a light-tight box with a photomultiplier tube for readout. The radioactive source was mounted on a motor-driven vertical axis so that it could traverse the length of a crystal automatically.

The procedure for measuring both light yield and uniformity required placing a crystal wrapped with Tyvek and aluminium foil inside the light-tight box above the photomultiplier tube. The radioactive source was moved along the crystal axis, and the light output from the base of the crystal was recorded. A LabView interface was provided via a data

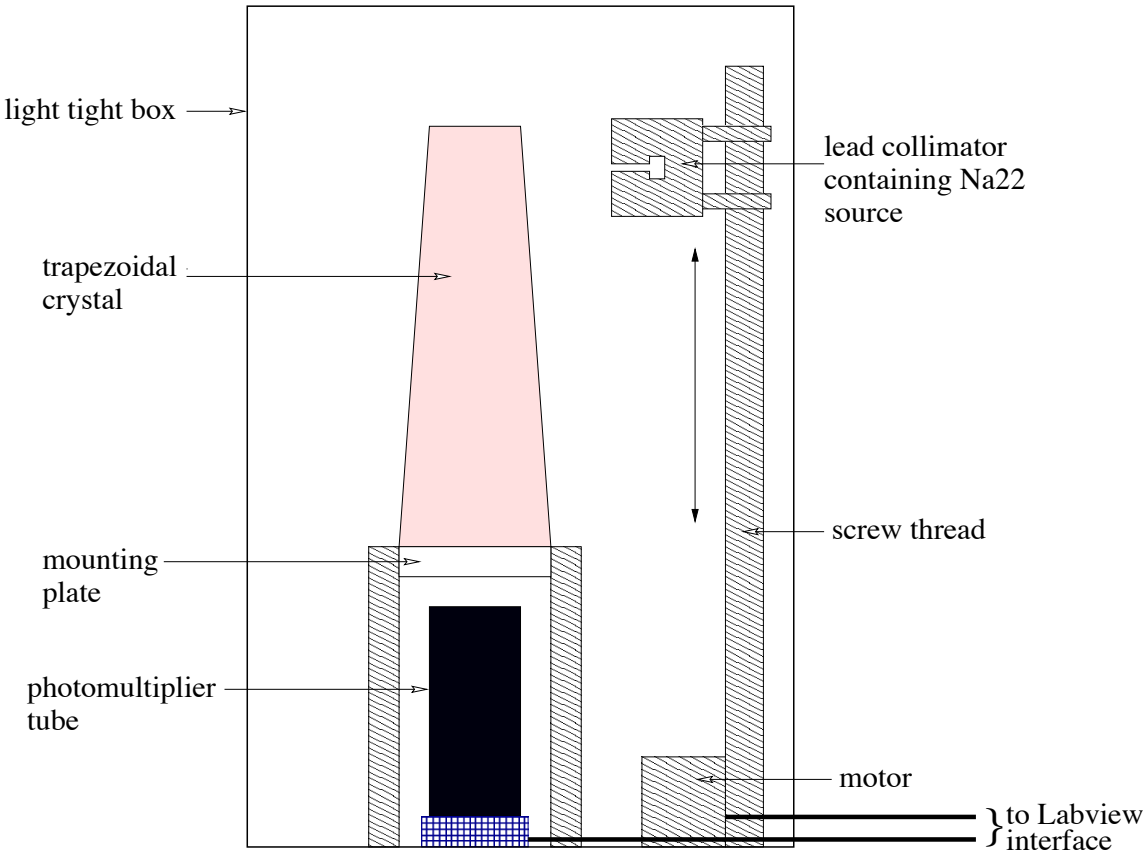

Figure 3-7. *Diagram of the apparatus used to measure light yield and uniformity for a crystal.*

acquisition system so that light output as a function of distance along the crystal could be recorded and plotted. Some examples of these plots are shown on the following pages.

In order for a crystal to pass the uniformity criteria [39], the value of its relative light output was required to be constant to within a specified range along its axis. The range was narrower at the top (*i.e.*, front end) of the crystal, where variations in the shower maximum are critical.

3.5.1 Development of Tuning Techniques for the BABAR Crystals

The general procedure for tuning crystals for uniformity is well-known [40]. It involves varying the level of reflectivity/absorption of the crystal surface in selected areas in order to alter the relative amounts of light transmission and reflection at points along the crystal axis. However, for any set of crystals with previously unknown uniformity characteristics, some detailed study with several iterations is needed in order to find an effective and efficient method for tuning. With the high production rates for BABAR crystals, the tuning process needed to be completed at an average rate of no more than two hours per crystal in order to meet production targets, which in turn implied a limit of three uniformity scans per crystal. Initially, the crystals were prepared for the tuning stage in a highly polished state, so that a high overall light yield could be obtained. However, these crystals were found to have very poor uniformity, and they were also very insensitive to attempts to correct for this using blackened areas on the surface to increase absorption levels. The high polish effectively allowed the path length of light inside the crystal to be so large that any local effects were dissipated. Crystals were also found to exhibit large variations in their light output properties over time. This was traced to the way in which they were handled prior to tuning, as the exposure of CsI(Tl) to light causes excitation which can last several hours. To remedy this situation, the crystals were stored in a light-tight box for at least 24 hours prior to their first uniformity scan.

An effective tuning procedure was then developed in which the surface of a crystal was roughened in small areas, using fine sandpaper. This was found to have a strong influence on the uniformity. The areas for roughening were identified from an initial uniformity scan of a crystal. Roughening the crystal surface in a given area tended to reduce the light yield contribution from points above it. This allowed regions which had lower than average light yield to be brought closer to the new average. The overall light yield was reduced by this process, so it remained important to limit the amount of roughening to the minimum necessary to achieve acceptable uniformity, while also keeping the number of

scans per crystal as low as possible. The sample plots on the following pages are typical results from the tuning process. They demonstrate the effectiveness of the method, since only two scans ("before" and "after") were needed in each case to achieve the uniformity required by the BABAR specification (indicated by the region between the dashed lines on each plot).

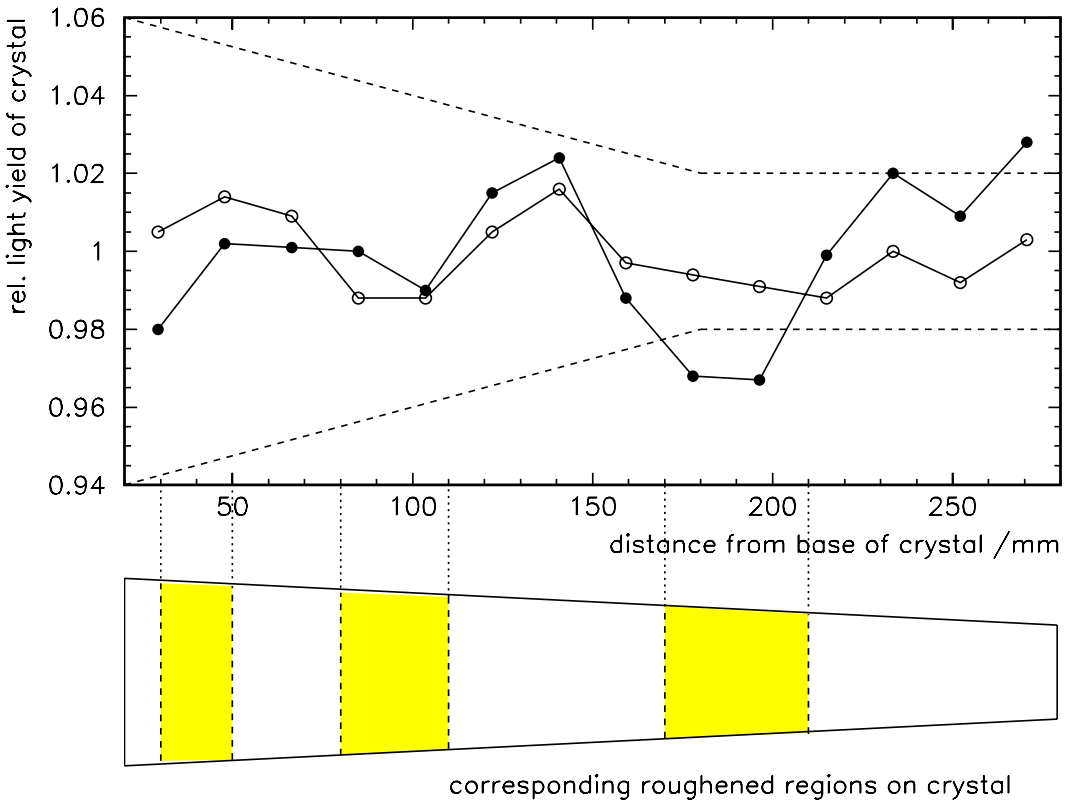

Figure 3-8. *Uniformity scans for a crystal showing variation of relative light yield with distance along crystal axis, before tuning (black points) and after tuning(white points). The limits of the BABAR quality specification are given by the dashed lines.*

In Fig.3-8 three areas of relatively low light yield were identified and roughened. The distribution of the points after tuning show how these areas have increased their relative light yield with respect to the average light yield of the crystal.

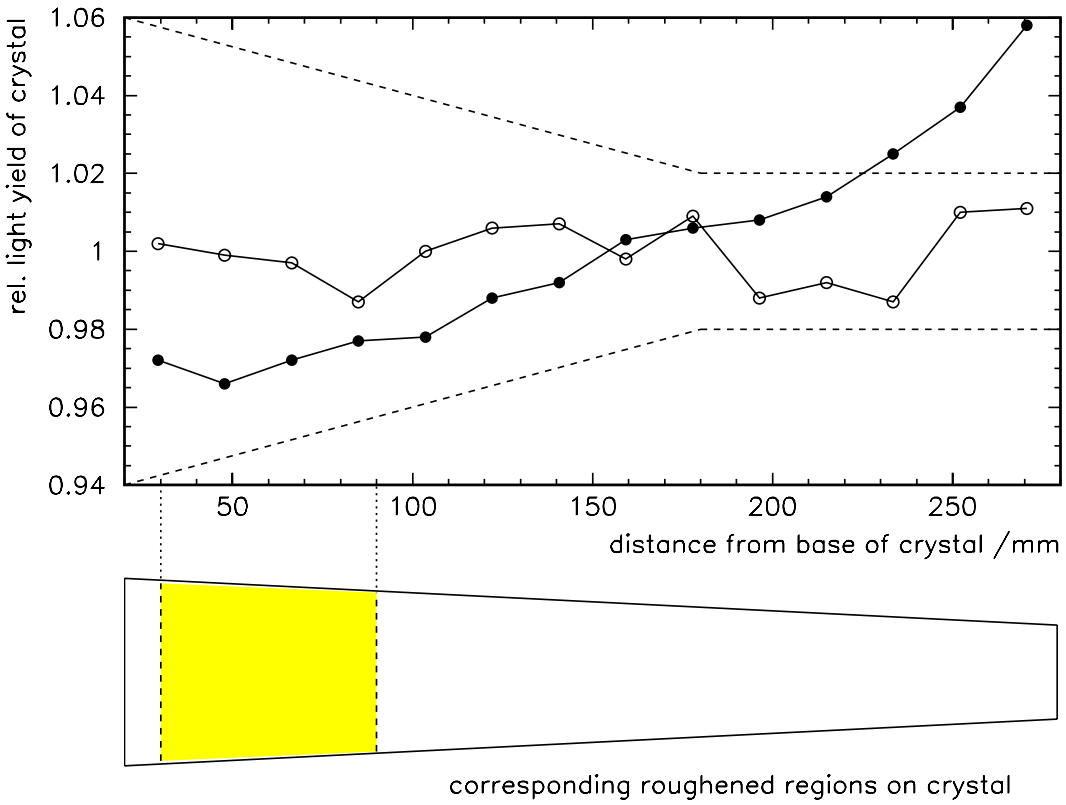

Figure 3-9. *Uniformity scans for a crystal showing variation of relative light yield with distance along crystal axis, before tuning (black points) and after tuning(white points). The limits of the BABAR quality specification are given by the dashed lines.*

In Fig.3-9 the crystal showed an initial uniformity scan which rose almost monotonically from the base to the top of the crystal. This characteristic was commonly observed in Hilger crystals, and was corrected by roughening a broad band near the base of the crystal.

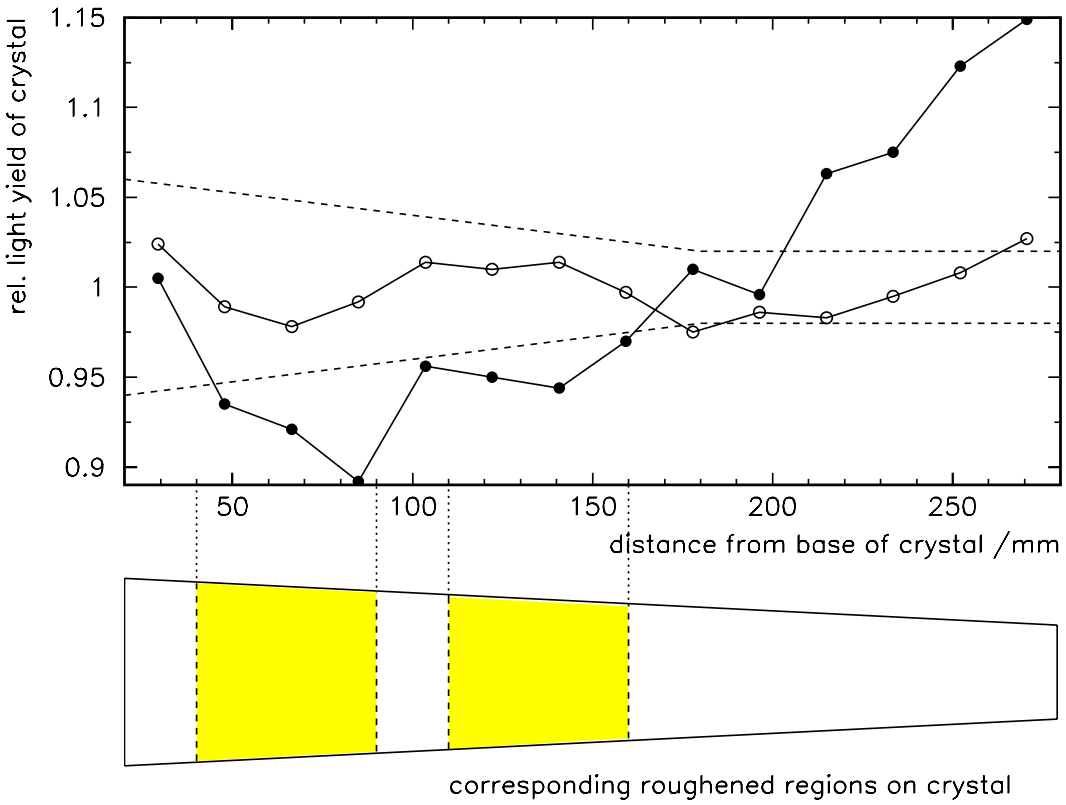

Figure 3-10. *Uniformity scans for a crystal showing variation of relative light yield with distance along crystal axis, before tuning (black points) and after tuning(white points). The limits of the BABAR quality specification are given by the dashed lines.*

In Fig.3-10 the crystal showed considerable non-uniformity prior to tuning, and two regions were roughened in order to improve uniformity. Following the tuning process uniformity of the crystal was much improved, but still slightly outside the specified tolerance bands. The crystal was deemed to be acceptable, however.

3.6 Summary

The work carried out for the production of crystals for the BABAR electromagnetic calorimeter at Hilger Crystals Materials has been discussed. Improvements to the crystal growing process were gained through investigations into the quality of crystal seeds. The equipment and techniques for tuning crystals to BABAR specifications were provided and developed, so that an efficient and reliable method for tuning was achieved.

4

Tools for Background Suppression in Physics Analyses

4.1 Introduction

The issue of background suppression is an important one for BABAR, where typically the branching ratios for the channels of interest are small. The challenge is to achieve background rejection of the order of 10^{-5}, or better.

Many sophisticated techniques and discriminating variables have been developed for background suppression in previous experiments. These are well known, and applicable to a range of channels. The BABAR experiment will operate in a unique environment, with the large boost and need for high precision vertex resolution to reconstruct B decays. The traditional background suppression methods have been reviewed in this context, and a set of tools has been developed to exploit the most useful discriminating variables.

The tools have been designed for a general procedure of discriminating signal from background in any analysis. The method described here has provided the means for employing a consistent approach to handling the variables across a range of analyses. It has also assisted with the data management issues present in dealing with the large number of events required for background studies. The tools have been applied to a particular channel, $B^0 \rightarrow \pi^+\pi^-\pi^0$, and this is presented as an example to illustrate the results which can be obtained.

4.2 Nature of the Backgrounds

Several sources of background can contribute to an analysis, and the issues associated with background rejection depend on the particular combination of detector and machine characteristics, and the features of the channel under study. The backgrounds can be categorised into various types: continuum, combinatorial within signal events, background from other B modes, and machine background. Each of these is described below. Methods for suppressing continuum background have been studied in detail, and are reported in the subsequent sections of this chapter.

4.2.1 Continuum Background

For the e^+e^- collider, operating at the $\Upsilon(4S)$ resonance, the expected relative abundances of $q\overline{q}$ pairs near the nominal energy are given in table 2-2. The relative rates reflect the dependence on the square of the quark charge, and additionally the $\Upsilon(4S)$ enhances $b\overline{b}$ production by approximately a factor 3. Fig. 2.3 shows the profile of the continuum and the $\Upsilon(4S)$ resonance in the region of the nominal centre-of-mass energy for PEP–II.

4.2.2 Combinatorial Backgrounds

Combinatorial backgrounds arise in both signal events and continuum events, due to wrong combinations arising in the signal reconstruction process which possess the desired signal properties. The term “combinatorial background” is taken here to mean the combinatorics from signal events, as combinatorics within continuum background is assumed. Combinatorics are particularly high for channels involving one or more neutral particles, as there is a significant number of calorimeter energy deposits in each event which can combine to form a viable reconstructed candidate. This is a particularly serious issue

for π^0 reconstruction. Some events, especially, contain a large number of low energy deposits in the calorimeter which can create a high multiplicity of B candidates which satisfy the signal pre-selection criteria. The most effective way to suppress combinatorial background is to create a χ^2 based on characteristic signal properties. The candidates can then be ranked according to their χ^2 value, and the candidate with the best χ^2 can be selected from each event. This method is superior to applying a hard cut on the discriminating variables, as it maintains higher efficiency. As an example, the χ^2 of pre-selection variables for the $B^0 \to \pi^+\pi^-\pi^0$ channel is formed from the π^0 reconstructed mass,M_{π^0}, the B^0 mass,M_B, and the B^0 momentum in the $\Upsilon(4S)$ rest frame, $p^*{}_B$,

$$\chi^2 = \frac{M_{\pi^0}^2}{\sigma_{\pi^0}^2} + \frac{M_B^2}{\sigma_B^2} + \frac{p_B^{*2}}{\sigma_{p_B^*}^2} \tag{4.1}$$

where the σ^2 have been estimated from fits to large samples of signal Monte Carlo events, (note that this introduces some systematic errors into the selection process).

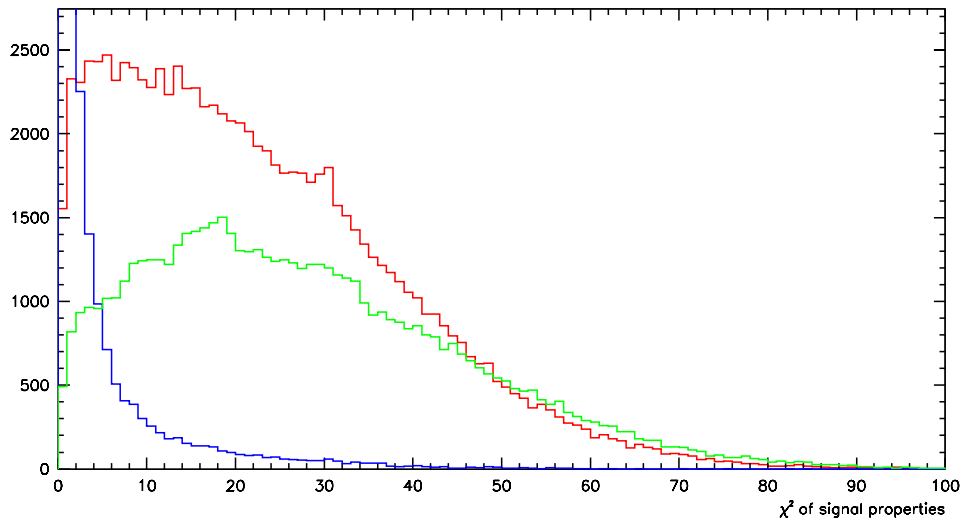

Figure 4-1. *Distributions of a χ^2 of signal properties, for signal (blue), combinatorial background (red), and (not normalised) u, d, s continuum background (green).*

The χ^2 distributions for signal, combinatorial background and continuum background are shown in Fig.4-1. The performance of a cut on this χ^2 for maintaining signal efficiency is discussed further in section 5.4.

4.2.3 Physics Channels

Backgrounds from physics channels which are similar to the channel under study fall into two categories: those which have no CP asymmetry, and those which contribute events having the same or opposite CP asymmetry to the channel under study. An example of this is seen in the study of the $B^0 \to J/\psi K^0_L$ mode, which has background contributions from both $B^0 \to J/\psi(K^{*0} \to K^0_L\pi^0)$ and $B^+ \to J/\psi K^{*+}$, $K^{*+} \to K^0_L\pi^+$. The K^{*+} mode has zero CP asymmetry, and therefore it affects the total statisitical power of the CP measurement, but does not dilute its value. The K^{*0} mode, however, has opposite CP to that of the signal, so that the measured CP asymmetry is diluted by inclusion of this background in the selected sample, (a detailed discussion of the effect on CP reach for this channel is given in [13]).

B decay modes containing several pions and/or kaons are the main physics background for the $B^0 \to \pi^+\pi^-\pi^0$ channel. The main tool for dealing with such physics backgrounds is efficient PID, so that effective K/π separation is possible. The results of some simple studies of physics backgrounds are given in the next chapter, section 5.3.1. The results of applying PID techniques can be combined to form discriminating variables for use in multivariate analysis, *e.g.*, $\sigma_{\pi^+K^+}$ and $\sigma_{\pi^-K^-}$. Such variables could represent, for example, the probability that a given particle was a π^+, or could simply be a boolean value set according to whether a particle passed or failed a given PID selection process.

4.2.4 Machine Backgrounds

The special design requirements for $PEP\text{-}II$ (described in section 2.2) are expected to create significant machine-induced backgrounds. The main sources of these backgrounds are beam gas interactions, synchrotron radiation, and elastic and radiative Bhabha scattering. These are expected to increase the occurrence of low energy clusters in the electromagnetic calorimeter, which in turn will increase the combinatorial background for neutral particles.

Close attention has been paid to engineering design issues, such as effective shielding, and efficient triggering, in order to limit the effects on machine-backgrounds, which can degrade physics reconstruction, both in the short-term (*e.g.,* saturation due to high occupancy), and in the long-term (*e.g.,* detector degradation due to radiation damage). Since the *Technical Design Report* **??** the estimates of machine-backgrounds have increased by more than a factor 10. The effects of machine-backgrounds are still uncertain to a great extent, and will only be understood when $PEP\text{-}II$ has run for some time. This constitutes a large topic for study, which has not been the focus of the work described here.

4.3 Criteria for Continuum Identification

A powerful method for discriminating signal events from $q\overline{q}$ background events exploits the differences in their characteristic topologies. In a true signal event, the primary e^+e^- produce a $B\overline{B}$ pair via the $\Upsilon(4\mathrm{S})$ resonance. In the $\Upsilon(4\mathrm{S})$ rest frame the Bs have low momenta, and so the decay of each B is fairly isotropic. An additional feature of a signal event is that there is negligible correlation between the directions of the decay products coming from each of the two Bs.

In a light quark (u, d, s) continuum event, however, the event shape has a pronounced two-jet structure, and so there is a strongly preferred direction characterising the whole event.

The B "candidates" from such an event will therefore tend to have less isotropic decay shapes in the $\Upsilon(4S)$ rest frame, and there will also be correlations between the directions of the candidate decay products of the two Bs, since they will tend to lie within the two jets.

In a $c\overline{c}$ event the jet structure is still present, but is less pronounced, and so the methods described here using shape variables will provide less discriminating power for this type of background.

A set of discriminating variables used for continuum identification and suppression has been selected. The list is by no means exhaustive, and other variables may be added subsequently. In addition to characteristic shape variables for the event, the list includes properties of the CP candidate, and kinematic variables.

The variables in use are described below. Some of them can be applied generally to any decay, while others require modification according to the number of bodies in the decay. For the two-body case the characteristic direction is clearly defined by the B decay axis. For the three-body case a suitable characteristic direction is the normal to the B decay plane. The best means of calculating these axes depends on the number and type of decay products in the channel under study.

The choice of reference frame is another issue which must be considered. Since it is the discriminating power of a variable which is of interest, the effect of a change of frame need only be viewed in this context, provided the evaluation of the variable remains valid in the chosen frame. For global event variables it is appropriate to use the $\Upsilon(4S)$ rest frame, while for variables using properties of the B decay products the B rest frame is used.

Another consideration when using each of these variables is the choice of the subset of the event to which it should be applied. For some variables only the charged tracks in the event are used, while others apply to all charged and neutral candidates. For

discriminating purposes a variable may be applied globally to the event, or just to the B^0_{CP} decay, or to the tagging B decay. In this study, the tagging B decay products are referred to as the "rest of the event", and a variable which has been applied to the rest of the event is indicated by the subscript R in variable name. All of the event shape variables described here have been calculated for the whole event, and for the rest of the event.

- **B^0_{CP} mass (M_B)**

  In each analysis the CP B decay is reconstructed for each event producing a set of "candidate" particles. The invariant mass distributions of reconstructed B candidates, for signal and $q\overline{q}$ events, are shown in Fig.5-3. As there are no real Bs produced in continuum background events the distribution reconstructed B^0 candidates in these events is to first order uniform.

- **The Momentum of the B^0_{CP} in the $\Upsilon(4\mathrm{S})$ rest frame ($p*_B$)**

  In a signal event, the B mesons have unique momenta in the $\Upsilon(4\mathrm{S})$ rest frame which is smeared by the detector resolution. Whereas the B candidates produced from continuum events exhibit a wide range of momenta. Additionally, the transverse momentum of a putative B is confined to a narrower range for signal candidates than for $q\overline{q}$ candidates, and with a lower average value. The distributions of the CP B candidate momentum in the $\Upsilon(4\mathrm{S})$ rest frame, for signal and u, d, s continuum events, are shown in Fig.4-3. It can be seen that this provides a very powerful discrimination between signal and background.

- **The Momenta of the decay products of the B^0_{CP} ($\cos(\rho\pi)$)**

  The decay products from the B^0_{CP} tend to have high momenta in the B rest frame. This information is used in the PID methods. In addition, the relative orientation of the decay products can provide some discrimination, *e.g.*, for a two-body mode the decay products are back-to-back in the B rest frame for a signal event, while only approximately colinear in $q\overline{q}$ events, due to the jet structure. A variable, $\cos(\rho\pi)$, has been defined for the $B \to \rho\pi \to 3\pi$ channel, which is the cosine of the angle

between the putative ρ and π in the B rest frame. Due to its dependence on the B rest frame, this variable has some correlation with $p*_B$.

- **Sum of transverse momenta of the rest of the event with respect to B direction ($p_t B_R$)**

  For a $q\overline{q}$ event the transverse components of momenta for the rest of the event are small with respect to the B candidate direction, due to the jet structure, whereas for a $B\overline{B}$ event there is no such correlation.

- **Thrust (T)**

  The thrust axis of an event is defined by the unit vector **n** such that the sum of the scalar products of **n** with all the particle momenta has a maximum value. Thrust, T, is related to the maximum value [41] by,

$$T = max_{|\mathbf{n}|=1} \frac{\sum_i |\mathbf{n}.\mathbf{p}_i|}{\sum_i |\mathbf{p}_i|} \tag{4.2}$$

  The allowed range of T is (0.5, 1), where $T \sim 1$ corresponds to a highly directional event, and $T = 0.5$ corresponds to an isotropic event.

  In a typical background event for a two-body decay, the decay products of the B^0 candidate each lie in one of the two jets, and are therefore approximately back-to-back. Thus the decay axis of the B^0 candidate is roughly colinear with the thrust axis for the rest of the event. Whereas, for a true signal event, the B^0 decay axis is essentially uncorrelated with the thrust axis of the rest of the event, which in that case comes from the decay of the other B^0 meson.

  For background discrimination, the cosine of the angle between the thrust axis of the rest of the event and several defined directions for the CP mode is calculated. The following variables were defined :

  – $\cos(TB)$ with the B direction,

  – $\cos(T\pi)$ with the fastest B decay product direction,

  – $\cos(TN)$ with the normal to the B decay plane, for a 3-body decay.

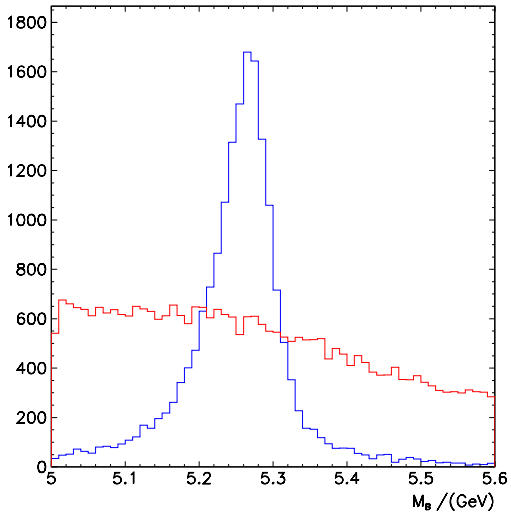

Figure 4-2. *B invariant mass, signal (blue), $q\overline{q}$ u, d, s (red).*

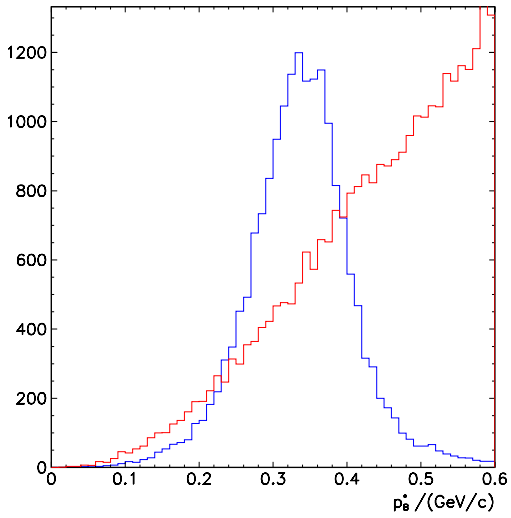

Figure 4-3. *Momentum of the B in the $\Upsilon(4S)$ rest frame, signal (blue), $q\overline{q}$ u, d, s (red).*

The distributions of thrust for the whole event, and the variable $\cos(T\pi)$, are shown for signal and $q\overline{q}$ events in Fig.4-4 and Fig.4-5 respectively.

- **Sphericity (S)**

  As with thrust, sphericity provides good separation of $q\overline{q}$ continuum events and signal due to the jet structure of $q\overline{q}$ events. Sphericity is a measure of the sum of the squares of transverse momenta for each track with respect to the event axis. Defined over the interval (0,1), with highly directional events having low sphericity, and isotropic events corresponding to sphericity = 1. Therefore, the pronounced jet structure of $q\overline{q}$ continuum events allows limited separation with signal to be achieved using this variable.

  Sphericity is defined [42] as,

  $$S = \frac{3}{2}(\lambda_2 + \lambda_3) \tag{4.3}$$

  where λ_2 and λ_3 are the two larger eigenvalues of the diagonalized sphericity tensor,

  $$S^{\alpha\beta} = \frac{\sum_i p_i^\alpha p_i^\beta}{\sum_i \mathbf{p}_i^2} \tag{4.4}$$

  where $\alpha, \beta = 1, 2, 3$ corresponds to x, y, z components.

  The sphericity axis of the system is determined by the direction of the eigenvector corresponding to the largest eigenvalue, λ_1. The sphericity axis of the rest of the event has been used in an analogous way to the thrust axis of the rest of the event to define the following variables:

  – $\cos(SB)$ with the B direction,
  – $\cos(S\pi)$ with the fastest B decay product direction,
  – $\cos(SN)$ with the normal to the B decay plane, for a 3-body decay,
  – $\cos(SS_{3\pi})$ with the sphericity axis of the 3π system.

- **Aplanarity and Planarity (apl, pla)**

  Aplanarity is a measure of the magnitude of the transverse component of momentum of a system out of the event plane. It is related to the smallest eigenvalue of the

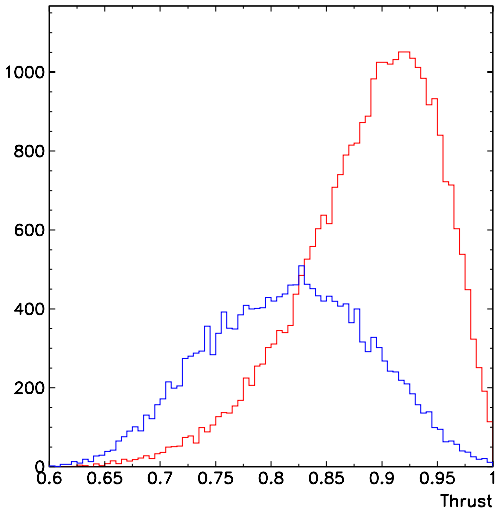

Figure 4-4. *Thrust for the whole event, signal (blue), $q\overline{q}$ u, d, s (red).*

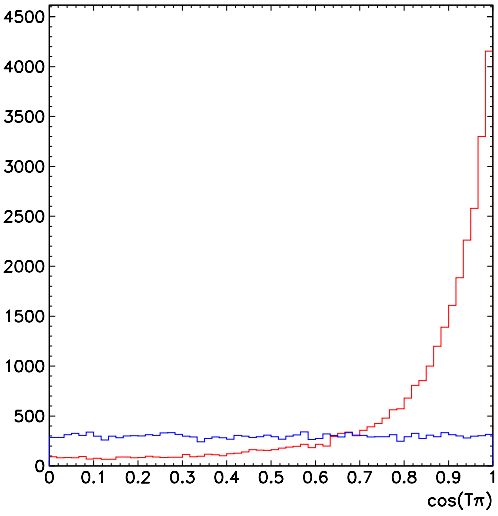

Figure 4-5. *Cosine of the angle between the thrust axis of the rest of the event and the momentum of the fastest pion in the B rest frame, signal (blue), $q\overline{q}$ u, d, s (red).*

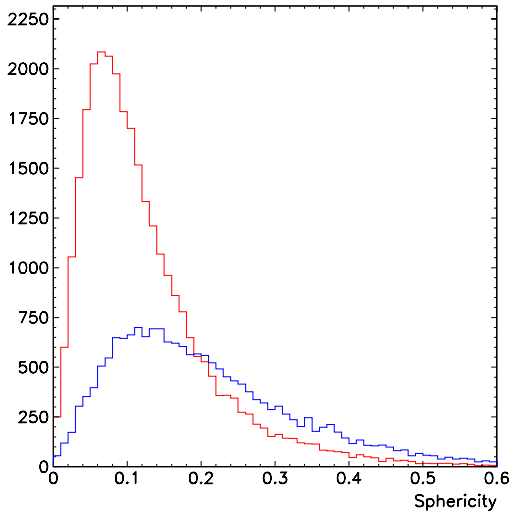

Figure 4-6. *Sphericity for the whole event, signal (blue), $q\overline{q}$ u, d, s (red).*

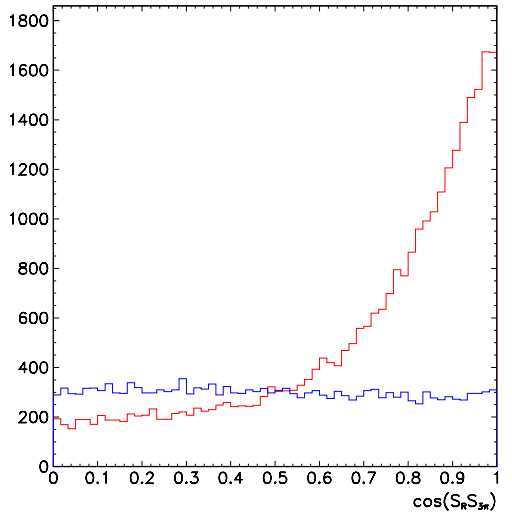

Figure 4-7. *Cosine of the angle between the sphericity axis of the rest of the event and the sphericity axis of the 3π system, signal (blue), $q\overline{q}$ u, d, s (red).*

sphericity tensor [42] by,

$$apl = \frac{3}{2}\lambda_3 \,. \tag{4.5}$$

So in the case of a totally planar event $\lambda_3 = 0$, and the aplanarity is zero. Whereas, for an isotropic event the three eigenvalues are of equal magnitude ($\frac{1}{3}$), and the aplanarity then takes a maximum value of $\frac{1}{2}$.

The planarity of a system is defined as the difference between the two smaller eigenvalues of the sphericity tensor,

$$pla = \lambda_2 - \lambda_3 \,. \tag{4.6}$$

The aplanarity and planarity for the rest of the event, apl_R and pla_R respectively, provide better signal/background discrimination than the aplanarity and planarity for the whole event.

- **Fox-Wolfram Moments ($\mathcal{H}_\ell$)**

  There is no natural axis in the final state of e^+e^- annihilation, and a common technique is to find an axis by minimising some observable. This is done in the case of the sphericity and thrust variables. This method is satisfactory for characterising continuum events with 2-jet structure, but can result in a poorly defined axis for events containing three or more jets [1].

  The Fox-Wolfram moments, $\mathcal{H}_\ell$, are independent of the axis used, and this has some advantages, including discriminating power between 2-jet and multi-jet events. As $\mathcal{H}_\ell$ are rotationally invariant, they are independent of the orientation of an event, so their values are insensitive to gaps in the angular acceptance of the detector.

  The Fox-Wolfram moments, $\mathcal{H}_\ell$, are defined [43] as,

$$H_l = \sum_{i,j} \frac{|\mathbf{p}_i|.|\mathbf{p}_j|}{E_{vis}^2} P_\ell \cos(\theta_{ij}) \,, \tag{4.7}$$

[1] the occurrence and clear identification of 3-jet events at BABAR is likely to be small, and has been disregarded.

where P_ℓ are the Legendre polynomials, $\mathbf{p}_{i,j}$ are the particle momenta, θ_{ij} is the opening angle between particles i and j, and E_{vis} is the total visible energy of the event.

Neglecting particle masses, if momentum is balanced for 2-jet events then , $H_0 = 1$, $H_1 = 0$, $\mathcal{H}_\ell \sim 1$ for ℓ even, and $\mathcal{H}_\ell \sim 0$ for ℓ odd. So for this application the ratio of Fox-Wolfram 2nd to 0th moments is taken as the discriminating variable. Energy-momentum conservation requires $H_0 = 1$, and $H_1 = 0$, if all particles in event are used (assuming calculation with respect to the $\Upsilon(4\mathrm{S})$ rest frame). For 2-jet events, since final quark momenta are collinear,
$\mathcal{H}_\ell = 1\,(even\,\ell)$,
$\mathcal{H}_\ell = 0\,(odd\,\ell)$.

- **Cones**

  The topological variable, Cones, is based on a method proposed by the CLEO Collaboration [44]. The space around a B^0 candidate is divided into a number of forward and backward cones centered on the B^0, and aligned with its thrust axis. The momentum flow between adjacent cones, *i.e.,* the scalar sum of the momenta of all particles pointing in the region, is calculated. At CLEO nine cones were used at 10° increments.

4.3.1 Considerations for Two- and Three-body Decays

Both two- and three-body decays exhibit well-defined kinematic behaviour which can be exploited for background suppression. The B decay axis for two-body decays is simply defined by the direction of either decay particle in the B rest frame. However, improved resolution, and less bias towards one particle, may be obtained by taking the difference between the momenta of both decay particles. In general, it is preferable to use

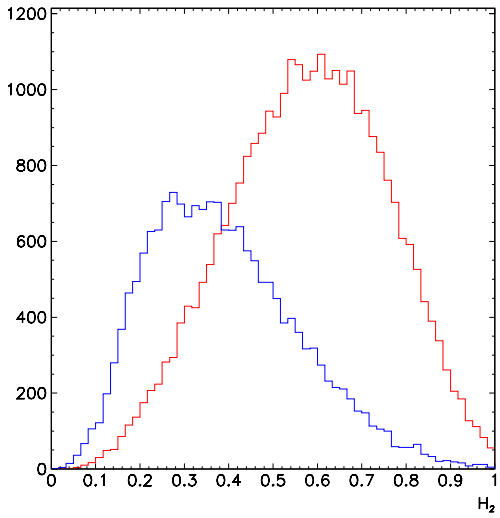

Figure 4-8. *Second Fox-Wolfram Moment for the whole event, signal (blue), $q\overline{q}$ u, d, s (red).*

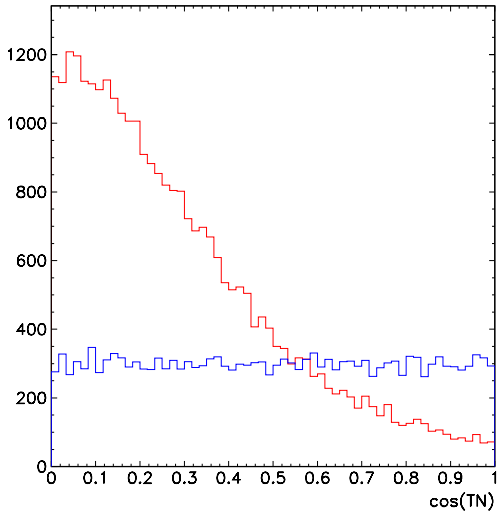

Figure 4-9. *Cosine of the angle between the normal to the B decay plane and the thrust axis for the rest of the event, signal (blue), $q\overline{q}$ u, d, s (red).*

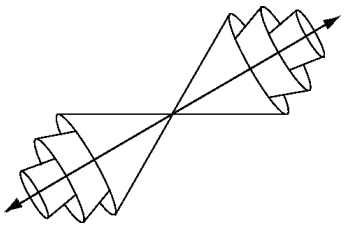

Figure 4-10. *Diagram showing the division of space around a B^0 candidate into cones for calculating momentum flow.*

charged tracks rather than neutral, but the final choice depends on the decay mode being considered.

Finding the best representation of the B decay axis for three-body decays is more involved. In the B rest frame the three final state particles lie in a plane. In the case of 3π, the decay is usually through the ρ resonance, so this pseudo-two-body nature allows the B decay axis to be defined as for two-body decays. However, for non-resonant 3π, the momenta of the three pions may be similar in magnitude, so that no overall direction can be identified. In this case, the orientation of the B decay in space is best characterised by the plane defined by the three pion momenta in the B rest frame. The normal to this plane then specifies a unique direction associated with the B decay. For $B^0 \to \pi^+\pi^-\pi^0$ the normal is defined by the cross product of the 3-momenta of the two charged πs in the B rest frame, since the charged tracks will always have better-defined directions than the π^0, (and the $\pi^+\pi^-$ are used to form the B vertex). In other three-body decays, where there are not exactly two charged decay products, then the two momenta which form the highest scalar product should be used.

4.4 Multivariate Analysis Techniques for Discrimination

The use of multivariate analysis techniques within High Energy Physics is widespread, as there are many applications where events need to be characterised as belonging to one of two classes for acceptance (*e.g.,* signal) or rejection (*e.g.,* background).

Within BABAR, a common interface to several multivariate methods is provided by the `Cornelius`[2] software package [46]. This offers ease of access to the various methods, and allows direct comparisons to be made between their performances, as the output of each method is a probability weighting that a given event comes from a given class. For two classes of events, the relative probability for an event to originate from class 1 is defined by,

$$p_1 = \frac{f_1 F_1(X)}{f_1 F_1(X) + f_2 F_2(X)}\,, \tag{4.8}$$

where the f_i are the fractions of events coming from class i ($f_1 + f_2 = 1$) and F_i the density distribution of the output variable, X, from a given multivariate method, normalized to unity.

The multivariate analysis methods which can be implemented via `Cornelius` are the Parameterised Approach (PA)[47], Fisher Method (FI)[48] and Neural Net (NN)[49]; these methods are briefly described below.

`Cornelius` was developed by the BABAR Tagging Group, and so its primary application has been to the discrimination between b and $\overline{b}$ flavours for the tagging B meson. However, the methods are completely general, and can be applied to the discrimination of any two classes where discriminating information is available. The work discussed here concerns the first application of these multivariate analysis techniques to the process of background discrimination using the full BABAR simulation (`BBsim`) in the BABAR object-oriented C++ software environment.

[2] Combined Optimal Reconstruction with Neural Network and Likelihood for Identification Usage

4.4.1 The Parameterised Approach (PA)

The Parameterised Approach distinguishes two classes (1 and 2) of events using relative likelihood. For n discriminating variables, the likelihood for an event to belong to class 1 is $g^1(x_1, \cdots x_n)$, and similarly for class 2. Then the ratio of these likelihoods provides a characteristic value for the event, with a range [0,1], X_{PA},

$$X_{PA} = \frac{g^1(x_1, \cdots x_n)}{g^1(x_1, \cdots x_n) + g^2(x_1, \cdots x_n)} \,. \tag{4.9}$$

The Parameterised Approach uses a simplification of this expression by assuming that the discriminating variables are uncorrelated, so that the likelihood expression for n variables reduces to the product of the likelihoods for the individual variables, *e.g.*, for class 1,

$$g^1(x_1, \cdots x_n) = \prod_{i=1}^{n} g_i^1(x_i) \,. \tag{4.10}$$

This method provides unbiased optimal discrimination, based on the variables provided, in the case where no correlation exists between the variables. However, where correlations do exist then some information is lost, and the discriminating power of the PA method is diluted.

4.4.2 The Fisher Method (FI)

The Fisher Method is a linear discriminant analysis, in which n variables are combined linearly in a single quantity, X_{FI}, to provide the largest separation between the two classes of events. The maximal separation is achieved by defining an axis in the n-dimensional space spanned by X_{FI} such that the distance between the means of each class ($\overline{\mathbf{x}}_1$, $\overline{\mathbf{x}}_2$), is a maximum. This axis of separation between the classes is therefore orthogonal to the line segment joining the class means. The discriminating quantity, X_{FI}, can then be determined for the set of discriminating variable values, $\mathbf{x}$, for an event,

$$X_{FI} = \frac{\sqrt{n_1 n_2}}{n} \left(\overline{\mathbf{x}}_1 - \overline{\mathbf{x}}_2\right)^T W^{-1} \mathbf{x} \tag{4.11}$$

where n_1, n_2 are the number of events in each sample, n is the total number of events, and W is the component of the total covariance matrix for the variables which represents the dispersion of the events within a class with respect to the class mean [50].

The quantity X_{FI} can be used to provide a probability that an event comes from a given class, or can be compared with a chosen threshold value in order to provide a cut criterion.

4.4.3 The Neural Net (NN)

Aa artificial neural net can provide a non-linear multivariate analysis, which offers potential improvements in discriminating performance over linear methods, but at the expense of increased complexity.

The neural net consists of a set of processing elements called neurons, which take as input a linear weighted combination of the discriminating variables, x. A threshold value, θ_j, is added to the input to provide a signal value Z for the neuron j,

$$Z = \sum_{k=1}^{n} \omega_{jk}\, x_k + \theta_j \,, \tag{4.12}$$

where ω_{jk} are the weightings.

The neuron can then be activated by the evaluation of a non-linear function at the value Z,

$$a(Z) = \frac{1}{2}(1 + \tanh Z). \tag{4.13}$$

The neurons are arranged in three layers which define the flow of data through the neural net. The first layer takes the set of discriminating variables as input, and the final layer gives the output of the neural net, X_{NN}. A hidden layer exists in between, containing n neurons. The output of the neural net is given by,

$$X_{NN} = a\,(\sum_{j=1}^{n} \omega_{1j}\, a\,(\sum_{k=1}^{n} \omega_{jk}\, x_k + \theta_j) + \theta_1)\,. \tag{4.14}$$

4.4.4 Separation as a Measure of Discriminating Power

The output of `Cornelius` is a probability that a given event belongs to a particular class, as shown in equation (4.8). This probability can either be used to associate an event to a class by using a fixed cut on its value – the fixed criterion approach, or it can be used to provide a weighting for the event – the probability approach.

A measure of the discriminating power of a set of distributions is provided by the quantity "separation" [51], which is a measurement of the purity of each of the classes being distinguished. If the distributions of a discriminating variable, x, are given by $F_1(x)$ and $F_2(x)$, for class 1 and class 2 events respectively[3], then the separation is defined as,

$$< s^2 >= \int (F_1(x) + F_2(x)) \left(\frac{(F_1(x) - F_2(x))}{(F_1(x) + F_2(x))} \right)^2 dx. \tag{4.15}$$

The variable x can be an individual discriminating variable, or the output from one of the multivariate methods (*i.e.*, X_{PA}, X_{FI}, X_{NN}), thus allowing the methods to be compared directly with each other.

In the probability approach, the separation is given by,

$$< s^2 >=< \left(\frac{p_2 - p_1}{p_2 + p_1} \right)^2 >=< (1 - 2p_1)^2 >=< (1 - 2p_2)^2 >, \tag{4.16}$$

where p_1 (p_2) is the relative probability for a given event to belong to class 1(2).

In the fixed criterion (cut) approach, the separation is a fixed number with the simplified expression,

$$< s^2 >= (1 - 2w)^2, \tag{4.17}$$

where w is the wrong association probability, *i.e.*, the probability that the criterion associates an event to the wrong class, which depends on the chosen cut value.

[3] the distributions must be correctly normalised and weighted by the *a priori* probability that an event comes from a given class.

4.5 A General Procedure for Background Suppression

A common procedure was developed to provide a set of tools for background suppression which can be applied to any CP analysis. The procedure makes use of the most general discriminating variables, and the structure of the common tools was designed to allow further variables to be added by the user which are specific to a given decay channel. The code was integrated within the BABAR software framework [52], and each stage in the procedure was controlled by a framework module, as described below :

Filtering

The filtering stage involves applying a set of preliminary cuts to every reconstructed continuum event from `BBsim` production. The aim is to reduce the sample by between one and two orders of magnitude, providing a condensed sample which contains the most dangerous $q\overline{q}$ background for the channel considered. A filter for a given CP-channel passes any event in which at least one B candidate is reconstructed. The cuts are loose enough to maintain signal efficiency as far as possible, and are typically made on the masses and momenta of the CP mode candidates. The signal events used in the background suppression procedure are also passed through the filter.

User Analysis Module

The analysis module takes as input the filtered samples for signal and $q\overline{q}$ background described above, using any additional cuts the user imposes, and produces a list of B candidates for each event. This list, together with details of the decay products for each reconstructed CP-mode, are then passed to the background suppression module.

Background Suppression

A tool was set up to provide an interface between the various functions used to calculate a set of background discriminating variables, and the subsequent multivariate analysis tools which can be used to optimise background suppression [53]. The design goal of this work was that it should supply a general list of variables which could apply to any channel, and

that it should be straightforward to add further variables which could be customised for particular channels. The output of the tool is an ntuple containing the distributions for each specified variable.

Cornelius Training

For the training stage, an HBOOK ntuple of the discriminating variables must be supplied to `Cornelius`, containing samples of both signal and background events. At least 3000 entries are needed in each sample to achieve acceptable performance from the training. For the neural network approach, samples of at least 5000 events each are required. The training procedure is discussed in more detail in the following section, where the results of training on different sets of discriminating variables are compared.

Cornelius Output

Having been trained on a $q\overline{q}$ sample, `Cornelius` can be instantiated in the user analysis in order to provide continuum suppression information. For each event, the chosen discriminating variables are calculated. These results effectively define a point in the multivariate space which has been characterised by the training process. The probability of an event belonging to the signal or background class is associated with each point, and this provides the user with a single selection criterion for suppressing the background. At this stage, either a cut can be applied on the probability to select a subset of events, or all events can be kept, with the probability used to weight each event at the subsequent CP fitting stage.

4.6 Results of Multivariate Analysis Training

The PA method was applied to a set of discriminating variables, as listed in table 4-1. The initial task of `Cornelius` was to rank the variables according to their individual discriminating power, determined by the individual separations, with no consideration for correlations with other variables. The results of this process are shown in table 4-1,

where it can be seen that the best individual discriminating variable is the momentum of the B^0_{CP} in the $\Upsilon(4S)$ rest frame. The invariant mass of the recontructed B^0_{CP} candidate is another a powerful discriminating variable, and several event shape variables are also ranked highly.

Table 4-1. *Separation $< s^2 >$ for individual discriminating variables (the variable definitions can be found in the text).*

Variable	$< s^2 >$	$< s^2 >$ error
$p*_B$	3.46 $\times 10^{-1}$	7.70 $\times 10^{-3}$
M_B	3.42 $\times 10^{-1}$	8.01 $\times 10^{-3}$
$\cos(S\pi)$	3.35 $\times 10^{-1}$	8.00 $\times 10^{-3}$
$\cos(SB)$	3.33 $\times 10^{-1}$	8.02 $\times 10^{-3}$
$\cos(T\pi)$	3.18 $\times 10^{-1}$	7.80 $\times 10^{-3}$
$\cos(TB)$	3.17 $\times 10^{-1}$	7.85 $\times 10^{-3}$
H_2	2.77 $\times 10^{-1}$	7.26 $\times 10^{-3}$
T	2.68 $\times 10^{-1}$	7.10 $\times 10^{-3}$
S	1.89 $\times 10^{-1}$	6.38 $\times 10^{-3}$
$\cos(SS_{3\pi})$	1.66 $\times 10^{-1}$	6.29 $\times 10^{-3}$
$\cos(SN)$	1.60 $\times 10^{-1}$	6.06 $\times 10^{-3}$
$\cos(TN)$	1.45 $\times 10^{-1}$	5.78 $\times 10^{-3}$
$\sigma_{\pi^-K^-}$	5.97 $\times 10^{-2}$	2.39 $\times 10^{-3}$
$\sigma_{\pi^+K^+}$	5.30 $\times 10^{-2}$	2.40 $\times 10^{-3}$
H_{2R}	4.15 $\times 10^{-2}$	3.32 $\times 10^{-3}$
T_R	3.87 $\times 10^{-2}$	3.19 $\times 10^{-3}$
S_R	3.74 $\times 10^{-2}$	3.12 $\times 10^{-3}$
z_T	3.14 $\times 10^{-2}$	2.88 $\times 10^{-3}$
pla_R	2.82 $\times 10^{-2}$	2.71 $\times 10^{-3}$
apl_R	2.47 $\times 10^{-2}$	2.36 $\times 10^{-3}$
x_T	1.60 $\times 10^{-2}$	2.15 $\times 10^{-3}$
y_T	1.23 $\times 10^{-2}$	1.89 $\times 10^{-3}$
$\cos(BS_R)$	1.01 $\times 10^{-2}$	1.71 $\times 10^{-3}$
$\cos(B\pi)$	6.66 $\times 10^{-3}$	1.40 $\times 10^{-3}$
p_tB_R	2.43 $\times 10^{-3}$	6.01 $\times 10^{-4}$
$\cos(\rho\pi)$	1.30 $\times 10^{-4}$	5.60 $\times 10^{-5}$

An iterative process was then performed in which the variables were used in different combinations to calculate values of overall separation. The process began by taking the variable with the highest separation and combining it with each of the other variables

in turn, until the pair with the highest combined separation was found. This pair was then combined with each of the remaining variables to find the triplet with the highest separation, and so on. This algorithm provides a set of variables which is close to optimal. In order to guarantee that the most optimal set of variables was produced it would be necessary to employ a slower and more complex algorithm, in which the separation was calculated for every possible combination of variables.

The results of the combined separations are shown in table 4-2. Clearly, by using certain combinations of variables greater values of separation are possible than with individual variables. In the ranking of combinations, though, only one of the event shape variables has been retained close to the top of the list. This is due to the close relationships which exist between many of the event shape variables, resulting in large correlations.

The information provided by the individual and combined separations in this ranking procedure allows judgements to be made about the best set of variables to use for discrimination.

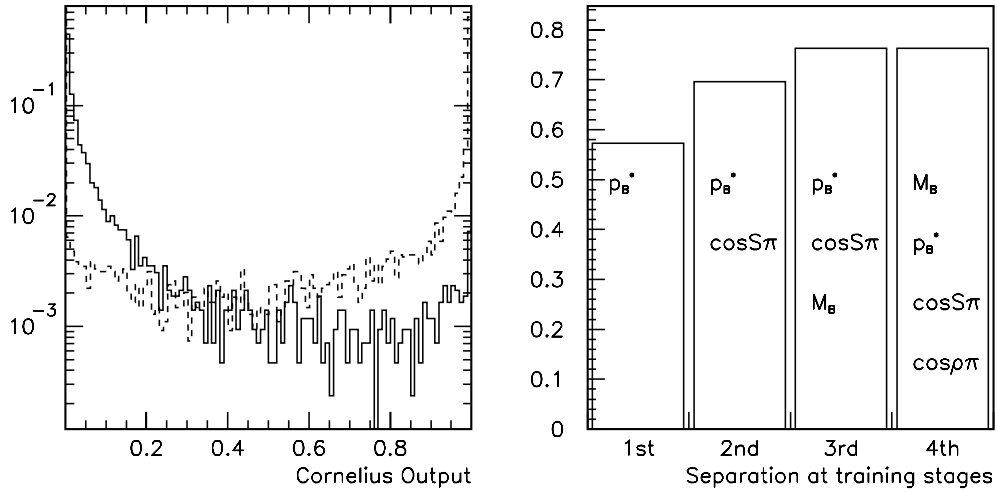

Figure 4-11. *Results of Cornelius training using the PA method on four discriminating variables: The left plot shows the distributions of signal events (solid line) and $q\overline{q}$ background events (dotted line) for the output of the training process, i.e., in this case the probability that events are background. The right plot shows the value of separation achieved during the training process for four sets of discriminating variables.*

Table 4-2. *Separation $< s^2 >$ for combinations of discriminating variables - each value of separation in the table refers to the accumulation of the set of variables in the rows above, (the variable definitions can be found in the text).*

Variable	$< s^2 >$	$< s^2 >$ error
$p*_B$	3.46 $\times 10^{-1}$	7.70 $\times 10^{-3}$
$\cos(SB)$	5.44 $\times 10^{-1}$	8.46 $\times 10^{-3}$
M_B	6.52 $\times 10^{-1}$	8.55 $\times 10^{-3}$
H_2	6.70 $\times 10^{-1}$	8.22 $\times 10^{-3}$
$\sigma_{\pi^- K^-}$	6.85 $\times 10^{-1}$	8.14 $\times 10^{-3}$
$\sigma_{\pi^+ K^+}$	6.97 $\times 10^{-1}$	8.05 $\times 10^{-3}$
x_T	7.02 $\times 10^{-1}$	8.05 $\times 10^{-3}$
y_T	7.03 $\times 10^{-1}$	8.04 $\times 10^{-3}$
z_T	7.07 $\times 10^{-1}$	8.00 $\times 10^{-3}$
$\cos(BS_R)$	7.13 $\times 10^{-1}$	7.84 $\times 10^{-3}$
$\cos(\rho\pi)$	7.13 $\times 10^{-1}$	7.85 $\times 10^{-3}$
$p_t B_R$	7.12 $\times 10^{-1}$	7.84 $\times 10^{-3}$
$\cos(B\pi)$	7.12 $\times 10^{-1}$	7.81 $\times 10^{-3}$
pla_R	7.08 $\times 10^{-1}$	7.78 $\times 10^{-3}$
apl_R	7.00 $\times 10^{-1}$	7.74 $\times 10^{-3}$
$\cos(TN)$	6.88 $\times 10^{-1}$	7.26 $\times 10^{-3}$
S_R	6.84 $\times 10^{-1}$	7.27 $\times 10^{-3}$
T_R	6.73 $\times 10^{-1}$	7.20 $\times 10^{-3}$
$\cos(SS_{3\pi})$	6.63 $\times 10^{-1}$	7.01 $\times 10^{-3}$
H_{2R}	6.54 $\times 10^{-1}$	7.02 $\times 10^{-3}$
$\cos(SN)$	6.37 $\times 10^{-1}$	6.86 $\times 10^{-3}$
S	6.16 $\times 10^{-1}$	6.16 $\times 10^{-3}$
$\cos(TB)$	5.89 $\times 10^{-1}$	5.89 $\times 10^{-3}$
T	5.57 $\times 10^{-1}$	6.81 $\times 10^{-3}$
$\cos(S\pi)$	5.30 $\times 10^{-1}$	6.75 $\times 10^{-3}$
$\cos(T\pi)$	5.11 $\times 10^{-1}$	6.77 $\times 10^{-3}$

A simple example of the output of training `Cornelius`, on fully reconstucted events, is shown in Fig. 4-11, using the PA method and four discriminating variables, $p*_B$, M_B, $\cos(S\pi)$ and $\cos(\rho\pi)$. The probability distributions for signal and background events can be used to calculate the final value of separation, using equation 4.16. The final separation was found to be 75.2%. As indicated in section4.4.4, this is a measure of the expected purity of the signal which can be achieved when using `Cornelius` at the analysis level, trained on this set of discriminating variables.

Fig. 4-11 also shows the separation at each stage of the training process. The PA method is most effective when the variables are uncorrelated, and it can be seen in this example that adding a fourth variable provides no additional discriminating power. This limitation of the PA method is illustrated more clearly in Fig. 4-12, where the separation peaks for a combination of 13 variables, and then falls as further variables are added.

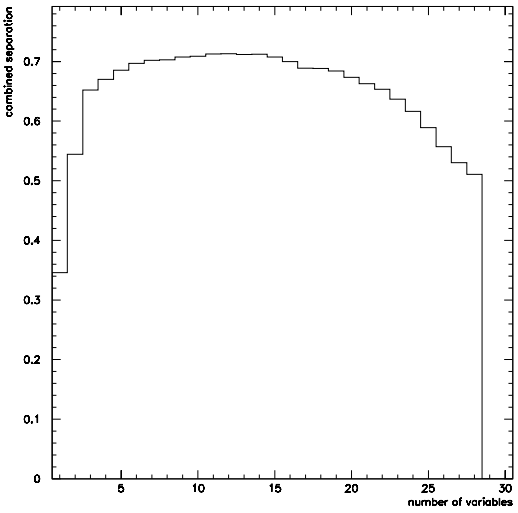

Figure 4-12. *Combined separation for the variables shown in table 4-2 using the PA method.*

4.7 Factors Affecting Performance

The effectiveness of the procedure which has been described is dependent on both the discriminating power of the individual variables, and on the correlations between them. Some examples of the correlations between some of the variables studies here are shown in Fig.4-13.

Selecting the final set of discriminating variables to use for background suppression must also take into account the type of multivariate analysis method employed, as correlations between the variables are handled differently. Care must be taken when selecting the

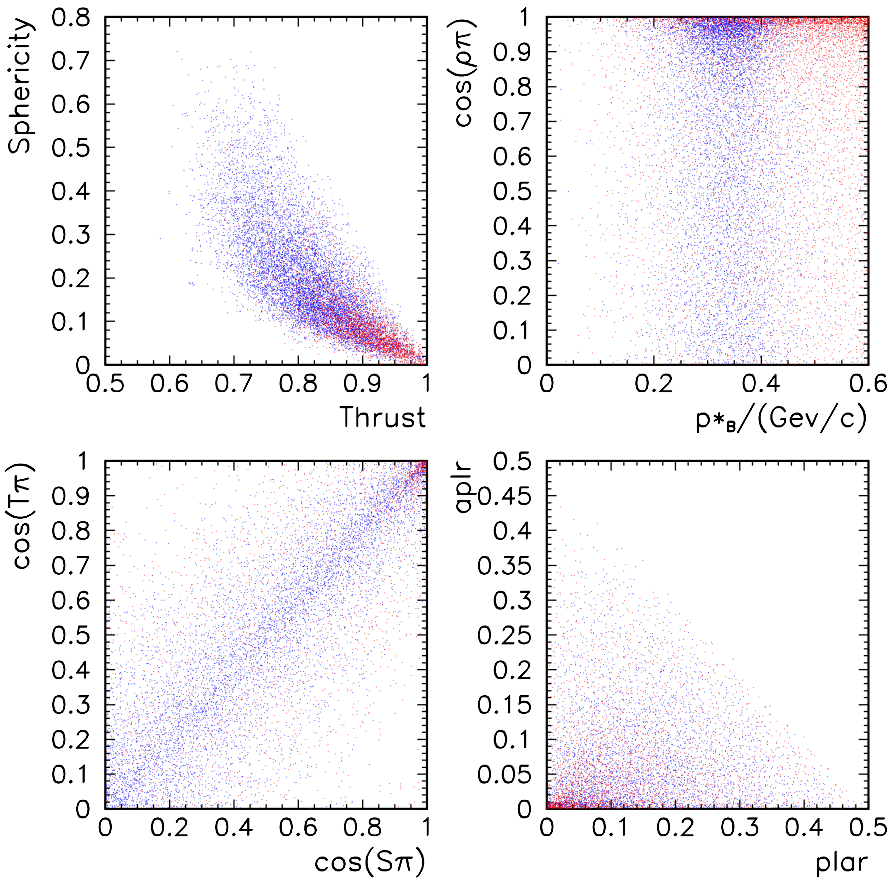

Figure 4-13. *Correlations between some Discriminating Variables, signal (blue), u, d, s background (red).*

variables for use with the PA method to ensure that large correlations do not exist. A neural network method, however, can handle correlations effectively, so in general it is possible to use more variables in the training process.

While it is tempting to add as many potential discriminating variables as possible, especially in the case of the neural network method, it is advisable to be conservative since, for every method, the overall systematic error is necessarily larger for more variables.

In the case of the Fisher method, it is important to avoid the inclusion of any variable which is a linear combination of others which are used, since the matrix inversion will not be possible (*e.g.,* sphericity, aplanarity and planarity).

Another approach, which has not been considered here, is the use of a Genetic Algorithm [54]. This provides an automated method for optimising sets of simple cuts. It therefore preserves the main advantage of simple cuts, which is the relative simplicity of interpreting systematic effects in the analysis, while offering the benefits of automation and optimisation.

4.7.1 The Fitting Algorithm

In addition to choosing the best inputs to the multivariate analysis, it is important to consider the internal factors which may affect the overall performance of this method. The performance of `Cornelius` depends strongly on the perceived shapes of distributions for the classes considered, and this requires a high quality and robust fitting procedure. The original fitting method [55], which has been used here, was not optimally designed for low statistics distributions, as would be found in real data. The implementation of a fitter with a more appropriate smoothing algorithm should improve overall performance.

4.8 Summary

The issue of backgrounds for CP studies with BABAR has been discussed, and the relative importance of the various types of background has been identified. A number of variables which are useful for background discrimination have been introduced. It was shown that many of the topological variables effectively carry the same information, and so are highly correlated. The essential topological information to extract is that a strong correlation exists between the directions of the decay axes of the putative B^0_{CP} and B^0_{tag} candidates in

continuum events, while essentially none exists for signal events. The issue then becomes one of defining these axes in the best possible way.

Several multivariate analysis techniques were described, and examples of their performance for background suppression were given. It is expected that such techniques will play an important role in providing CP analyses with optimal background suppression. However, both the issue of unknown levels of machine backgrounds, and the need for training the multivariate methods on realistic data samples, mean that the full implementation and study of the effectiveness of these methods must wait until real data is available.

5

Data Analysis for $B^0 \to \pi^+\pi^-\pi^0$

5.1 Introduction

An analysis of the channel $B^0 \to \pi^+\pi^-\pi^0$ has been carried out using Monte Carlo events which were produced using the full BABAR reconstruction software[56]. The $B^0 \to \pi^+\pi^-\pi^0$ mode provides a possible source for the measurement of the CP angle α [57]. However, the full study of this channel with data will be a challenging procedure, due to both the substantial level of background expected, and to the theoretical uncertainties which complicate the analysis. It is therefore necessary to ensure that the event selection process is designed to provide a high quality sample of data for the CP extraction stage, having a low level of background contamination. This chapter describes the details of the procedure used to select events. Since the ultimate requirement of this process is to obtain a set of data which will provide good time distribution and b flavour information, the topics of tagging and vertexing for the B candidates form an integral part of the study; in particular, the vertexing procedure has been studied in detail, and the results are reported here.

5.2 Preliminary Cuts for Pre-selection of Events

The small expected branching ratio (5.5×10^{-5}, [13]) of the $B^0 \to \pi^+\pi^-\pi^0$ channel, and the presence of three particles in the decay, indicate that this channel will suffer

from a very large background compared with the small number of expected signal events. There are several sources of background which must be considered, and these have been categorised in chapter 4. The combinatorial background arises mainly from the presence of the π^0 in the decay, and from the wide range of kinematic configurations available in the final state. The physics background comes from B decays to similar channels, such as $B^0 \rightarrow K^{\pm}\pi^{\mp}\pi^0$ with $\pi/\ K$ mis-identification, or from kinematically similar decays, possibly with lost particles, such as 2π and 4π modes. While these backgrounds are significant, being of the same order as the signal, the continuum background is the dominant by several orders of magnitude.

In order to handle the background suppression effectively, the event selection was carried out in two stages. In the first stage, pre-selection, a set of preliminary cuts was applied for the purpose of reducing the background while maintaining high signal efficiency. The variables used for these cuts were the mass of the π^0 from the B candidate decay, and the mass and momentum (in the $\Upsilon(4\mathrm{S})$ rest frame) of the B candidate. No cut was made on ρ mass so that the full phase space of the three pion mode was preserved. The B candidates from the resulting set of events which passed this initial "filtering" process were then reconstructed from scratch with more stringent constraints on the π candidates : a minimum momentum was required for all three pions, and the π^0 selection algorithms were fully implemented.

In the second stage of background rejection (discussed in the next section), a further set of cuts was applied, in order to substantially improve the rejection of the more persistent background, which had survived the first stage cuts, but with some loss in signal efficiency. For this purpose, a number of the discriminating variables described in Chapter 4 were used to suppress the background.

The signal events referred to here comprised $B^0 \rightarrow \pi^+\pi^-\pi^0$, with $\overline{B}^0 \rightarrow X$, and included mixing. The continuum background considered was separated into light quark (u, d, s), and charm events, all of these being simulated at the $\Upsilon(4\mathrm{S})$ resonance. The total number

of events processed is shown in Table5-1. From this sample, 5000 events passing pre-selection cuts were required for each of signal and $q\overline{q}$ to provide a training sample for the background fighting methods.

Table 5-1. *Statistics for the Monte Carlo events generated using the* `BBsim` *[56] simulation*

Event type	Total number of events generated	equivalent luminosity (fb^{-1})
$B^0 \to \pi^+\pi^-\pi^0, \overline{B}^0 \to X$	52,000	886
$q\overline{q}\,(u,d,s)$	2.988 $\times 10^6$	1.29
$c\overline{c}$	1.790 $\times 10^6$	1.24

5.2.1 The cut on π^0 mass

The $B^0 \to \pi^+\pi^-\pi^0$ mode includes $\pi^0\,s$ across a wide energy range, up to $\sim 3\,\mathrm{GeV}$. The energy spectrum is divided into two distinct regions due to the polarisation of the intermediate ρ in this mode (see Fig.5-5). While $\pi^0\,s$ with energy less than $\sim 2\,\mathrm{GeV}$ are usually resolvable as two separate photons, which appear as distinguishable bumps[1] in the calorimeter, above this energy the photons become merged, so that individual bumps cannot be separated. In order to handle the reconstruction of $\pi^0\,s$ from both resolved and merged photons two distinct algorithms were used. In the first method, $\pi^0\,s$ from resolved photons were formed by combining all pairs of photon candidates, which appear as bumps in the calorimeter. A cut was made on the calculated invariant mass of these $\pi^0\,s$ of $0.10 < M_{\gamma\gamma} < 0.17\ \mathrm{GeV/c^2}$ (Fig.5-2). In the second method, any clusters above a threshold energy of $700\,\mathrm{MeV}$ were considered to be merged π^0 candidates, and were assigned the nominal π^0 mass, *i.e.*, the π^0 energy was recalculated using the nominal mass for the same 3-momentum. Both methods also rely on the electromagnetic calorimeter track-matching algorithm [59] to determine which electromagnetic calorimeter energy deposits

[1] the term "bump" refers to a local energy maximum in the calorimeter which satisfies a given set of energy cuts, [58]

arise from neutral particles. The sets of π^0 candidates produced by each method were then checked, using the reconstructed decay tree, to ensure that there was no overlap of identical (duplicated) candidates, especially in the region where a pair of bumps was partially merged but the bump centroids were resolved; legitimate combinatorial backgound was kept, however. The efficiency performances of the two algorithms were found to complement each other over the full momentum range, as shown in Fig.5-1.

The mass distributions of the resolved π^0 candidates for $\pi^+\pi^-\pi^0$ signal events before other pre-selection cuts are shown in Fig.5-2. The signal π^0 mass distribution has a resolution of about 10 $\mathrm{MeV/c^2}$(fitting with a single Gaussian function, and ignoring tails).

5.2.2 The cuts on B^0 mass and momentum

The B^0 candidates were reconstructed by forming all combinations of $\pi^+\pi^-\pi^0$ candidates which gave an invariant mass compatible with the B^0 mass, within the range $5.00 < M_B < 5.60\,\mathrm{GeV/c^2}$. The B^0 is produced close to rest in the $\Upsilon(4\mathrm{S})$ rest frame, so a highly background-suppressing cut can be made on the B^0 momentum, without affecting the signal. The B candidate momentum in the $\Upsilon(4\mathrm{S})$ rest frame was taken to be in the range $0.0 < M_B < 0.6$ $\mathrm{GeV/c^2}$. The distributions of mass and momentum for the B^0 candidates, both for the signal and the combinatorial background, are shown in Fig.5-3. The resolution on the B^0 mass peak for the signal is 40 $\mathrm{MeV/c^2}$.

The values of all the filter cuts, and the resulting signal efficiencies for each cut, are summarized in Table 5-2. These efficiencies do not include the effects of detector acceptance and reconstruction efficiency, which combined with the filter cuts give an overall efficiency for signal events of $\sim 60 - -70\%$.

The reconstructed B^0 distributions emphasise the presence of the combinatorial background, which is still high after the initial filtering process. Moreover, the combinatorial background is expected to be significantly higher with data which includes machine

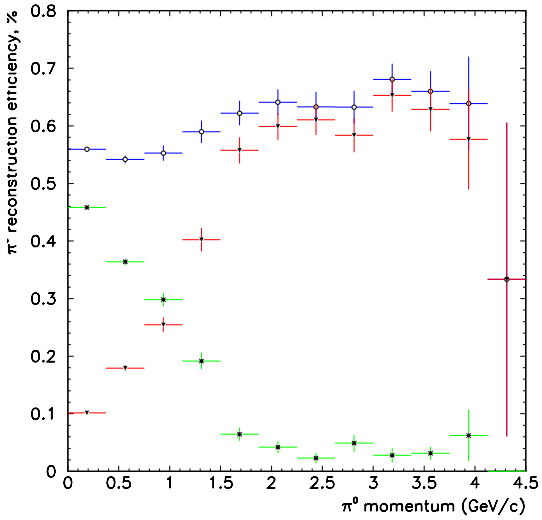

Figure 5-1. *Variation of reconstruction efficiency for π^0 candidates from signal events, as a function of momentum, for resolved π^0 s (green), merged π^0 s (red), and all π^0 s (blue).*

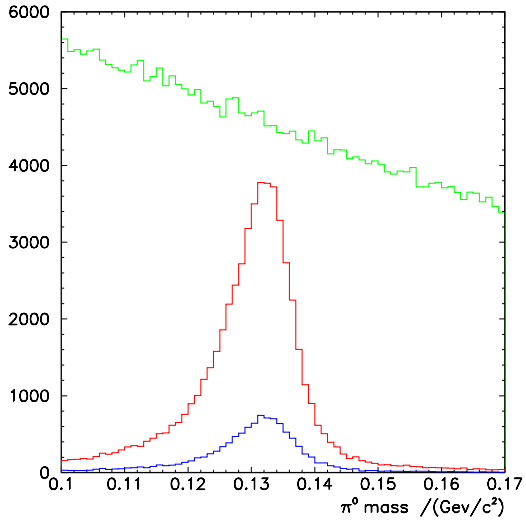

Figure 5-2. *Invariant mass distributions for π^0 candidates from signal events which are reconstructed from resolved photon candidates, following the pre-selection cuts : signal π^0 s (blue), all real π^0 s (red), false combinations (green).*

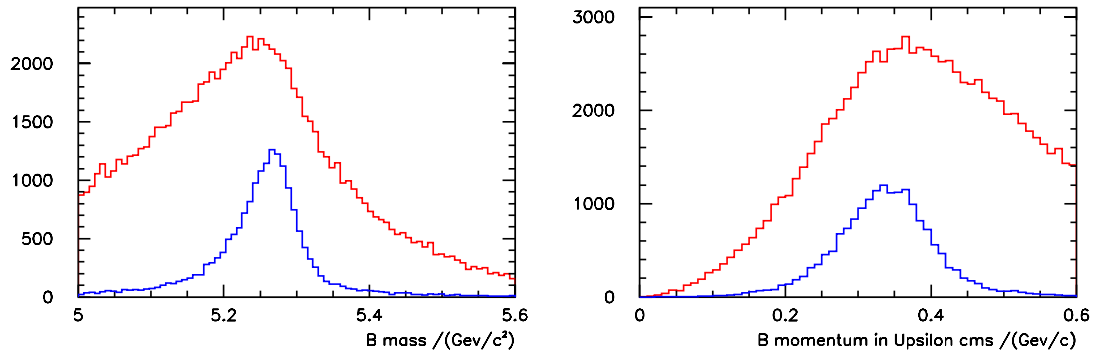

Figure 5-3. *B^0 mass, and momentum in the $\Upsilon(4S)$ rest frame for signal events (blue), including combinatorial background (red) after the cuts for pre-selection.*

Table 5-2. *Signal efficiencies for initial filter cuts*

filter cut variable	Allowed Range	Efficiency
$M_{\gamma\gamma}$	$0.10 < M_{\gamma\gamma} < 0.17$ GeV/c^2	0.93
M_B	$5.00 < M_B < 5.60$ GeV/c^2	0.93
$p_B^\star$	$0.00 < p_B^\star < 0.6$ GeV/c	0.99

background, since this will provide an additional source of many low energy photons. In order to reduce the combinatorial background further, the energy of each pion was required to be greater than 30 MeV. This is, in any case, an appropriate cut to make since it is close to the limit of the detection capabilities of BABAR.

The efficiencies for signal and background events at the completion of the pre-selection stage are summarised in Table 5-3.

In order to see how the above cuts affect the Dalitz Plot, Fig.5-4 illustrates how the efficiency for the signal varies as a function of the Dalitz Plot variables. Each plot is a projection of one of the three ρ bands of the Dalitz Plot. The efficiency is generally flat, but it decreases near the ends of the variable ranges which correspond to the production of a soft pion.

Table 5-3. *Selection efficiencies after filtering and pre-selection for signal and continuum events : the efficiency refers to the fraction of events with at least one B candidate which has passed the pre-selection cuts ("all" refers to signal and combinatorial background)*

Event type	Efficiency after filtering	Efficiency after pre-selection	Equivalent number of events at 30 fb^{-1}
$B^0 \to \pi^+\pi^-\pi^0, \overline{B}^0 \to X$ (all)	0.72	0.64	1133
$B^0 \to \pi^+\pi^-\pi^0, \overline{B}^0 \to X$ (signal)	0.50	0.47	827
$q\overline{q}(u,d,s)$	0.018	0.012	854000
$q\overline{q}(c\overline{c})$	0.014	0.00093	402690

5.2.3 The Effect of π^0 Reconstruction on Pre-Selection Efficiency

The method for reconstructing B^0s which has been carried out for the pre-selection is dependent on the efficient reconstruction and identification of π^0 s. The BABAR calorimeter has been designed to provide high quality π^0 identification. Nevertheless, π^0 s from the $B^0 \to \pi^+\pi^-\pi^0$ channel exhibit a broad range of momenta and energy, (see Fig.5-5), which suggests that B^0 reconstruction may be poor in some regions of the $\pi^+\pi^-\pi^0$ phase space. Additionally, the expected multiplicity of calorimeter clusters from machine backgrounds is likely to further suppress the overall π^0 reconstruction efficiency. In order to assess the potential impact of these issues on an analysis of the $B^0 \to \pi^+\pi^-\pi^0$ channel, the possibility of reconstructing B candidates without the presence of π^0 information was investigated.

It is known that Bs produced at the $\Upsilon(4\text{S})$ resonance will be almost at rest in the $\Upsilon(4\text{S})$ rest frame ($\beta_B \simeq 0.064$). This information can be exploited in partially reconstructing the B^0_{CP} candidate, *i.e.,* without the need to reconstruct π^0 s, and using only the charged πs in the event. The charged πs are expected to be well-determined, and overall tracking efficiency is good to the level of $p_t \simeq 50\,\text{MeV/c}$, which is comparable to the detection energy threshold for neutral pions. But whereas the tracking is close to 100% efficient within

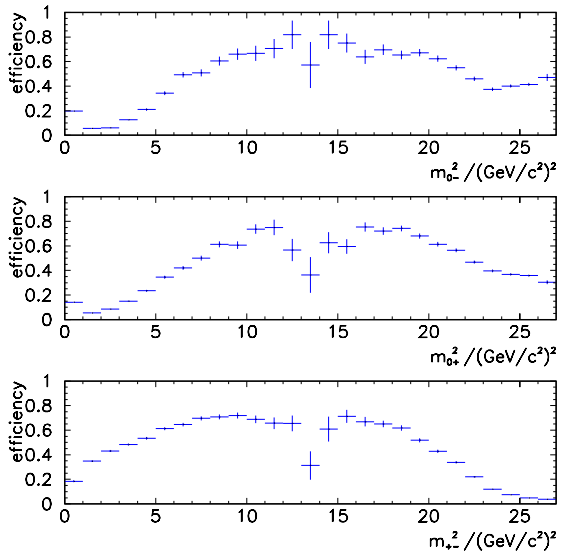

Figure 5-4. *Efficiency for signal after pre-selection cuts as a function of position along the three ρ bands of the Dalitz Plot.*

acceptance, the π^0 reconstruction efficiency varies from about 70% at high momentum, to less than 60% at low momentum. Pairs of oppositely charged particles were combined, with the requirement of a two-track vertex χ^2 less than three, in order to eliminate any poorly reconstructed tracks and reduce combinatoric background within events.

The calculated total energy of the pair in the B^0 rest frame is ,

$$E_{calc} = \frac{(m_B^2 - m_{\pi^0}^2 + m_{\pi\pi}^2)}{2m_B}, \tag{5.1}$$

where $m_{\pi\pi}$ is the invariant mass of the $\pi^+\pi^-$ pair, and m_{π^0} and m_B are the nominal π^0 and B^0 masses respectively. This was compared with the measured energy of the pair in the $\Upsilon(4S)$ rest frame, and the difference, $E_{meas} - E_{calc}$, was plotted as a function of the measured combined $\pi^+\pi^-$ mass, $m_{\pi\pi}$, as shown in Fig.5-6.

The triangular shape of the signal distribution is due to the range of the B^0 momentum in the $\Upsilon(4S)$ rest frame. The effect of the ρ polarisation can clearly be seen by the depletion of signal events in the mid-range of $m_{\pi\pi}^2$. A cut was defined around a triangular region,

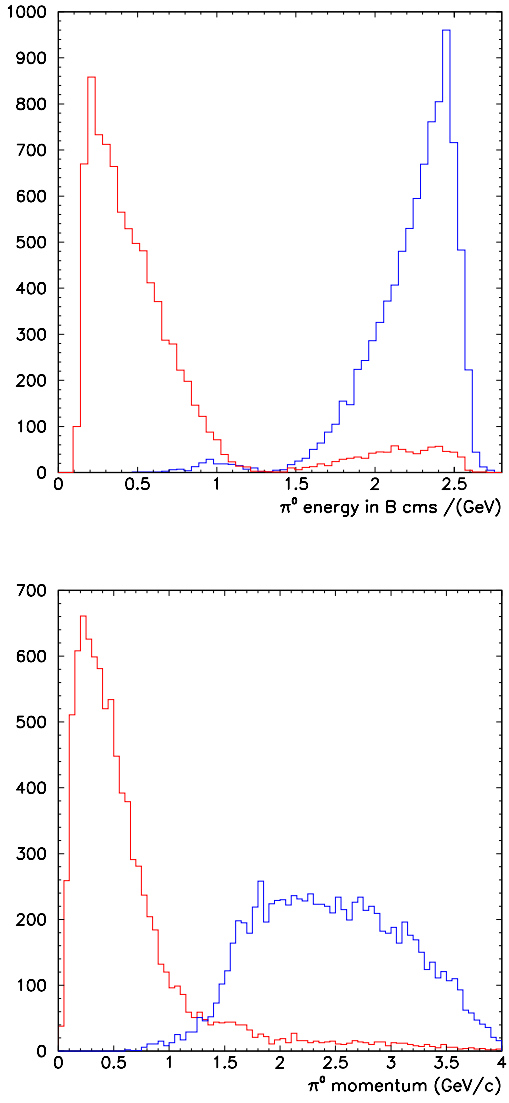

Figure 5-5. *Energy (in B rest frame) and momentum (in lab. rest frame) distributions for merged π^0 s (blue) and resolved π^0 s (red).*

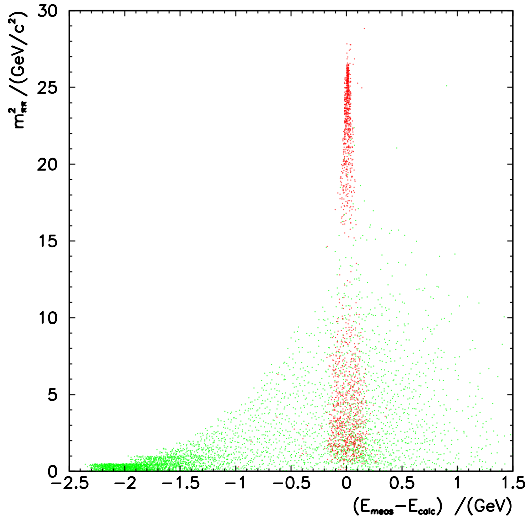

Figure 5-6. *Distributions of the difference between measured and calculated energy for $\pi^+\pi^-$ combinations as a function of $\pi^+\pi^-$ invariant mass squared, for $\pi^+\pi^-$ pairs from signal (red) and combinatorial background (green). The distribution for $q\bar{q}$ events is similar to that for combinatorial background.*

centered on $E_{meas} = E_{calc}$ and linear in $m^2_{\pi\pi}$, which was highly efficient for the signal,

$$m^2_{\pi\pi} = \pm 150(E_{meas} - E_{calc}) + 33 \ , \ m^2_{\pi\pi} > 0.7 \, . \tag{5.2}$$

The efficiency after this cut was 74% for $\pi^+\pi^-\pi^0$ events including acceptance effects, while the combinatorial background for $\pi^+\pi^-$ combinations was suppressed at a level of 8%. Since the tracking efficiency and acceptance are largely independent of momentum, this method did not favour any particular region of the Dalitz Plot.

It is feasible to carry out the remainder of the analysis with such a sample of partially-reconstructed B^0_{CP} candidates. The essential vertex information is available[2], and the most powerful discriminating variables for background suppression involve only the properties of charged tracks[3]. It is thus possible to undertake the full event selection with this method. However, the reconstructed π^0 is ultimately needed in order to determine the

[2] the effect of including the π^0 information in a kinematic fit to the B^0_{CP} is discussed in section 5.6.5

[3] the subject of background discrimination is covered in detail in Chapter 4

position of an event in the Dalitz Plot, but this requirement may be postponed until after the event selection.

5.3 Background Rejection

Following the pre-selection stage, the continuum background still dominates the signal by a factor ~ 750 (see Table 5-3). The second stage of event selection requires the use of discriminating variables which cut both signal and background. The details of the discriminating variables which have been considered were discussed in Chapter 4. Nine discriminating variables were used to separate signal and continuum; these included the original pre-selection variables with more stringent cuts applied. A further cut has also been made on the minimum momentum required of any photon which is used in reconstructing a resolved π^0 candidate. This corresponds closely to the limit of detection capability for the calorimeter.

Essentially all of the topological information for an event could be exploited by using one shape variable. Slightly better performance was obtained by using the two variables, $\cos(axis_{TR}\pi)$ and $\cos(axis_{SR}\pi)$, (defined in section 4.3), with the same cut, and a further small improvement was obtained with a cut on the Fox-Wolfram second moment. Particle identification cuts were also added for the two charged pion candidates from the B^0_{CP} decay. For each event, all three ρ candidates were reconstructed by forming all pairs of the decay pions. A loose cut was then made on the ρ mass, such that an event passed if any of the three ρ candidates passed the cut, so that three broad bands were selected in the Dalitz Plot, maintaining the regions with high signal.

The final set of background suppression cuts and the resulting selection efficiencies are summarised in Table 5-4, and the distributions of these variables are shown at the end of this section, Fig.5-7, Fig.5-8. The tagging efficiency has been included at this stage for completeness, as it provides some further natural discrimination between signal and back-

ground. The total efficiencies for the combined pre-selection and background suppression stages are 0.12 for 3π, 0.39×10^{-4} for u, d, s, and 0.30×10^{-4} for $c\bar{c}$ events. For one year of data-taking at nominal luminosity this corresponds to about 260 3π events, 2700 u, d, s events, and 1300 $c\bar{c}$ events. Clearly, the level of background must be further reduced if a reasonable analysis is to be performed, hence the need for techniques to fully optimise the cuts. However, this simple study serves to illustrate that levels of background rejection of the order of 10^{-4} can be achieved with relative ease. The final tuning and optimisation of the background suppression methods can only be validated once real data is available.

Table 5-4. *Background suppression cuts and efficiencies for 3π, u, d, s, and $c\bar{c}$ events*

Cut	3π	$q\bar{q}$ u, d, s	$c\bar{c}$
$0.17 < p{*}_B < 0.46\,\mathrm{GeV/c}$	0.94	0.48	0.46
$5.10 < M_B < 5.36\,\mathrm{GeV/c^2}$	0.93	0.52	0.52
$0.115 < M_{\pi^0} < 0.145\,\mathrm{GeV/c^2}$	0.95	0.85	0.87
$0.35 < M_\rho < 1.20\,\mathrm{GeV/c^2}$	0.95	0.80	0.79
$\cos(axis_{TR}\pi), \cos(axis_{SR}\pi) < 0.6$	0.55	0.10	0.09
$\sigma_{\pi^+K^+} = 0, \sigma_{\pi^-K^-} = 0$	0.99	0.79	0.62
$H_2 < 0.8$	1.00	0.96	0.92
$p_\gamma > 30\,\mathrm{MeV/c}$	0.97	0.91	0.98
tagging efficiency	0.56	0.28	0.29
total efficiency	0.24	0.33×10^{-2}	0.33×10^{-2}

The full Dalitz Plots for signal and $q\bar{q}$ events, before and after the background suppression cuts, are shown in Fig 5-9. It is interesting to note that the $q\bar{q}$ distribution before the background suppression cuts is concentrated near the edges of the Dalitz Plot. This is partly an effect of the pre-selection cuts, which have already been applied at this stage, however, it is mainly a result of the light quark continuum events having a strong pseudo-2-body characteristic, due to their 2-jet structure. This mimics the pseudo-2-body decay

of the 3π decay via the ρ resonance, and therefore enhances the level of u, d, s background which contaminates the signal.

Another discriminating variable which has not been considered in this analysis is the vertex of the B^0_{CP} candidate. This has been deliberately excluded from the cuts in order to preserve the full time distribution for both signal and background. However, studies have shown [60] that vertex cuts in the 100-200 μm range have only a small effect on CP resolution. Therefore, there is potential for considering such cuts to further reduce background. Cuts on the vertex position would be most effective at suppressing light quark continuum, with a reduced effect for $c\bar{c}$ events.

5.3.1 Background from Physics Channels

The $B^0 \to \pi^+\pi^-\pi^0$ mode can also suffer backgrounds from other B decay processes to final states containing several pions, especially $\pi^0 s$. The 4π modes may present a significant background, especially where one of the πs is lost. Also, charged two body decays can provide some background where low energy π^0 candidates in the event can combine with the two signal charged pions to form a B^0 invariant mass (these events will populate the lower left corner of the Dalitz Plot, in the region close to the interference between $\rho^+\pi^-$ and $\rho^-\pi^+$. Modes which include one or two kaons present a background which is dependent on the efficiency of K/π discrimination provided by the DIRC. In particular, the $B^0 \to K^\pm\pi^\mp\pi^0$ mode is expected to be kinematically very similar to the $\pi^+\pi^-\pi^0$ mode due to the similar mass and width of the ρ and $K^\star$ resonances. It should be noted that some of these processes have not been observed experimentally, or their branching ratios are poorly determined, and so their relative importance with respect to the 3π mode can only be estimated.

The significance of the physics backgrounds must be considered in the context of their relative abundance, their persistence following cuts, and their position in the Dalitz Plot.

Clearly, with branching ratios of the same order as that of the signal, these channels represent a numerically insignificant background compared to the continuum. However, since they arise from genuine B decays, they are likely to survive both the pre-selection cuts and the event shape cuts, designed to suppress the $q\overline{q}$ background, with high efficiency. For the 2π and 4π cases some kinematic separation can be used, whereas suppressing the $B^0 \to K^{\pm}\pi^{\mp}\pi^0$ mode would rely on PID techniques, since it is kinematically very similar to $B^0 \to \pi^+\pi^-\pi^0$. In order to assess the likely impact of physics backgrounds on $B^0 \to \pi^+\pi^-\pi^0$, several of the modes discussed above were studied ($B^0 \to \pi^+\pi^-$, $B^0 \to 4\pi$, $B^0 \to K^+\pi^-$). The efficiencies for these modes to pass the pre-selection stage are given in table 5-5. While this study of a sample of physics modes was non-exhaustive, it illustrates that channels containing a number of final state pions and/or kaons can represent a significant background.

Table 5-5. *Efficiency of physics background modes for pre-selection cuts*

background mode	signal pre-selection mode		
(with $B^0 \to X$)	$\pi^+\pi^-\pi^0$	$\pi^+\pi^+\pi^-$	$\pi^+\pi^0\pi^0$
$B^0 \to \pi^+\pi^-$	0.84	0.44	0.00(2)
$B^0 \to 4\pi$	0.01	0.04	0.00(0)
$B^0 \to K^+\pi^-$	0.84	0.47	0.00(2)

In order to reduce kaon contamination in the charged pion sample, PID information was combined from the different subsystems, to create a kaon selector, which was used to identify kaon candidates with high purity. For each B candidate, the charged pion decay products were checked against the selected kaon list, and the candidate was rejected if either pion was successfully identified as a kaon candidate. The two boolean variables, $\sigma_{\pi^+K^+}$ and $\sigma_{\pi^-K^-}$, were included in the list of discriminating variables used for background suppression.

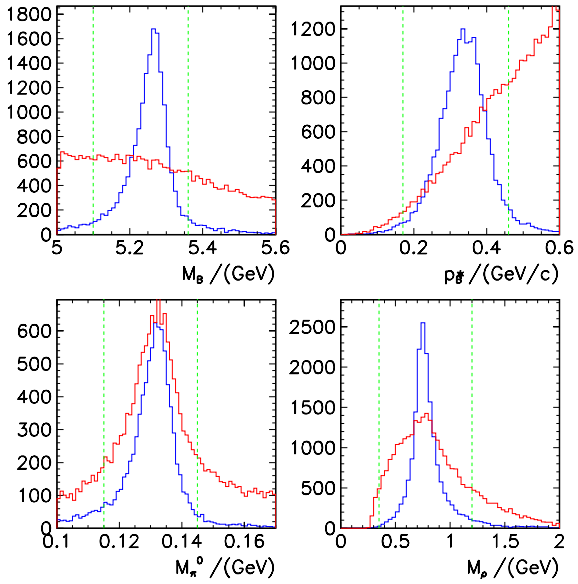

Figure 5-7. *Distributions of cut variables, (before cuts) for 3π signal (blue) and $q\overline{q}$ continuum (red) events (not normalised): $p*_B$, M_B, M_{π^0}, M_ρ.*

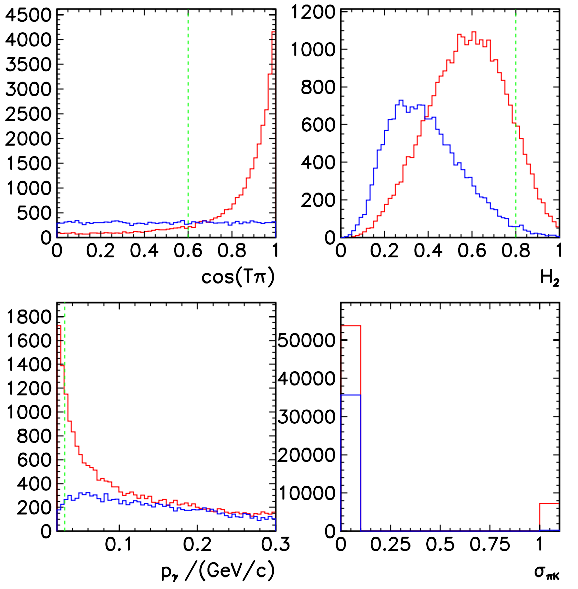

Figure 5-8. *Distributions of cut variables, (before cuts) for 3π signal (blue) and $q\overline{q}$ continuum (red) events (not normalised): $\cos(axis_{TR}\pi)$, $H_2 < 0.8$, p_γ, $\sigma_{\pi^+K^+}$, $\sigma_{\pi^-K^-}$.*

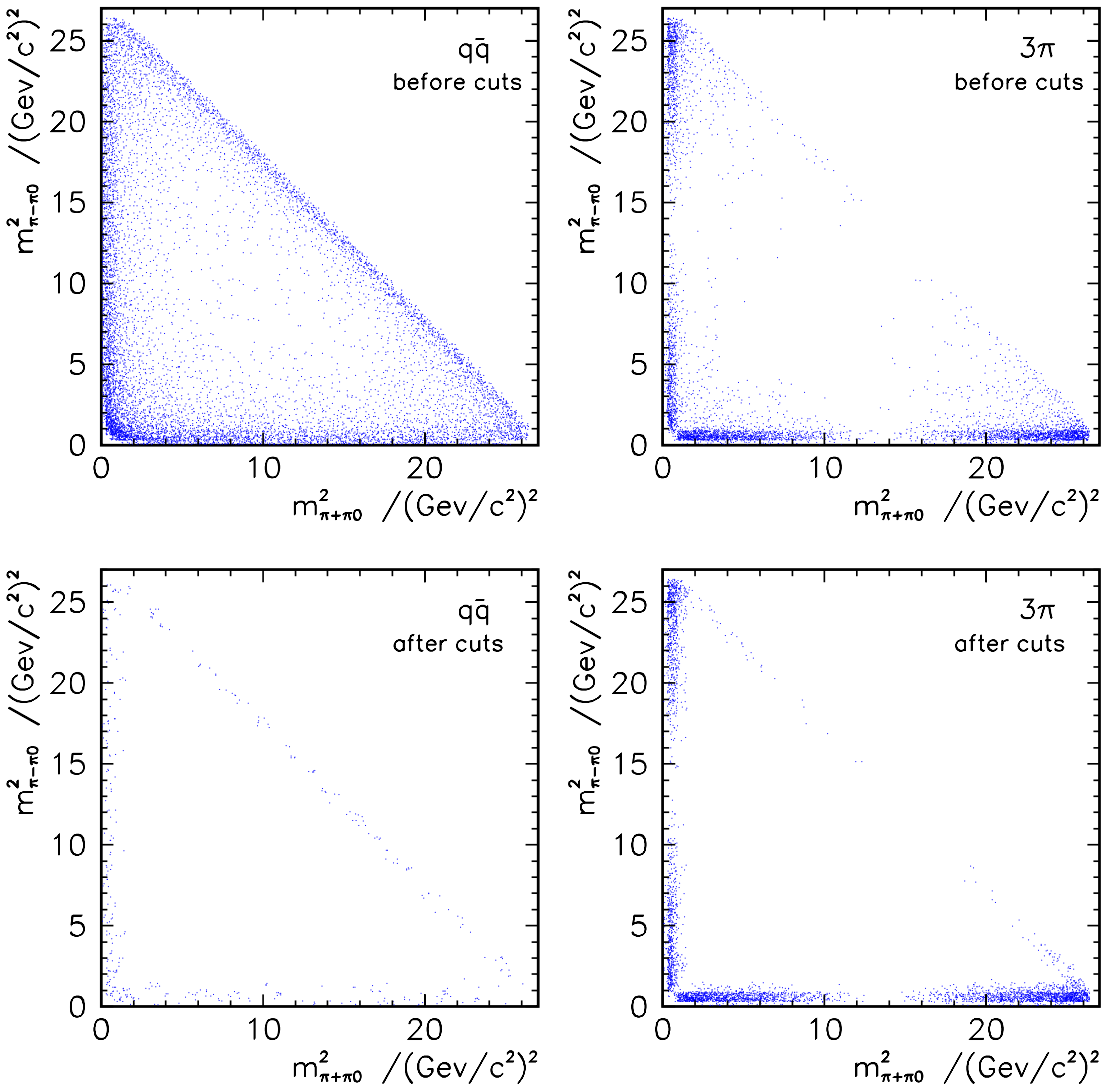

Figure 5-9. *Dalitz Plots for 3π signal and $q\overline{q}$ continuum events before and after the background suppression cuts.*

5.4 Final B^0 Candidate Selection

Initially, the sample of B^0 candidates contains a large combinatorial background, with about five times more background candidates than signal. In addition there are a few events which contain a particularly large number of candidates, sometimes 20 or more. Such events are typically those having a large number of calorimeter objects, especially many low energy clusters.

The "best" B^0 candidate in each event must be specified on the basis of some selection criteria. Previous studies have shown that combinatorial background is largely suppressed by the $q\overline{q}$ fighting methods described above, but nevertheless, several B^0 candidates per event will remain following these cuts, so that a quality factor needs to be applied to rank the candidates. Such a quality factor must be capable of identifying the candidates with the best signal characteristics. One option is to use a set of the discriminating variables already identified for background suppression. However, in order to maintain signal efficiency, only the pre-selection variables, π^0 mass, B^0 mass, and B^0 momentum in the $\Upsilon(4\mathrm{S})$ rest frame, are used. The method of using a χ^2 formed from these variables, is described in section 4.2.2.

The effect of selecting the candidate with the lowest χ^2 in each event is to reduce the signal efficiency by a further 10%. However, of the background candidates which are wrongly selected, 78% are combinations containing the correct π^+ and π^-. In these cases the combinatorial B^0 will have a correctly formed vertex, and time information needed for the CP fit is preserved. Additionally, 24% of these background candidates represent cases where no signal B^0 was reconstructed, and therefore a real gain in information is achieved by their presence.

5.4.1 Increasing Continuum Statistics

The Monte Carlo statistics for continuum available for this study were limited in comparison with the level of continuum expected with real data, *i.e.*, the full Monte Carlo dataset contains only the equivalent of two weeks of data taking at BABAR. In order to gain more statistical significance for the continuum, the technique of sideband-widening was employed. This technique involves widening the cuts for continuum on some variables which do not bias the selection process because they are essentially flat for continuum events, *e.g.*, the mass of the reconstructed B candidate, and the resulting increase in continuum can be accurately determined. The amount of continuum which is kept as a result of the sideband widening is treated as if it was selected using the original cuts, but represents an increase in the original data sample, thus artificially increasing the statistics. The amount of 'effective' continuum was increased by a factor ~ 2 by relaxing the tight cut on M_B to its pre-selection level.

5.4.2 Dalitz Plot Considerations

In using shape variables for continuum suppression the jet-like structure of $q\overline{q}$ events is exploited. However, within the phase-space of $B^0 \to \pi^+\pi^-\pi^0$ decays, it is precisely the ρ-bands, near the perimeter of the Dalitz Plot which have the most jet-like characteristics. This limits the efficacy of the discriminating variables. It is interesting, therefore, to consider the signal available in the central region of the Dalitz Plot, where continuum background is better suppressed. It is known that non-resonant $\pi^+\pi^-\pi^0$ cannot be used for CP studies, since it has unspecified angular momentum. Therefore the presence of an intermediate resonance, such as the ρ, with definite spin is required to fix the angular momentum configuration of the final $\pi^+\pi^-\pi^0$ state. However, resonances other than ρ are expected for $B^0 \to \pi^+\pi^-\pi^0$ decays, which could provide valuable information if branching ratios from B^0 decays turn out to be reasonable. The higher resonances would

appear as bands closer to the centre of the Dalitz Plot, where the background is lower. The most promising of these higher resonances is $f_2(1270)$ which has a branching ratio to $\pi\pi$ of $(84.7^{+2.6}_{-1.2})\%$. ([14])

5.5 Tagging the *b* Quark Flavour

A sophisticated tagging procedure exists as a standard tool in BABAR software [46], and has been implemented here. The details of the approach are described, and some possible areas for further development are considered, although these have not been implemented. The flavour of the tagging B meson is identified by making use of the correlations which

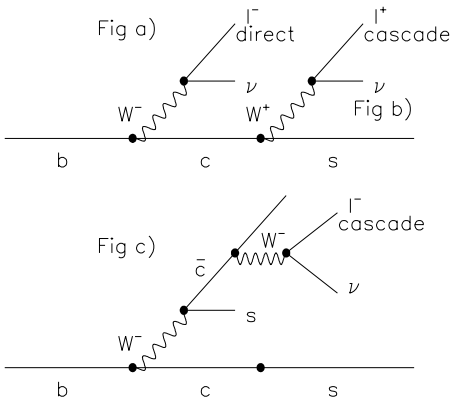

Figure 5-10. *Lepton decay modes for the B^0_{tag} (a) direct lepton, (b) reverse sign cascade lepton, (c) direct sign cascade lepton[13].*

exist between the b quark flavour and the charge of its decay products. There are three possible ways for a lepton to result from the B decay. If the lepton comes directly from the semi-leptonic decay of the B, then it has the same sign as the charge on the b quark, q_b. However, leptons coming from cascade decays can have either same or reverse sign (Fig. 5-10), and these cannot be distinguished. The method for identifying q_b relies on the properties of the primary lepton being distinct from those of cascade leptons, in particular

its momentum distribution is peaked at a much higher value. A multivariate analysis is performed to identify a primary lepton with a certain probability, and this probability is associated directly with q_b.

Another class of tagging mode involves a kaon in the decay. A kaon may come directly from the B in a rare decay, but is much more likely to result from a virtual W or charm decay, so a kaon is almost always a secondary particle, and its charge provides a very efficient discriminating variable. Decay modes which include two leptons, or a lepton and a kaon, are also identified.

The tagging efficiency, ε_{tag}, is essentially independent of the channel under study, and is quoted as being approximately 40% for leptons and 20% for kaons[13]. To evaluate the overall tagging performance a dilution factor must be included, due to the fraction of wrong-sign assignments, w. The dilution factor is estimated to be 40-60%, depending on the tagging mode. The resulting uncertainty in the measured CP asymmetry due to the tagging performance is given by $(\varepsilon_{tag}(1-2w)^2)^{\frac{1}{2}}$, and is expected to be about 35%.

The design of the tagging method based on `Cornelius` is highly sophisticated. However, there are several areas where further developments could prove to be beneficial. Some of these ideas are discussed below.

In the case of an event containing two lepton candidates, if a reverse sign condition is found, it is useful to assess the quality of the second lepton as a tag candidate by applying the multivariate analysis using its properties. A study of the value and sign of q_b derived for each lepton tag hypothesis can then be used to better determine the primary and secondary candidates. The candidate which results in q_b having a magnitude closest to one is used to determine the sign of the B, and to establish the primary/secondary nature of the leptons. This method can also be applied to other categories of event where a second particle is available.

Another development to the tagging algorithm concerns the re-assessment of tag candidates in the case where accurate PID is expected to be low. Since the discriminating variables are flavour-specific, a tag which is mis-identified will provide poor discrimination. Such cases, if they can be found, benefit from applying the multivariate analysis with a different particle hypothesis.

At present, PID is used to provide the best hypothesis for each candidate in the tagging list, however, further information on the quality of a given tag could be gained by including the likelihood for a given hypothesis as a weighting in each tagging procedure. It is also worth noting that there exists an inherent asymmetry in the tagging efficiency of B^0 and $\overline{B}^0$ due to matter-antimatter detection differences in the BABAR detector; since positively and negatively charged hadrons have different interaction cross-sections in the detector, there are different levels of background for positively and negatively charged tagging candidates. This in turn affects the selection efficiencies for each tagging category, and must be taken into account.

It is known that performance of tagging for muons was non-optimal at the time of this study, due to the poor muon identification efficiency which existed in the sample used for training the `Cornelius` package.

5.6 Vertexing

Obtaining precise vertex information for the B^0_{CP} and B^0_{tag} candidates is a central goal of the analysis, as it provides directly the proper time distribution for the CP fitting process. Since the B^0_{CP} is fully reconstructed, it is possible to calculate the decay point by vertexing its decay products. The $B^0 \to \pi^+\pi^-\pi^0$ channel is fortunate in having two charged tracks from which a decay vertex can be formed.

In the case of the B^0_{tag}, however, it is impractical to consider exclusive reconstruction of the decay, since the decay tree will often be incomplete, and a significant fraction of the

tracks are likely to originate from secondary vertices produced by long-lived intermediate particles. There are several ways to handle the tracks from secondary vertices: one approach is to attempt to remove them from the list of tracks used to find the B^0_{tag} decay point. However, the effectiveness of this method depends strongly on identifying such tracks with high purity and efficiency, so that tracks which are genuinely from the B^0_{tag} vertex are not discarded, *i.e.,* in cases where the overall track multiplicity is low, it is more desirable to keep tracks from secondary vertices than to have a situation in which B^0_{tag} vertex resolution is highly degraded due to lack of tracks. Clearly, a balance must be achieved, so careful track selection must take place which optimises the vertex resolution. The alternative approach towards secondary tracks is to include them in the vertexing method, then, either it is necessary to develop a vertexing algorithm which identifies the secondary vertices, or the effect of the secondary tracks can be accounted for in the fit to the vertex distribution; the latter of these methods has been adopted here.

In this analysis, several algorithms for obtaining the z-component of the B^0_{CP} and B^0_{tag} vertices have been implemented and compared. In particular, a novel approach has been studied for the B^0_{tag} vertex which avoids the need for vertexing tracks, and this method is also shown to be highly favorable for the B^0_{CP}, producing better resolution than the other methods which were tested. The effectiveness of the new approach relies upon an accurate determination of the primary vertex on an event-by-event basis, which provides the best estimate of the e^+e^- interaction point (I.P.) for each event.

The methods for obtaining each of the B^0_{CP}, B^0_{tag} and primary vertices are described in the rest of this section. The subsequent fitting procedures used to obtain the Δz and z resolutions for the B^0_{CP} vertex and B^0_{tag} vertex, for both signal and continuum events, are described in section 5.7.

5.6.1 The Primary Vertex

The beamspot at the $PEP\text{–}II$ interaction region is expected to be known to a precision of about 150 μm in x, 7 μm in y and 1 cm in z. The reconstruction of a primary vertex on an event-by-event basis substantially improves the estimated position of the primary interaction point (I.P.), compared to using the average beamspot position. This is significant for the properties of charged reconstructed candidates, since the track parameters of charged tracks are calculated with respect to the nominal I.P[4].

The reconstructed primary vertex position was obtained using the PrimVtxFinder algorithm ([61]). This fits a common vertex to all tracks in the event which have an impact parameter in the x, y plane, calculated at the nominal I.P., of less than 1 mm, (which removes more than 80% of tracks which are K^0_S daughters). The information about the known position of the average beam spot is also incorporated into the fit. This dominates the y-position of the vertex since the beamspot is known to high precision in y.

The performance of the algorithm has been assessed by comparing the reconstructed primary vertex with the true one for each event. For u, d, s, c events, the true primary vertex is the e^+e^- interaction point, whereas for $B\overline{B}$ events, the reference point is taken to be the average position of the two B meson vertices.

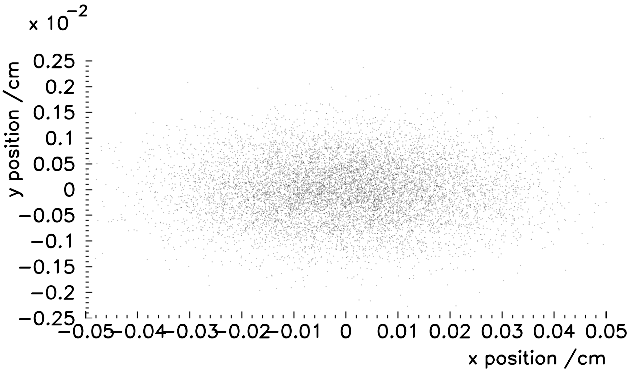

Figure 5-11. *View of the scatter in generated primary vertex position in the transverse plane, for $q\overline{q}$ events (note the different scales in x and y components).*

[4]the resolution on momentum for neutral candidates will not be high enough for this effect to be significant

In light quark continuum events the reconstructed primary vertex is a good estimate of the true primary interaction point, with a resolution of about $63\,\mu\mathrm{m}$ in x, $7\,\mu\mathrm{m}$ in y and $62\,\mu\mathrm{m}$ in z. For charm and $B\overline{B}$ events, the reconstructed primary vertex resolution is degraded by non-Gaussian tails due to the effects of the long charm and B meson lifetimes. The resolution for charm events is about $87\,\mu\mathrm{m}$ in x, $7\,\mu\mathrm{m}$ in y and $99\,\mu\mathrm{m}$ in z. For $B\overline{B}$ events, both B mesons travel along the positive z direction in the lab. frame and so the reconstructed primary vertex is shifted in the positive z direction from the e^+e^- interaction point. The vertex reconstructed by this algorithm therefore represents the midway point between the two decays. This is the appropriate quantity in many applications (*e.g.*, neutral candidates should be pointed back to one of the B vertices). The resolution (using the midway point between the two decaying B mesons as a reference) is $101\,\mu\mathrm{m}$ in x, $10\ \mu\mathrm{m}$ in y and $115\,\mu\mathrm{m}$ in z. The mean z also remains shifted by about $43\,\mu\mathrm{m}$ (the reconstructed z is shifted in the positive z direction with respect to the reference vertex).

The primary vertex has been used to define the reference point for K^0_S decay lengths in the K^0_S selection process. The transverse component of the primary vertex is used in the reconstruction of the z-component of the B^0_{tag} vertex.

5.6.2 Rejection of Tracks from K^0_S Decays

A list of K^0_S candidates was formed by combining and vertexing pairs of all charged tracks from the tagging side of the event, and applying a loose cut on the K^0_S mass. The list was then refined by selecting candidates based on the quality and position of the vertex, Fig.5-13, and by applying a tighter mass cut, $0.493 < M_{K^0_S} < 0.506\,\mathrm{GeV/c^2}$. The vertex position was calculated with respect to the primary vertex, which provides a better estimate of the interaction point for the event than the beamspot. Cuts were applied on the position, ($< 40\,\mathrm{cm}$), and the χ^2, (< 5), of the vertex.

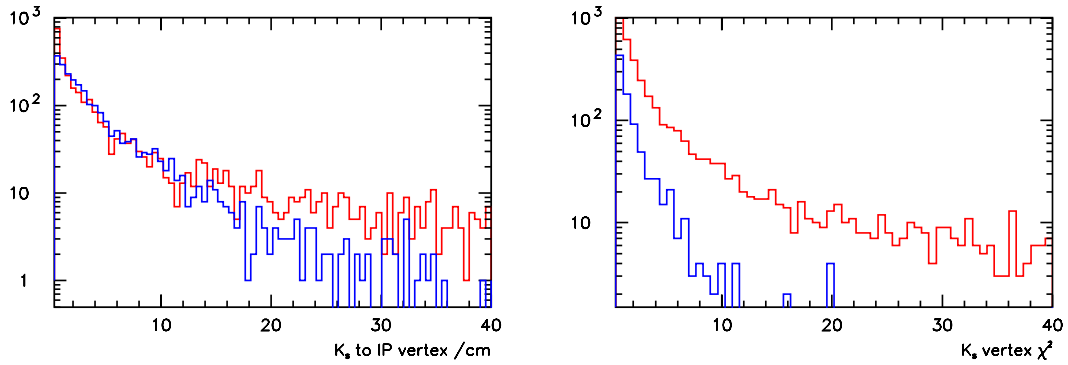

Figure 5-12. *Distributions of quality and position of K^0_S candidate vertices for real kaons (blue) and combinatorial background (red).*

For K^0_S candidates passing the above cuts, the pair of constituent tracks are removed from the list of tracks used to calculate the B^0_{tag} vertex. While the presence of tracks from a real K^0_S in the vertexing will result in a wrongly-calculated vertex position, it is also important not to remove good tracks from the vertexing list, so that the vertex resolution is not degraded. (The average charge multiplicity for signal events is 7.6, including the two charged pions from the B^0_{CP}, for combinatorial background for the signal this is slightly higher, at 7.8, and for continuum background it is 7.2). For this reason, the cuts for K^0_S selection were tight, in order to maintain a high K^0_S purity, and to prevent the removal of many good tracks from the B^0_{tag} vertexing procedure. While this approach necessarily leaves some tracks from real K^0_Ss remaining in the vertexing list, the explicit cut on K^0_S vertex position ensured that these tracks would have a limited effect on the calculation of the B^0_{tag} vertex.

5.6.3 Treatment of Tracks from D Decays

In addition to secondary vertices from K^0_S decays, the vertices from charm decays must be considered. The mean lifetime of the D meson is of the same order ($\sim 10^{-12}$ s) as that of the B, with $\tau_{D^0} \sim 0.4 \times \tau_{D^\pm}$, with a large inclusive branching fraction of B^0 to charm

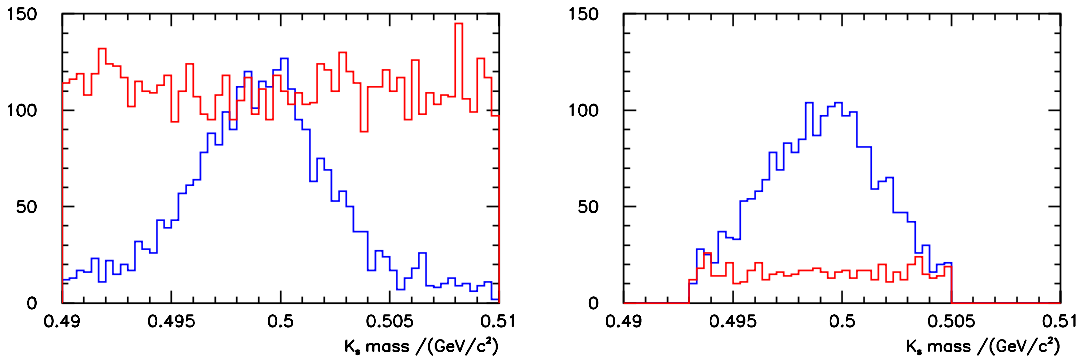

Figure 5-13. *Mass distributions before and after cuts on position and χ^2 of vertex for real kaons (blue) and combinatorial background (red).*

modes, so that tracks from secondary vertices from charm decays present a significant effect when calculating the vertex of the B^0_{tag}, and must be accounted for. Applying a track rejection procedure in the charm case, similar to that described in the previous section, would be more involved, since there is a need to construct a pseudotrack for the D direction, and there is less discriminating power in a cut on the impact parameter. More importantly, the number of tracks removed from the B^0 vertexing by eliminating charm decays is prohibitively large, because it substantially reduces the number of tracks available for vertexing, and thus increases statistical error on the B^0_{tag} vertex position (this observation has been verified by a test in which all tracks from charm decays were removed with 100% efficiency, and the reconstructed vertex resolution was seen to degrade by $\sim 9\%$). For these reasons, it is better to preserve the charm decays in the list of tracks used for vertexing, and then to take account of the systematic error which is introduced by fitting for the charm decay length in the vertex position distribution.

In order to parameterise the effect of charm on the B^0_{tag} vertex, a measurable quantity was sought which could act as an indicator of the charm decay length, λ_D, in a given event. The χ^2/dof of the B^0_{tag} vertex was investigated as a possible indicator, since if the charm has a small decay length in a given event the χ^2/dof of the B^0_{tag} vertex should be good, and vice versa. If a correlation between the measured χ^2/dof and λ_D (from Monte Carlo

truth) could be established, then this could be used to determine the value of λ_D to be used as input to the fit of the B^0_{tag} vertex distribution. The true charm decay length distribution was plotted in bins of the vertex χ^2/dof. There was found to be only a weak correlation present, with several factors contributing to the poor resolution :

- The value of the χ^2 is highly influenced by the relative numbers of tracks associated with the B and D vertices which are included in the B^0_{tag} vertex calculation, as well as the total number of tracks used. In particular, if all the tracks originate from the D decay, then a good χ^2 value will be obtained, but with a large unknown systematic error; this situation occurs in about 7% of signal events. On average, about half of the tracks used in the vertex are associated with the B and half with the D. The true distribution of the number of tracks coming from the B^0_{tag} vertex with the number coming from the D vertex, for signal events, is illustrated in Fig.5-15.

  For a high statistics sample, the correlation between the mean charm decay length and the χ^2/dof is noticable, as shown in Fig.5-15. However, the variation on an event-by-event basis, due to other influencing factors, is too great to exploit this information.

- A simple model was assumed, in which the z-component of the charm decay was represented by a single exponential. This neglected the effects of the boost, the presence of two lifetime components from D^0 and $D^{\pm}$, and the projection of the actual D decay path onto the z-axis. Some improvement to the fit to the distribution was achieved by allowing for the projection onto the z-axis, which has been modelled by a functional form consisting of a set of exponentials with effective decay length $\lambda = \lambda_D \cos\theta$, distributed flat in $\cos\theta$. The improved performance of this fit compared with a single exponential can clearly be seen in Fig.5-16. The effect of the boost can also be seen in the distribution, with the majority of Ds displaced forwards in z from the B^0_{tag} vertex. The small number of backward-going Ds have been neglected in this study.

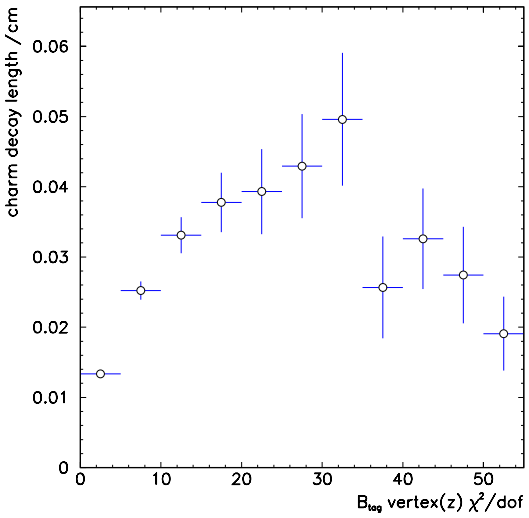

Figure 5-14. *The mean true charm decay length in bins of the calculated χ^2 of the z-component of the B^0_{tag} vertex, for signal events.*

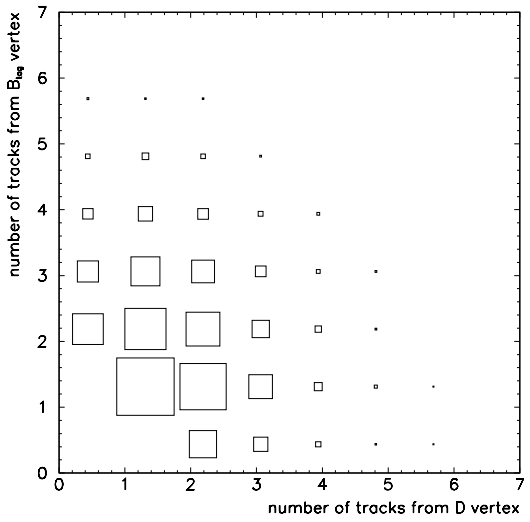

Figure 5-15. *The number of reconstructed tracks used in B^0_{tag} vertexing which came directly from the B^0_{tag} decay or from a secondary charm decay, for signal events.*

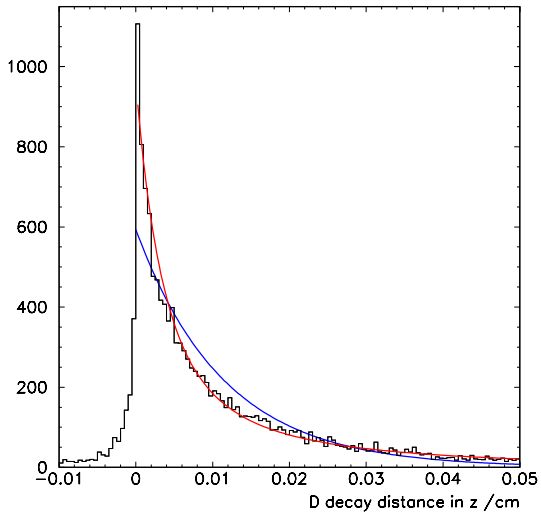

Figure 5-16. *Distribution of the z-component of the true D decay length for signal events, showing the comparison of a multi-exponential fit (red) and a single exponential fit (blue).*

The following section describes the method used to reconstruct the B^0_{tag} vertex, and incorporates a treatment of the charm decay component in fitting the vertex resolution.

5.6.4 Reconstructing the B^0_{tag} Vertex

Obtaining a precise vertex for the tagging B^0 is a much more complicated procedure than vertexing the B^0_{CP}, and presents one of the most significant challenges in all CP analyses for BABAR. In the ideal case, the tagging B^0 would be fully reconstructed using all tracks in the event which are not included in the CP mode. However, due to the high occurrence of secondary vertices in the tagging mode, from charm decays and K^0_Ss, it is difficult to isolate the vertex of the tagging B. This results in the resolution on the B^0_{tag} vertex position being a limiting factor in the analysis.

Several sophisticated fitting techniques have been proposed for BABAR which handle the secondary vertices, either by eliminating them via some selection criteria, or by attempt-

ing to reconstruct them. However, it is interesting to consider an alternative approach in which the track position information can be combined without the need to carry out a complicated fitting procedure for the B^0_{tag} vertex. In particular, it is worth emphasising that it is *only* the z component of the decay point for each B which is of interest, and not the full vertex position in three dimensions.

One such approach could use a simple summation of the track impact parameters weighted according to their errors. The impact parameter (distance of closest approach to the origin) of each track is not the appropriate quantity to use here though, since the error on the z component of the B^0_{tag} vertex is large compared to the error on the transverse component. Rather, it is the distance of closest approach of each track to a z-axis passing through the B^0_{tag} vertex point, the $z_{B^0_{tag}}$-axis, which would provide a realistic estimate of the z component of the B^0_{tag} vertex, $z0_{tag}$. If this $z_{B^0_{tag}}$-axis can be estimated with sufficient precision for each event then $z0_{tag}$ can be calculated as follows,

$$z0_{tag} = \frac{\sum_{trk} \frac{z0_{trk}}{\sigma^2_{z0_{trk}}}}{\sum_{trk} \frac{1}{\sigma^2_{z0_{trk}}}}, \tag{5.3}$$

where the summation takes place over all charged tracks in the event which are not associated with the B^0_{CP} decay mode (see section 5.6.5), or with identified K^0_S candidates (see section 5.6.2).

A study of the effectiveness of this approach has been carried out using a large sample of light quark continuum events, where the effects of charm decays are not present. Use has been made of Monte Carlo truth information to demonstrate the improvements achieved at each stage (but there is, of course, no reliance on Monte Carlo truth in the method itself). For u, d, s events, the putative B^0_{CP} and B^0_{tag} candidates share the same vertex, which is the decay vertex of the quark pair.

The method depends strongly on the accurate determination of the $z_{B^0_{tag}}$-axis for each event. The $z_{B^0_{tag}}$-axis position has been estimated from the transverse component of the

primary vertex. Clearly, this provides the best possible reconstruction of the $z_{B^0_{tag}}$-axis position for u, d, s continuum events, since all tracks not deemed to originate from K^0_S decays are vertexed. It is argued that the calculated primary vertex also provides a good estimate of the $z_{B^0_{tag}}$-axis for signal events. The two charged pions from the B^0_{CP} have relatively high, and therefore well-defined, momentum, so it is advantageous to keep these tracks for vertexing when the tracks from the tagging B may be few in number, or ill-defined. Also, in signal events the tracks from charm decays often have high transverse momentum, so that the bias towards the B^0_{CP} vertex in the transverse plane somewhat offsets the bias towards the charm secondary vertices. In approximately 10% of both signal and continuum events the primary vertex is badly formed by the vertex-fitting procedure[5]. About half of these events have a well-formed B^0_{CP} vertex, however. The transverse component of the B^0_{CP} vertex is found to have a good correlation with the true transverse B^0_{tag} vertex position, for both continuum and signal events, so it can be used in the correction calculation when no good primary vertex is available.

Correcting for the transverse component of the vertex

The point of closest approach of a track to the nominal $z_{B^0_{tag}}$-axis (*i.e.*, $x = 0, y = 0$) is given by $d0$, and the z-component of this point is $z0$. If the distance between the true $z_{B^0_{tag}}$-axis for the event and the nominal $z_{B^0_{tag}}$-axis is D, then a correction, $\Delta z0$, can be made to $z0$ as follows : The direction cosines of the reconstructed track are used to estimate the projection of the true track from its point of origin (the B^0_{tag} vertex) to its point of closest approach to the nominal $z_{B^0_{tag}}$-axis. z_{corr} defines the point of intersection of a line perpendicular to the track with the nominal $z_{B^0_{tag}}$-axis. Assuming θ and ϕ (the angles in cylindrical coordinates) for the track are constant over this range,

$$\Delta z0_{tag} = z0_{tag} - z_{corr} = \frac{1}{\tan\theta}(x_{IP}\cos\phi + y_{IP}\sin\phi) \tag{5.4}$$

[5]there is a good argument here for developing a 2-dimensional primary vertex finding algorithm, to reconstruct just the transverse component

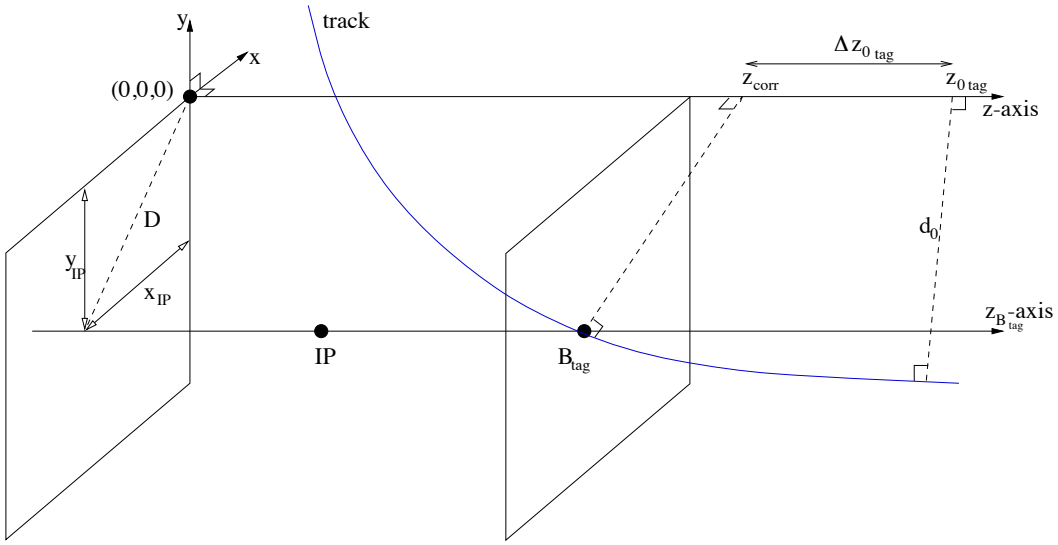

Figure 5-17. *Diagram showing the correction needed to $z0_{tag}$ for a track, not to scale.*

where (x_{IP}, y_{IP}) is the transverse position of the primary vertex. Due to the constraints imposed by the beamspot, the y-component of this expression is negligible compared with the x-component, and can be disregarded.

The correction was calculated for each track used in the B^0_{tag} vertex, for samples of signal and continuum events. In cases where a well-formed reference vertex (primary or B^0_{CP}) exists, the resulting z-resolution obtained with the corrected $z0$ values showed $\sim 5-10\%$ improvement over the uncorrected method.

Correcting for the pulls of track errors

The simulated data is subject to potential inaccuracies in the estimates of track errors, just as the real data. A technique for assessing the accuracy of track errors is the use of pull distributions. If the errors on a quantity are correctly estimated then a pull distribution of that quantity will be a Gaussian with a σ of 1. With the availability of Monte Carlo truth information, the pull of the $z0$ value for a given track is,

$$pull_{z0} = \frac{z0_{trk}(meas) - z0_{trk}(true)}{\sigma_{trkz0}} \tag{5.5}$$

This technique is also valid in the case of real data : well-identified u, d, s continuum events could be used to assess the quality of the error on the $z0$ of a given track, since it is known that all tracks originate from a common vertex. In this case, the true $z0$ of the track is replaced by the mean $z0$ of the other tracks in the event.

The track pull distributions were plotted in bins of track momentum and also $\tan\theta$. There was found to be essentially no correlation with $\tan\theta$, but the mean of the pull distributions was found to be positively correlated with momentum. The track errors were corrected accordingly, using the relationship,

$$\sigma_{trkz0}(corrected) = \sigma_{trkz0}(original) + (a * \log p_{trk} + b) \tag{5.6}$$

where the two parameter values were obtained from the fit to the pulls for continuum events ($a = 0.1726(\,\mathrm{GeV/c})^{-1}$, $\mathrm{b} = 1.048$). The momentum dependence of pulls indicates that some underestimate of the amount of material present in the SVT has probably occurred in the simulation. The results of correcting track errors using the pull information have a relatively small impact on the z-resolution for the B^0_{tag} vertex due to the number of events where only one track contributes to the vertex, and so the relative track weightings play no role.

Cut on the x-component of the primary vertex

It is known that for some events the primary vertex is poorly constructed. The presence of long tails on the distribution of the x-component of the primary vertex indicate that these cases correspond to very large values of x_{IP}, when clearly it is better to not to apply the correction. A cut of $x_{IP} < 450\,\mu\mathrm{m}$ affects about 7% of events. Of these, 50% have a $x_{B^0_{CP}}$ value of less than $450\,\mu\mathrm{m}$, allowing the correction to be made using the B^0_{CP} vertex as a reference. The remaining events have no correction applied to the calculated $z0_{tag}$ value.

Cut on σ_{trkz0}

If the track errors were weighted perfectly, (*i.e.*, pull distributions correct), then adding new tracks with large error to the vertex calculation would improve (if only slightly) the

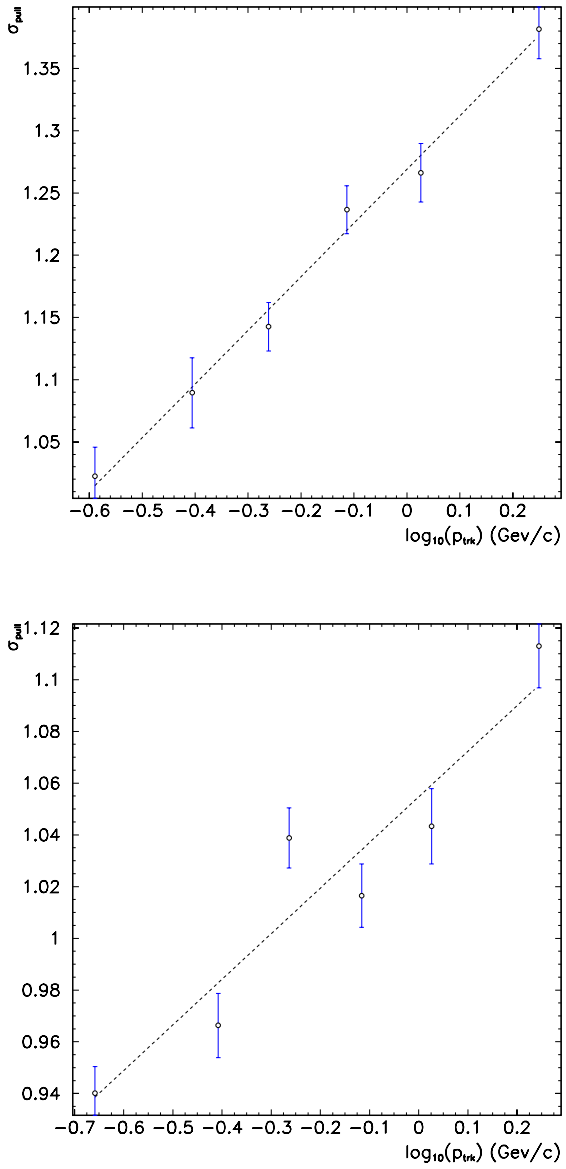

Figure 5-18. *Variation of σ for the Gaussian-fitted pull distributions of track z0 errors as a function of $\log(p_{trk})$ for signal (left plot) and u, d, s continuum events (right plot). A linear fit has been used in each case.*

overall resolution obtained, since information would be added with the correct weighting. However, the pull study showed that this was not the case, and so an improvement in resolution can be gained from a cut on σ_{trkz0}. A cut of $\sigma_{trkz0} < 0.001$ was chosen so that the resolution was not degraded by the loss of too many tracks.

Fitting the z-resolution distributions

It is commonly the case that a double-Gaussian fit is applied to the z resolution distribution, since this allows a straightforward estimate of the resolution to be obtained using the σ of the narrow Gaussian. However, such a method gives a poor fit, and is particularly inadequate for the B^0_{tag} vertex for signal events where the charm lifetime has been shown to introduce an asymmetry. It is reasonable to assume that the error on the $z0$ value for a given event obeys a Gaussian distribution. So the natural extension of this is to represent the $z0$ distribution of many events by a multi-Gaussian function. Such a function [62] has been used here to fit the $z0_{tag}$ resolution for the $q\overline{q}$ sample. The function consists of the sum of all Gaussians with σ within a specified continuous range (σ_{min} to σ_{max}) according to a $\frac{1}{\sigma_2}$ distribution. The value of σ quoted from the fit is the mean of the σs from the constituent Gaussians.

Two functions were used to fit the z resolution for the 3π signal sample, and the results of these were compared. The first was a multi-Gaussian fit in which the Gaussians were constrained to have the same mean value, but the mean value itself was allowed to vary. The second function was a multi-Gaussian convoluted with a single exponential term of decay length λ. In this function, the mean of the Gaussians was fixed to zero, so the asymmetry of the distribution was fitted by the exponential component.

The results in table 5-6 show that both types of fitting function are able to identify the charm component, as given by the values of mean and λ respectively. The values are around 30 μm, which corresponds to the mean decay length for one charm lifetime. The function which includes the exponential component is seen to give a better fit (lower χ^2).

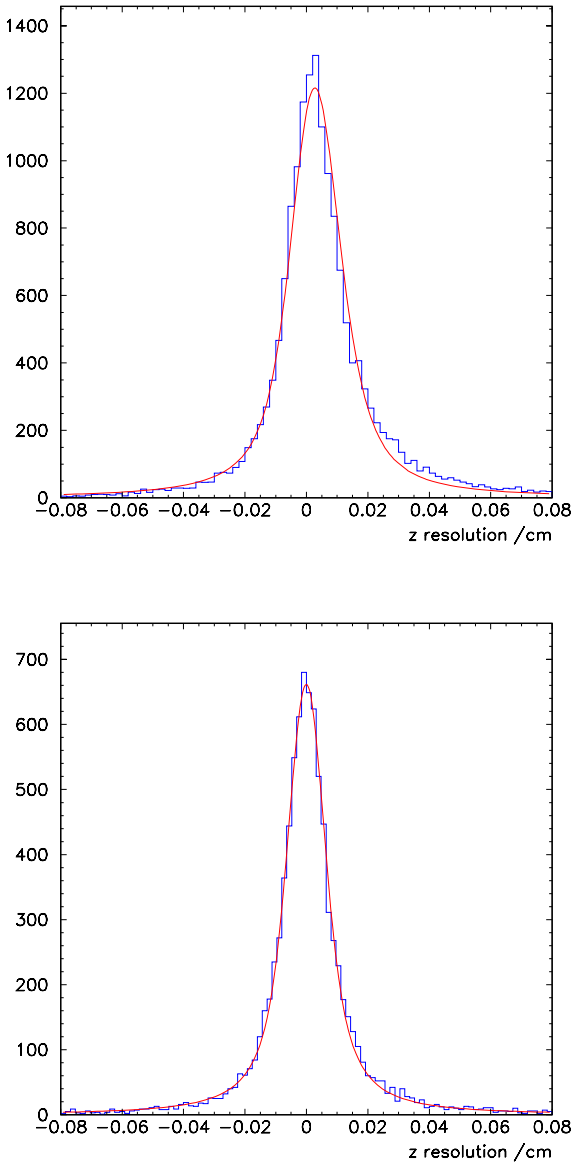

Figure 5-19. *Resolution of the z component of the B^0_{tag} vertex for signal (left) and u, d, s continuum (right) events; the signal distribution has been fitted with a multi-Gaussian convoluted with an exponential function, and the continuum distribution is fitted with a multi-Gaussian function.*

Table 5-6. *A comparison of different methods for obtaining the z component of the B^0_{tag} vertex, for $B^0 \to \pi^+\pi^-\pi^0$ events and $q\overline{q}$ (u,d,s) events*

weighted z0 method	3π signal events			$q\overline{q}$ (u,d,s) events		
	σ μm	mean (λ) μm	χ^2/dof	σ μm	mean μm	χ^2/dof
uncorrected	58.8 (55.5)	30.0 (33.9)	5.9 (5.0)	44.2	0.35	1.00
+ transverse correction	54.5 (51.2)	28.0 (31.8)	5.4 (4.8)	42.7	1.18	0.91
+ weighting correction	54.3 (51.0)	28.2 (31.9)	5.8 (5.1)	42.4	0.79	0.94

5.6.5 Reconstructing the B^0_{CP} Vertex

The B^0 from the CP mode has been fully reconstructed from its decay products, $\pi^+\pi^-\pi^0$. The three πs are always produced at the B^0_{CP} decay vertex, *i.e.*, the presence of a ρ intermediate state in the decay does not affect the vertex in this sense, since the ρ resonance lifetime is small ($\Gamma \simeq 151\,\mathrm{MeV}$). Therefore, the B^0_{CP} decay position can be obtained simply by vertexing the two charged pion candidates from the putative B^0. However, some track selection procedure is also required, since in background events a significant number of the pion candidates may come from K^0_S decays, or D decays. Although this problem is quite rare in signal events, there are some occasions when one (or both) of the pion candidates may have an unusually high z_0, such as when the π momentum is almost parallel with the $z_{B^0_{tag}}$-axis; these events need to be discarded in order to maintain good overall vertex resolution. Therefore, a loose cut of $|z_0| < 1.5\,\mathrm{mm}$ was made for each pion candidate. In addition, a π^+ or π^- candidate was discarded if found to be associated with a K^0_S candidate. These two cuts produced a negligible loss of signal efficiency.

The method of vertexing the $\pi^+\pi^-$ pair in order to obtain the B^0_{CP} vertex clearly has implications for the distribution of vertexed B^0_{CP} candidates in the 3π phase space, as it deals only with charged pions. The bias on B^0_{CP} vertex resolution in favour of the charged ρ modes can be reduced (but not eliminated) by including information from the π^0 in the

Table 5-7. *Comparison between different methods for obtaining the $z$component of the B^0_{CP} vertex, for $B^0 \to \pi^+\pi^-\pi^0$ events and $q\overline{q}$ (u,d,s) events*

	3π signal events			$q\overline{q}$ (u,d,s) events		
	σ μm	mean μm	χ^2/dof	σ μm	mean μm	χ^2/dof
vertexing methods						
BetaKFit	26.6	0.15	3.18	28.2	0.52	1.85
$\pi^+\pi^-$ vertexing	26.8	0.18	3.15	28.5	0.61	1.94
weighted z0 methods						
uncorrected	29.9	1.50	1.79	29.0	0.59	1.48
+ transverse correction	22.9	1.54	1.24	23.9	0.09	0.98
+ selective transverse correction	23.3	1.63	1.74	23.2	0.12	1.53
+ optimised transverse correction	22.8	1.50	1.85	23.1	0.23	1.58

vertexing process, *i.e.*, by making a kinematic fit which takes into account the π^0 energy. This has been carried out using the software package `BetaKFit` ([63]), which can be used to build a decay tree with optional mass constraints. The full covariance matrix for the resulting vertex is also calculated. The resulting B^0_{CP} vertex and its error provided a small improvement over the $\pi^+\pi^-$ vertexing method, since the additional π^0 information adds to the overall fit with only a small weighting due to the large uncertainty on the π^0 momentum compared with that for the charged tracks. It was found that the success rate for producing a vertex using the kinematic fit was slightly lower than for the $\pi^+\pi^-$ vertexing method, due to a few cases where the fit failed to converge.

In addition to the two full-vertexing methods, the weighted $z0$ method was used to find the z component of the B^0_{CP} vertex using the $\pi^+\pi^-$ tracks from the reconstructed signal B^0_{CP}, and their errors. All the techniques which have been described for the B^0_{tag} case were applied using the signal π^+ and π^-. The resulting resolutions from the three methods are compared in Table 5-7, and show that the weighted $z0$ method offers the best performance.

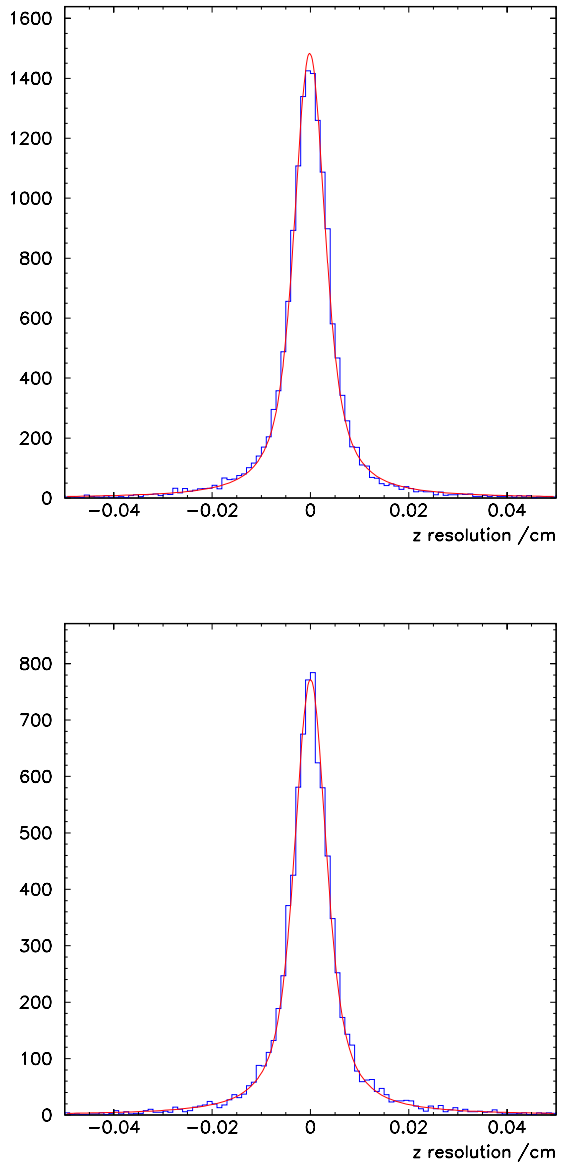

Figure 5-20. *Resolution of the z component of the B^0_{CP} vertex for signal and u, d, s continuum events; both distributions are fitted with a multi-Gaussian function.*

The resolution on the vertex is a function of phase space, due to the distributions of the three π momenta. Here, the ρ resonance plays a role, due to its polarisation, since it contains one high momentum and one low momentum constituent pion. The relative momentum distributions of the three πs are summarised in the Dalitz Plot. The best kinematic conditions for constructing the B^0_{CP} vertex involve both charged πs having high momentum, with an opening angle between the tracks close to 90°. Both of the charged pions have simultaneously high momenta in the interference region between $\rho^+\pi^-$ and $\rho^-\pi^+$, (*i.e.*, the lower left-hand corner of the Dalitz Plot). However, the kinematic configuration of final states in the ρ-bands has a pseudo-2-body structure, which means that the charged pions are almost back-to-back near the edges of the Dalitz Plot, (and conversely their opening angle reduces towards the middle of the Dalitz Plot).

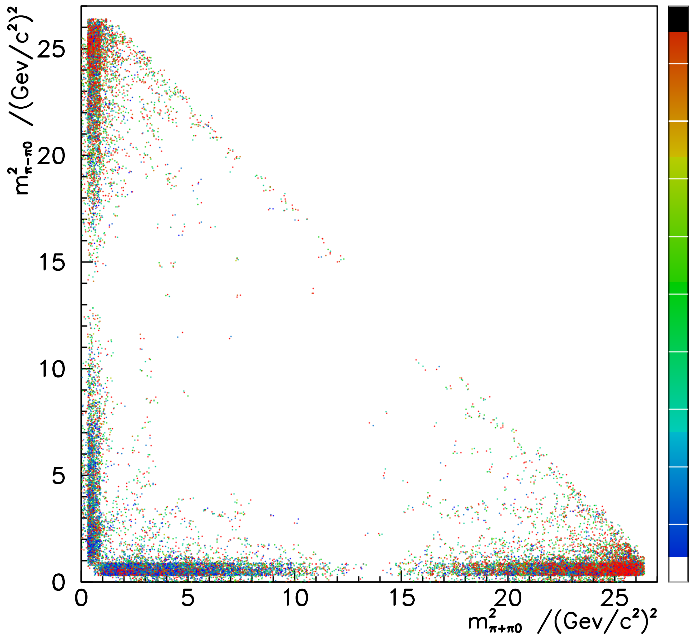

Figure 5-21. *Dalitz Plot showing variation in vertex resolution for the reconstructed B^0_{CP} candidate as a function of the 3π phase space (before final event selection). On the colour scale, blue represents a good vertex and red represents a bad vertex, according to the χ^2 of the vertex.*

5.7 The Proper Time Distribution for B Decays

The information required for CP fitting is the proper time distribution between the B^0_{CP} and the B^0_{tag}, together with the tagging information. At the $\Upsilon(4S)$, the $B\overline{B}$ pair are produced with small momenta in the $\Upsilon(4S)$ rest frame. At BABAR the typical transverse momentum of the B mesons is $\sim 300\,\mathrm{MeV}$, which is negligible compared to the boost of the $\Upsilon(4S)$, β, (it is assumed here that both Bs experience a boost equal to β). Therefore, to a good approximation, the proper time distribution can be obtained from the Δz distribution by the simple relationship,

$$t = \frac{\Delta z}{\beta\gamma} \tag{5.7}$$

Fits have been applied to the measured Δz (*i.e.*, $z_{CP} - z_{tag}$) distribution and its resolution according to Monte Carlo truth (*i.e.*, $(z_{CP} - z_{tag})_{measured} - (z_{CP} - z_{tag})_{true}$), for both signal and continuum events, in order to provide estimates of the resolutions on these quantities. The resolution obtained for the signal Δz distribution was $\sigma = 170\,\mu\mathrm{m}$, using a multi-Gaussian fit convoluted with an exponential component (to model the charm contribution). The remaining distributions (Δz for $q\overline{q}$ and Δz-resolutions for signal and $q\overline{q}$) were fitted with a multi-Gaussian. The resolution for the $q\overline{q}$ Δz distribution was $\sigma = 57\,\mu\mathrm{m}$, and for the Δz-resolution distribution was $\sigma = 68\,\mu\mathrm{m}$. The detailed fits to the Δz distributions are the subject of the next chapter.

While much emphasis is placed on obtaining the best z resolutions for signal events, it is also important to simultaneously reduce the z resolutions for $q\overline{q}$ events as much as possible. If the z resolutions for u, d, s backgrounds are very small, (*i.e.*, so that $\sigma_{\Delta t} << \tau_{B^0}$), then the negative effect of their presence in the event sample used for CP extraction is reduced because there are less background events contributing to the Δt distribution in regions most sensitive to the measurement of CP asymmetry.

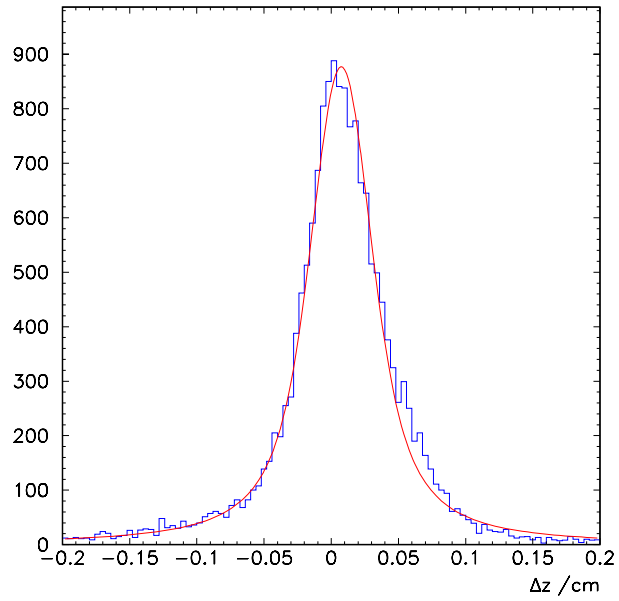

Figure 5-22. *Δz distribution for signal events.*

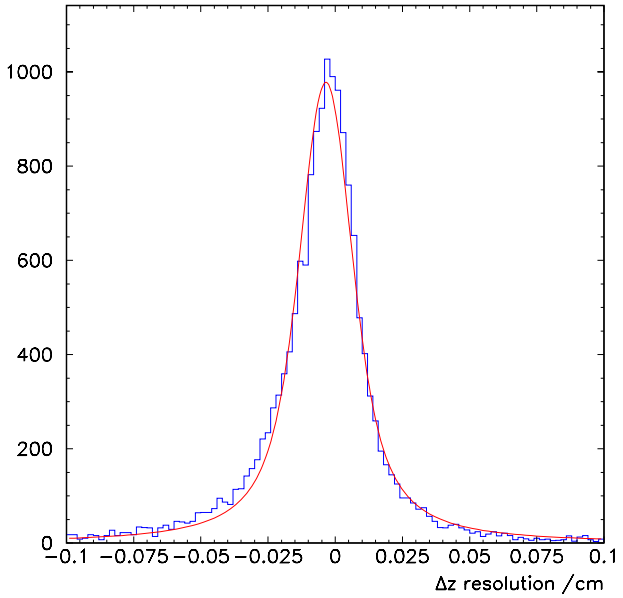

Figure 5-23. *Distribution of Δz resolution with respect to Monte Carlo truth for signal events.*

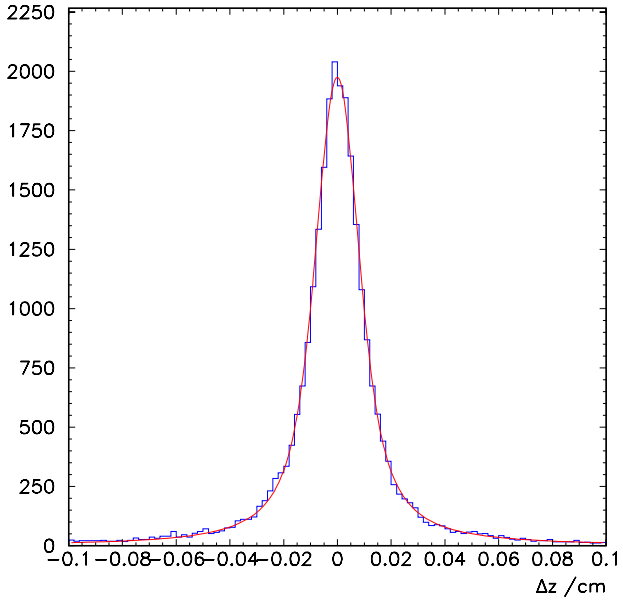

Figure 5-24. *Δz distribution for u, d, s continuum events.*

Since the true point of origin of both the B^0_{CP} and B^0_{tag} candidates is the I.P. in the case of u, d, s continuum events, the resolution on the Δz position is equal to Δz itself. This is a powerful observation, as it means that various vertexing algorithms can be exercised on u, d, s-identified events in real data to determine their likely resolution.

5.7.1 Correlations between Selection, Vertexing and Tagging

The procedure for B candidate selection, described in section 5.4, is not expected to have a significant effect on the Δz distribution for signal or background, as the selection variables used do not depend on the time evolution of the B mesons.

However, there are considerable correlations between the B^0_{tag} vertexing and the tagging, since they both depend strongly on the nature of the charged tracks from the tagging side of the event. The possible correlations which exist between selection, vertexing and

tagging can readily be seen using an illustration. Events which contain a well-defined high momentum lepton from the B^0_{tag} are considered : in such cases the tagging efficiency is expected to be high, and in addition, the thrust axis for the B^0_{tag} decay should be well-defined. Also, since the resolution on the B^0_{tag} vertex is the limiting factor in obtaining the Δz for an event, a good value for $z0_{tag}$, where the lepton is used with high weighting, will be of direct benefit. However, in events where the tagging particle is mis-identified, and actually originates from the B^0_{CP} decay, the above effects will conspire to give the wrong information for the selection and the vertexing as well.

5.8 Summary

The event selection for the $B^0 \to \pi^+\pi^-\pi^0$ channel has been described, with consideration given to the nature and extent of backgrounds which are likely to be most significant, and in particular the light quark continuum background. The selection efficiencies were found to be 0.12 for 3π, 0.39×10^{-4} for u, d, s, and 0.30×10^{-4} for $c\overline{c}$ events. At this level, the amount of background contamination would severely impact an analysis of the $B^0 \to \pi^+\pi^-\pi^0$ channel. However, there exists some scope for improving the selection procedure and implementing cut optimisation techniques which could yield a higher signal to background ratio. The uncertainties associated with the lack of machine background effects in this study make it impractical to consider such optimisation at this stage.

The procedures for tagging and vertexing the B candidates from the event sample have been shown. A detailed study for obtaining the z-components of the B^0_{CP} and B^0_{tag} vertices was carried out, and was found to provide improvements in resolution of 15% for signal, and 19% for $q\overline{q}$, for the B^0_{CP} vertex, and 8% for signal, and 4% for $q\overline{q}$, for the B^0_{tag} vertex. The final resolution of the Δz distribution using the new vertexing method was $68\,\mu\mathrm{m}$. The typical distance between B decays in the lab. frame is $\sim 250\,\mu\mathrm{m}$. Therefore

the precision to which Δz can be measured facilitates the extraction of CP asymmetry. The Δz distributions, combined with the tagging values, for the signal and continuum samples, provide the information necessary for a CP analysis of this channel.

6

Determination of the CP angle α for $B^0 \to \pi^+\pi^-\pi^0$

6.1 Introduction

The current experimental programme in High Energy Physics for studying CP violation includes a number of existing and planned experiments which will have the capability to make a precise measurement of the CP angle β. However, the aim of BABAR is not only to observe and measure CP violation in B decays, but to establish whether the Standard Model explanation of CP violation is correct. This requires fully (over) constraining the Unitarity Triangle, and in order to do this, it is essential to make a precise measurement of α. Decays which proceeds via $b \to du\overline{u}$ provide a possible mechanism for extracting the CP angle α, which is the angle between $V_{ub}{}^*V_{ud}$ and $V_{tb}{}^*V_{td}$; these include the 2π, 3π and 4π modes.

The $B^0 \to \pi^+\pi^-\pi^0$ channel offers some interesting features for studying CP violation. The decay proceeds predominantly through $\rho\pi$, and the three modes, $\rho^+\pi^-$, $\rho^-\pi^+$ and $\rho^0\pi^0$, are expected the exhibit large interference effects due to the polarisation of the ρ. This is clear from a study of the 3π Dalitz Plot, where the greatest density of events is seen to be in the corner regions where the ρ bands overlap. In the full three-body analysis, the interference regions provide additional terms in the fit, providing extra constraints which can be used to help lift the degeneracy of the solutions for α, which would otherwise compromise the analysis. The full three-body CP fit to the Dalitz Plot is a complicated

procedure involving 11 parameters, and will require several years' data-taking before it can be carried out effectively. The analysis presented here has not exploited all the information in the Dalitz Plot, but has instead focused on the three ρ bands where a reasonable signal to background ratio can be obtained. In the two-body treatment, the interference regions are not considered, and the $\rho^+\pi^-$, $\rho^-\pi^+$ and $\rho^0\pi^0$ modes are regarded as separate channels. It is possible to extract the CP asymmetry in this case, even though the two-body modes are non-CP eigenstates. The two-body approach is a simpler analysis, which can be used for earlier studies of this mode, and as a check on the three-body approach.

All α channels suffer from the possibility of penguin contributions [64]. In early studies of modes to be investigated at BABAR, $\pi^+\pi^-$ was considered the primary mode for measuring α, since it is a CP eigenstate. However, recent evidence from the CLEO experiment, [65] suggests that the branching ratio for this channel is smaller than originally expected, and that the penguin contributions are larger. The 3π mode is also likely to suffer from penguin contributions [66], but the current estimate of the $\rho\pi$ branching ratio is consistent with the expected value, so that the 3π mode may prove to be the best means of measuring α.

The expected branching ratios for the three modes, $B^0 \to \rho\pi \to \pi^+\pi^-\pi^0$, are given in table 6-1. The relative amplitudes for each mode vary with assumed penguin amplitude, however the estimated inclusive branching ratio for the six processes $B^0, \overline{B}^0 \to \rho\pi$ remains 5.5×10^{-5}.

The ultimate feasibility of the 3π analysis will depend on the actual branching ratios of the ρ-mediated decays, the distribution of events in the 3π phase space, and the relative strength of tree and penguin amplitudes.

The following sections begin with a description of the theoretical model for the $B^0 \to \pi^+\pi^-\pi^0$ analysis, including a discussion of the various simplified approaches which can be explored. This provides the context for justifying the procedure which has been

Table 6-1. *Branching ratios and amplitudes used in these studies. The Penguin amplitudes were derived from theoretical models. [13]*

Mode	Branching Ratio	Tree Amplitude	Penguin Amplitude
$B^0 \to \rho^+\pi^-$	4.4×10^{-5}	$T^{+-} = 1.00$	$P^{+-} = -0.09$
$B^0 \to \rho^-\pi^+$	1.0×10^{-5}	$T^{-+} = 0.47$	$P^{-+} = 0.01$
$B^0 \to \rho^0\,\pi^0$	0.1×10^{-5}	$T^{00} = 0.14$	$P^{00} = \frac{-1}{2}(P^{+-} + P^{-+})$

adopted in this analysis. A discussion of the fitting procedure for extracting a value of α is then given, together with the results obtained from this method.

6.2 Theoretical Context

6.2.1 *CP* extraction from non-*CP* eigenstates

The full 3π distribution contains both CP-odd and CP-even states, which it is not possible to distinguish. However, the presence of an intermediate resonance in the decay provides angular information which specifies the CP eigenstate. The 3π mode must therefore be studied via resonances, such as $\rho(770)$, in order to identify final states of well-defined angular momentum.

The $\rho\pi$ intermediate states are not CP eigenstates, but are CP self-conjugate collections of quarks $(u\overline{d})(\overline{u}d)$. Because of this, the modes $\rho^+\pi^-$ and $\rho^-\pi^+$ are expected to have amplitudes within a factor of two in magnitude (see table6-1, which is favourable for CP extraction. This introduces an eightfold ambiguity into the extraction of α [67]. It has been shown, however, that all but one of the mirror solutions can be lifted by considering the interference effects between the $\rho\pi$ modes in a full 3π Dalitz Plot analysis [68]. Such a detailed analysis requires a large sample of events, and will be feasible only after several years of data-taking. Fortunately, there are a number of simplified models which can

be investigated with smaller data sets, on a shorter time-scale, which can yield useful information in the interim. It is foreseen that several stages of development will take place, as data are accumulated:

1] establish the existence of CP violation in the 3π channel,
2] measure a value for α,
3] test consistency with the Standard Model predictions.

The main simplifying assumption one can make is that penguin contributions will be negligible. This reduces the number of parameters in the fit from 9 to 5. However, the value of α thus obtained differs from the true value by an unknown amount. It is hoped that improvements to theoretical models in the next few years will allow the relationship between this fitted α and the true α, due to penguin effects, to be better understood. If penguins turn out to be small, then this simplified analysis will be adequate. If penguins are large, then the extraction of α will be more involved, but the analysis becomes more compelling since large penguins are an indication of large direct CP violation effects.

Other areas which have been investigated, and will require further careful study with data, are the levels of background from the continuum, which can limit extraction of signal events, and the feasibility of using the $\rho^0\pi^0$ mode, which is expected to have a lower branching ratio than the charged $\rho\pi$ modes, due to colour-suppression.

The mechanism for CP violation in the interference between decay and mixing was introduced in Chapter 1 for the case of decays to a CP eigenstate (eqn 1.34). It is also possible to extract measurements of CP violating asymmetries from certain non-CP eigenstates (such as $\rho\pi$), although the method is more complicated. If the final states under consideration are f and $\overline{f}$, then there are four separate amplitudes for B^0 and $\overline{B}^0$ to decay to f and $\overline{f}$,

$$\begin{aligned} A(B^0 \to f) &\equiv A_f = |A_f| e^{i\theta_f} \\ A(\overline{B}^0 \to f) &\equiv \overline{\mathrm{A}}_f = |\overline{\mathrm{A}}_f| e^{i\overline{\theta}_f} \end{aligned}$$

$$\begin{aligned} A(B^0 \to \overline{f}) &\equiv A_{\overline{f}} = |A_{\overline{f}}| e^{i\theta_{\overline{f}}} \\ A(\overline{B}^0 \to \overline{f}) &\equiv \overline{\mathrm{A}}_{\overline{f}} = |\overline{\mathrm{A}}_{\overline{f}}| e^{i\bar{\theta}_{\overline{f}}} \end{aligned} \tag{6.1}$$

The rates for the physical, time-evolved $B^0_{\rm phys}(t)$ and $\overline{B}^0_{\rm phys}(t)$ states to decay into f can then be written [67]

$$\begin{aligned} \Gamma(B^0_{\rm phys}(t) \to f) &= e^{-\Gamma t} A^2 \times \\ &\quad \{1 + R\cos(\Delta m_B t) - D\sin(2\alpha - \Delta\delta)\sin(\Delta m_B t)\} \\ \Gamma(\overline{B}^0_{\rm phys}(t) \to f) &= e^{-\Gamma t} A^2 \times \\ &\quad \{1 - R\cos(\Delta m_B t) + D\sin(2\alpha - \Delta\delta)\sin(\Delta m_B t)\} \end{aligned} \tag{6.2}$$

where α is the CP phase and $\Delta\delta$ is the difference of the strong phases.

$$A^2 \equiv \frac{1}{2}\left(|A_f|^2 + |\overline{\mathrm{A}}_f|^2\right), \quad R \equiv \frac{|A_f|^2 - |\overline{\mathrm{A}}_f|^2}{|A_f|^2 + |\overline{\mathrm{A}}_f|^2}, \quad D \equiv 2\frac{|A_f||\overline{\mathrm{A}}_f|}{|A_f|^2 + |\overline{\mathrm{A}}_f|^2}. \tag{6.3}$$

Similarly, the rates for $B^0_{\rm phys}(t)$ and $\overline{B}^0_{\rm phys}(t)$ states to decay into $\overline{f}$ are

$$\begin{aligned} \Gamma(B^0_{\rm phys}(t) \to \overline{f}) &= e^{-\Gamma t} \overline{\mathrm{A}}^2 \times \\ &\quad \left\{1 + \overline{R}\cos(\Delta m_B t) - \overline{D}\sin(2\alpha + \Delta\delta)\sin(\Delta m_B t)\right\} \\ \Gamma(\overline{B}^0_{\rm phys}(t) \to \overline{f}) &= e^{-\Gamma t} \overline{\mathrm{A}}^2 \times \\ &\quad \left\{1 - \overline{R}\cos(\Delta m_B t) + \overline{D}\sin(2\alpha + \Delta\delta)\sin(\Delta m_B t)\right\} \end{aligned} \tag{6.4}$$

where

$$\overline{\mathrm{A}}^2 \equiv \frac{1}{2}\left(|A_{\overline{f}}|^2 + |\overline{\mathrm{A}}_{\overline{f}}|^2\right), \quad \overline{R} \equiv \frac{|A_{\overline{f}}|^2 - |\overline{\mathrm{A}}_{\overline{f}}|^2}{|A_{\overline{f}}|^2 + |\overline{\mathrm{A}}_{\overline{f}}|^2}, \quad \overline{D} \equiv 2\frac{|A_{\overline{f}}||\overline{\mathrm{A}}_{\overline{f}}|}{|A_{\overline{f}}|^2 + |\overline{\mathrm{A}}_{\overline{f}}|^2}. \tag{6.5}$$

The conservation of CP would require that the probabilities of CP conjugate processes were identical, which leads to,

$$|A_{\overline{f}}| = |\overline{\mathrm{A}}_f|, \quad |\overline{\mathrm{A}}_{\overline{f}}| = |A_f| \tag{6.6}$$

$$\sin(2\alpha - \Delta\delta) = \sin(2\alpha + \Delta\delta) \tag{6.7}$$

Therefore, if any of these equalities is not satisfied then CP violation is present. Equation 6.7 relates to the CP violation generated by the interference between decay and mixing.

Measurements of the time-dependent decay distributions can provide $\overline{S} \equiv \sin(2\alpha - \Delta\delta)$ and $S \equiv \sin(2\alpha + \Delta\delta)$, from which α can be extracted,

$$\sin^2 2\alpha = \frac{1}{2}\left[1 + S\overline{S} \pm \sqrt{(1-S^2)(1-\overline{S})^2}\right]. \quad (6.8)$$

6.3 Event Generation for Signal and Backgrounds

The simulated data sample for this analysis was generated using the package of Monte Carlo event generators available in the BABAR software, `EvtGen`, [69]. The features of the event generation for both signal and continuum events are described below, in order to provide a detailed account of the inputs to the fit.

6.3.1 Generation of CP Asymmetries

`EvtGen` introduces mixing by generating decays of the $\Upsilon(4S)$ to the proper mixture of $B^0\overline{B}^0$, $\overline{B}^0\overline{B}^0$, and B^0B^0 final states, with the correct distributions of Δt. In general, CP asymmetries are generated in modules which modify the generated lifetime distributions of the two Bs produced in the decay of the $\Upsilon(4S)$. One of the Bs then decays to the required CP mode, and currently, the generator assumes that the other B always provides a flavour tag. In the case of $B^0 \to \pi^+\pi^-\pi^0$, the additional complication of interference between resonances must be taken into account. In order to handle this, a special model was provided [69] which returns amplitudes incorporating the CP-violating phase present in the mixing.

6.3.2 The $B^0 \to \pi^+\pi^-\pi^0$ Monte Carlo Generator

B^0 decays into the $\pi^+\pi^-\pi^0$ final state were generated via several resonances : $\rho(770)$, $\rho(1450)$, $\rho(1700)$. This allowed the interferences between the different final states to

be included in the model (*e.g.*, $B^0 \to \pi^+\pi^-\pi^0$ via $\rho^+(770)\pi^-$ and $\rho^-(770)\pi^+$). The interference regions can provide useful information to the CP fit, which is essential for all but the pseudo-two-body analysis of this channel. The shape of the resonances was described using a relativistic Breit-Wigner function[1].

The Tree and Penguins amplitudes and phases for $B^0 \to 3\pi$, and $\overline{B}^0 \to 3\pi$ [2] were provided by the generator in order to calculate the kinematics of the generated final state. The strong phases were set to zero. A very low branching ratio is produced for the $\rho^0\pi^0$ due to colour-suppression [13]. The generator allowed two input parameters to be supplied, Δm and α. For the events used in this analysis, the values used as input to the fit were taken from [14]. These are summarised in table 6-2.

Table 6-2. *Values of physical quantities used in the 3π generator*

Input quantity	value
B^0 mass difference Δm	$0.474 \times 10^{12}\hbar s^{-1}$
B^0 lifetime τ_B	1.56×10^{-12} s
CP angle α	1.5207 rad (87.130°)
strong phase δ	0.0

The ρ-mediated $B^0 \to \pi^+\pi^-\pi^0$ amplitude is just the sum of amplitude terms for each ρ mode, which are weighted by the relevant functional form for the ρ. The shape of the ρ resonance, and the higher resonant contributions, is taken to be a relativistic Breit-Wigner, $f(s)$, and is a source of a systematic uncertainty in the analysis.

$$f(s) \propto \frac{\cos\theta_H}{s - m_\rho^2 + i\Pi(s)}, \tag{6.9}$$

where s is the square of the invariant mass of the putative ρ, and θ_H is the angle in the ρ rest frame between a decay pion direction and the line of flight of the ρ. The function Π

[1] using parameters fitted by Aleph with e^+e^- and $\tau^+\tau^-$ data, [70]

[2] computed by the LPTHE [13]

is given by [13]

$$\Pi(s) = \frac{m_\rho^2}{\sqrt{s}} \left(\frac{p}{p_0}\right)^3 \Gamma_\rho(m_\rho^2), \tag{6.10}$$

where $p = p(s) = \sqrt{s/4 - m_\pi^2}$ is the momentum of the daughter-pion in the ρ rest frame and p_0 is the momentum of the ρ candidate. In addition to the shape of the resonance, the angular dependence of the ρ decay is included in the f_i. The decay distribution is proportional to $\cos\theta_H$, as a consequence of a scalar particle, the B meson, decaying into a scalar, π, and a vector, ρ. Angular momentum conservation requires the ρ to have zero helicity.

The known phase variation over the Dalitz Plot introduced by the Breit-Wigner form provides the method for resolving the unknown phases in the amplitudes, which arise from both the weak interactions and the strong final state interactions.

6.3.3 Continuum Generation

Continuum events at the $\Upsilon(4\mathrm{S})$ were generated using `JETSET 7.4` ([71]) to fragment quark strings. The flavour of the primary string is given as the argument to the model (1: $d\overline{d}$, 2: $u\overline{u}$, 3: $s\overline{s}$, 4: $c\overline{c}$). A flavour of 0 represented a mixture of the quarks generated with the appropriate ratios. The first particle created was the virtual photon, which could then be decayed using this decay model. The primary jets were created according to a $1 + \cos^2\theta$ distribution in the e^+e^- rest frame, where θ is the angle of the primary jet with respect to the z-axis.

The total number of continuum events generated for the study is given in table 5-1. Following the event selection process described in the previous chapter, taking account of the expected relative production rates, the background/signal ratio was found to be 12.8. The inclusion of continuum background effects in the CP fitting process is discussed in the next section.

6.4 *CP* Fitting

CP fitting has been carried out to the Δz distribution for each of the four classes of events corresponding to different tag and $type$ combinations, where tag represents the charge on the b quark of the B^0_{CP}, and $type$ represents a $\rho^+\pi^-$ or a $\rho^-\pi^+$ event. The type selection was based on which of the reconstructed ρ candidates in the event had a mass closest to the nominal ρ mass. The shape of the Δz distribution for the signal is described by the time distribution for the decay rates of B^0 and $\overline{B}^0$ to f and $\overline{f}$, as given by equations 6.2 and 6.4, multiplied by a constant factor (given by equation 5.7). In order to correctly fit the data, this function has been modified to incorporate both background and detector effects [72], [73]. Additionally, the effect of charm decays has been taken into account. The development of the final fitting function is described below :

6.4.1 Effects from Charm Decays

It was shown in section 5.6.3 that the presence of charm decays from the B^0_{tag} in signal events contributes an exponential term to the Δz distribution which has a decay length equal to the charm decay length (when projected onto the z-axis),λ_C. Due to the lack of a clear correlation between any measurable quantity and the charm decay length on an event-by-event basis, it was decided to model the effect of charm using a single value of the decay length applied to every event. The Δz distribution described by equations 6.2 and 6.4 was convoluted with an exponential function, $\exp\frac{(-\Delta z}{\lambda_C)}$, where $\lambda_C = 30\,\mu\mathrm{m}$. In carrying out the convolution it was assumed that charm decays were always in the positive z direction with respect to the B^0_{tag} vertex.

The function resulting from this convolution is shown in Fig.6-1 for two cases, where (a) takes a value $\frac{\lambda_B}{\lambda_C}$ of 15, and (b) takes a value $\frac{\lambda_B}{\lambda_C}$ of 3. Δz has been scaled by $\beta\gamma\tau_B \sim 0.250\,\mathrm{mm}$, where τ_B is the nominal B^0 lifetime. When the charm lifetime is

significant, compared with the B lifetime, there is a considerable effect on the distribution, but within a small range close to the peak. In particular, it can be seen that when charm is taken into account in the fit, as described in section 5.6.3, then the asymmetry due to CP violation is not noticably affected by the charm contribution in the region of the B^0 lifetime (corresponding to the value 1 on the abscissa). This implies the significant finding that the CP reach is not degraded by the presence of charm (provided that the charm effect is handled correctly).

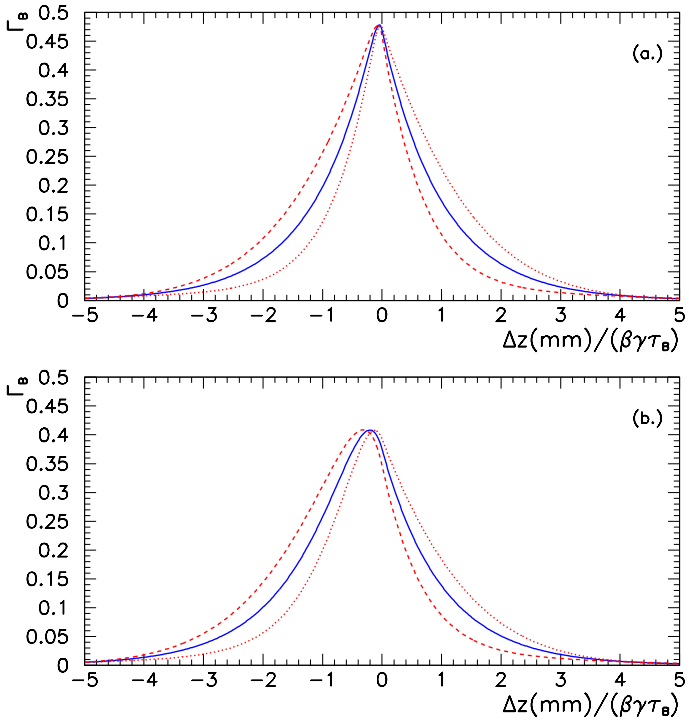

Figure 6-1. *The Δz distribution function convoluted with an exponential component, without CP violation (blue) and with CP violation (red, dotted line for positive asymmetry, dashed line for negative asymmetry); (a) shows the function when the charm effect is negligible, and (b) shows the effect of a significant charm component.*

6.4.2 Detector Resolution Effects

The finite resolution of the detector introduces a smearing of the actual Δz distribution. The overall level of the smearing can be estimated from a fit to the Δz resolution distribution, as shown in section 5.7. The multigaussian function provides a good fit to this distribution because it represents the summing of a set of single gaussians with a range of resolutions, and this corresponds to the set of events, where the Δz from each event has its own experimentally-determined resolution, $\sigma_{z(meas)}$. The measured value of Δz from each event then represents a sample from a gaussian distribution of resolution $\sigma_{z(meas)}$. Therefore, in order to handle the detector resolution correctly, the CP fitting function must be convoluted with a gaussian distribution with $\sigma = \sigma_{z(meas)}$, and the value of $\sigma_{z(meas)}$ is supplied to the function for each event along with the value of Δz.

6.4.3 Continuum Background Effects

In order to take into account the effects of background, a function is needed to describe the background distribution. However, the shape of the Δz distribution for the u, d, s continuum is less well understood than that for the signal. Both the B^0_{CP} and the B^0_{tag} vertex in u, d, s continuum events should have similar resolution, as there is no charm present. Since the events are highly jet-like, the resolution on the putative B candidate vertices depends on the angle of the thrust axis of the event with respect to the z-axis, *i.e.*, when all tracks are close to parallel with the z-axis then poor resolution is expected. In any case, for events with the thrust axis approximately colinear with the z-axis, the loss of tracks along the beampipe is likely to be high. The thrust axis direction features in some of the background rejection cuts using topological variables in the event selection process. While there may be some influence from these cuts on the shape of the resulting distribution, it is reasonable to assume that the Δz distribution for the u, d, s continuum can be approximately described by a single gaussian distribution for each event, since

there is no charm component. The distribution for $c\overline{c}$ continuum would of course need to include the exponential term representing charm decay. The σ for the gaussian is again supplied on an event-by-event basis by $\sigma_{z(meas)}$.

The fitting function is then modified to incorporate the form for the background with a weighting given by the expected background to signal ratio in the sample, w. Following the event selection process described in the previous chapter, the actual background to signal ratio in the sample was found to be 12.8. In a detailed analysis, the weighting factor should be floated as one of the fit variables.

$$\Delta z = (1 - w)\Delta z_{3\pi} + w\Delta z_{q\overline{q}} \tag{6.11}$$

6.4.4 The CP Fitting Function

To summarise the results of the previous sections, the final form of the fitting function is the convolution of equations 6.2 and 6.4 with an exponential function to represent the charm lifetime contribution, and a further convolution with a gaussian representing the detector resolution effects. This results in the three terms (constant, cosine and sine), which are illustrated in Fig.6-2, for a single value of $\sigma_{z(meas)}$, and tag and $type$ set equal to 1 (*i.e.*, the $\overline{B}^0 \to \rho^+\pi^-$ mode). The plots clearly demonstrate the asymmetry which is introduced by the sine term. The complete fit function to the full Δz distribution involves contributions from the experimental range of $\sigma_{z(meas)}$ values, and the four classes given by values of tag and $type$.

An example fit was carried out on a sample of 1760 events selected from $B^0 \to \pi^+\pi^-\pi^0$, $\overline{B}^0 \to X$ generated events according to event selection procedure described in the previous chapter. The size of the event sample corresponded to a canonical year of data-taking (*i.e.*, $30\,\text{fb}^{-1}$ luminosity). The parameters to be fitted were α and the ratio of the amplitudes, A_f and $A_{\overline{f}}$. The initial value of α was set to $1.5\,\text{rad}$, and the initial value of $(\frac{A_f}{A_{\overline{f}}})^2$ was taken as 4.53. The fit converged to a value of $\alpha = 1.75 \pm 0.10\,\text{rad}$, which corresponds

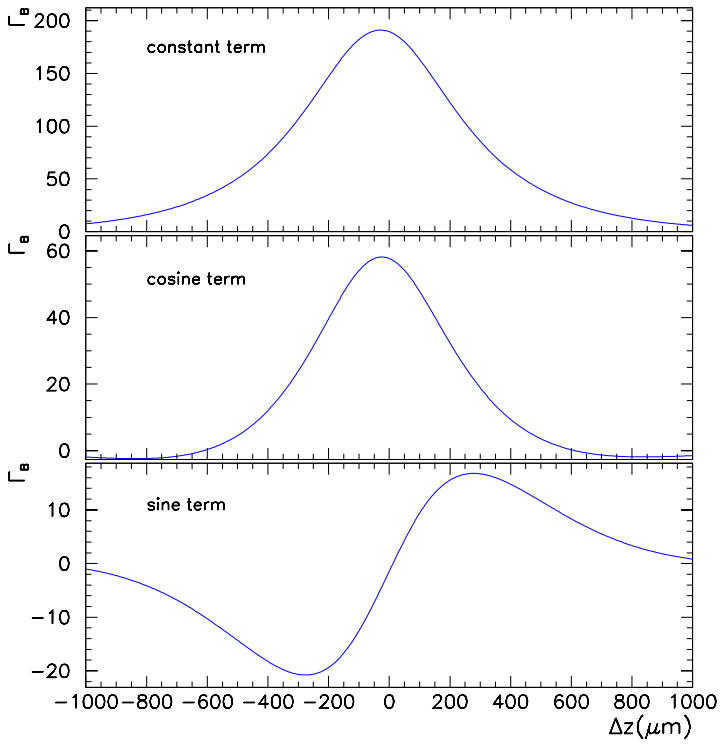

Figure 6-2. *The three terms of the Δz fitting function.*

to $\sin 2\alpha = -0.35^{+0.19}_{-0.02}$, and a value of $(\frac{A_f}{A_{\overline{f}}})^2 = 1.8 \pm 0.9$. While the problems of mirror solutions and the shift in the value of α remain in this example, due to the characteristics of the $\rho\pi$ analysis, it serves to demonstrate the principle of applying the fitting function which has been developed to the extraction of a CP asymmetry.

6.5 Summary

The formulation of a general fitting function for the extraction of CP asymmetry has been carried out. The function includes the treatment of charm decays from the B^0_{tag}, detector resolution effects, and the modelling of light quark continuum background. A sample fit has been applied to the 3π mode, using the simplified two-body analysis. While the

two-body analysis does not make full use of the information carried by the 3π Dalitz Plot, it provides a means of studying CP violation in this mode using less parameters than the full 3π treatment. It is therefore useful for early studies of this channel, when data is limited. Additionally, the two-body treatment may be all that is required, if penguin contributions turn out to be small, and other analyses of α modes revealed a preferred region for the value of α to identify the correct mirror solution. This simplified analysis also does not suffer from the model dependence which is introduced to the 3π analysis, *i.e.,* the establishment of a non-zero sine term using the above method would demonstrate in a model-independent way that CP violation is present in this decay mode.

Ultimately, the extraction of the CP angle α using the 3π channel will depend on actual branching ratios, the distribution of events in the Dalitz Plot, and the size of penguin contributions. The effectiveness of the event selection process will depend not only on the background suppression methods which have been considered here, but also on the levels of machine backgrounds, and their impact on the reconstruction of the B candidate.

7

Conclusions

The BABAR experiment is beginning a programme of CP violation studies in the B meson system. It is expected that the studies of a wide range of channels will yield measurements which will overconstrain the Unitarity Triangle, and thereby establish whether the current explanation of CP violation in the Standard Model is adequate.

In order to carry out this physics programme, BABAR needs to be able to reconstruct a wide range of exclusive final states. This places stringent requirements on the performance of the detector. In particular, the reconstruction of modes which include one or more π^0 s demand an electromagnetic calorimeter with excellent energy and position resolution. The CsI(Tl) crystals which form the calorimeter must therefore conform to high standards of quality, in both light uniformity and overall light output. In order to ensure that such standards were met, work was carried out on site with a CsI(Tl) crystal manufacturer to develop the new crystal growth techniques necessary for producing large CsI(Tl) crystals, and to define and maintain levels of quality control at all stages of the crystal production process.

While a number of experiments have the capability to measure the angle β of the Unitarity Triangle, via the $B^0 \to J/\psi K^0_S$ channel, BABAR is also sensitive to the modes related to the angle $\alpha$of the Unitarity Triangle, which is much less well-determined, and will be harder to measure. These modes include $B^0 \to \pi^+\pi^-$, $B^0 \to \pi^+\pi^-\pi^0$and $B^0 \to 4\pi$. The extraction of α from these modes is complicated by the presence of penguins, requiring a many parameter fit. In addition, the channels have low branching ratios, and suffer from a high level of background contamination from the $q\overline{q}$ continuum. The issue of suppressing

the background has been addressed, with respect to the $B^0 \to \pi^+\pi^-\pi^0$ channel, and techniques have been developed which demonstrate that the background can be effectively suppressed to a sufficient level. Nevertheless, it is anticipated that several years' data taking will be required before a full study of CP violation in this channel can be realised.

The feasibility of the $B^0 \to \pi^+\pi^-\pi^0$ study will ultimately depend on the number of events, and their distribution in phase space, which depends on a number of resonant contributions, and in particular the $\rho(770)$. The interference effects between the resonances, the strength of penguin contributions with respect to the trees, and the effects of background contamination are factors which will determine the extent to which a value of α can be extracted. This work has demonstrated that the $B^0 \to \pi^+\pi^-\pi^0$ mode provides one of the most promising opportunities for measuring α.

References

[1] J.H. Christenson, J.W.Cronin, V.L.Fitch, R.Turlay, *Phys. Rev. Lett.* 13, *pp*. 138, 1964

[2] Y. Nir and Helen R. Quinn, *Ann. Rev. Nucl. Part. Sci.* **42** (1992) *pp*. 211–250.

[3] J.L.Rosner, Present and Future Aspects of CP Violation, lectures presented at the VIII J.A.Swieca Summer School, Brazil, 1995

[4] R.D.Peccei, CP Violation and Baryogenesis, Int. Conf. on CP Violation, Blois, 1989

[5] A.D. Sakharov, ZhETF Pis. Red. 5 32; JETP Lett. 5, *pp*. 24, 1967

[6] H. Quinn, CP Violation, SLAC-PUB-95-7053, 1995

[7] M. Kobayashi and T. Maskawa, Prog. Theor. Phys. **49**, No. 2, *pp*. 652, 1973

[8] P.F. Harrison, Symmetry and Conservation, lectures presented for the University of London Postgraduate HEP Lecture Series, 1995

[9] C.Albajar *et al.,* (UA1 Collaboration), *Phys. Lett. B* 186, 247, 1987

[10] E.Fernanadez *et al.,* (MAC Collaboration), *Phys. Rev. Lett.* 51, 1022, 1983

[11] N.Lockyer *et al.,* (Mark II Collaboration), *Phys. Rev. Lett.* 51, 1316, 1983

[12] J.D.Richman, Heavy Quark Physics and CP Violation, Lectures at the Nato Advanced Study Institute, Les Houches, France, 1997

[13] The BABAR Physics Book: Physics at an Asymmetric B Factory, SLAC-R-504, ed. P.F. Harrison and H.R. Quinn (BABAR Collaboration), 1998

[14] R.M. Barnett *et al.,* Particle Data Group, *Phys. Rev. D* **54**, 1996

[15] L. Wolfenstein, *Ann. Rev. Nucl. Part. Sci.* **36** *pp*. 137

[16] N. Cabibbo, *Phys. Rev. Lett.* **10**, *pp*. 531, 1963

[17] H. Albrecht *et al.,* (ARGUS Collaboration), *Phys. Lett. B* **234**, *pp*. 409, 1990

[18] D.Besson (CLEO Collaboration), Lepton and Photon Interactions: XVI International Symposium, Ithaca, ed. P.Drell, D.Rubin, 1993

[19] A.Alavi-Harati *et al.,* (KTeV Collaboration), *Phys. Rev. Lett.* 83, 22, 1999

[20] (CDF Collaboration), A Measurement of $\sin(2\beta)$ from $B^0 \to J/\psi K^0_S$ with the CDF Detector, CDF/PUB/BOTTOM/CDF/4855, 1999

[21] QCD161 I92, *pp*. 93–6, 1988

[22] P.J. Oddone, in Proceedings of the UCLA workshop: Linear collider $b\overline{b}$ Factory Conceptual Design, *pp*. 423

[23] PEP–II, An Asymmetric B-Factory, *Conceptual Design Report*, SLAC-418/LBL-PUB-5379/CALT-68-1869/UCRL-ID-114055/UC-IRPA-93-01

[24] The Physics Program of a High Luminosity Asymmetric B Factory at SLAC, ed. D. Hitlin, SLAC-353/LBL-PUB-5245/CALT-68-1588, 1989

[25] BABAR *Letter of Intent*, ed. D. Hitlin, SLAC-443, 1994

[26] Proc. of Workshop on Physics and Detector Issues for a High Luminosity Asymmetric B Factory at SLAC, ed. D. Hitlin, SLAC-373/LBL-30097/CALT-68-1697, 1990

[27] B Factories: The State of the Art in Accelerators, Detectors and Physics, ed. D. Hitlin, SLAC-400, 1992

[28] BABAR *Technical Design Report*, ed. D. Hitlin, SLAC-R-95-457, 1995

[29] P.Franzini, J.Lee-Franzini, Upsilon Resonances, *Ann. Rev. Nucl. Part. Sci.* 33:1-29, 1983, e^+e^- Annihilation: New Quarks and Leptons, ed. R.N.Cahn, (Benjamin/Cummings Pub), 1985

[30] F.Forti, TRACKERR Studies for Optimization of Vertex Detector Resolution, BABAR *Note* # 195, 1994

[31] W.W.M. Allison and P.R.S. Wright, The Physics of Charged Particle Identification: $\mathrm{d}E/\mathrm{d}x$, Čerenkov and Transition Radiation, in Experimental Techniques in High Energy Physics, ed. T. Ferbel, Addison Wesley, 1987

[32] R. Barlow *et al.*, Results from the BABAR Electromagnetic Calorimeter Beam Test, BABAR *Note* # 367, 1997

[33] N. Dyce *et al.*, The BABAR Trigger Group, The BABAR Trigger System Design Requirements, V4.00, 1997

[34] G.F.Knoll, Radiation Detection and Measurement, 2^{ed}, Wiley, 1989

[35] G.Eigen, D.Hitlin, W.J.Wisniewski, Radiation Hardness Studies of Doped CsI Crystals, BABAR *Note* # 96, 1993

[36] G.Eigen, D.Hitlin, Radiation Hardness Studies of CsI Crystals, BABAR *Note* # 96, 1993

[37] Crystal Growth, B. Pamplin, Pergamon Press, 1975

[38] Introduction to Solid State Physics, C. Kittel, Wiley, 1971

[39] J.Brose, G.Dahlinger, P.Eckstein, K.Schubert, R. Seitz, CsI Crystal Uniformity Specification and Quality Control, BABAR *Note* # 175, 1995

[40] Zong-ying Wei, Ren-yuan Zhu, A Study on Undoped CsI Crystals, *Nucl. Instr. and Methods* , A326, 508-512, 1993

[41] S. Brandt *et al., Phys. Lett.* 12, 57, 1964; E.Fahri *Phys. Rev. Lett.* 39, 1587, 1977

[42] J.D.Bjorken and S.J.Brodsky, *Phys. Rev. D* 1, 1416, 1970

[43] G.C.Fox and S.Wolfram, Nucl. Phys. **B 149**, 413, 1979

[44] D.M. Asner *et al.,* Search for Exclusive Charmless Hadronic B Decays, *Phys. Rev. D* 53, 1039, 1996

[45] S.Versillé, C.Yèche, Cornelius User Guide, Tagging *Note* # 5, 1996

[46] S.Versillé, C.Yèche, Cornelius User Guide, Tagging *Note* # 5, 1996

[47] D.E.Jaffe, F.Le Diberder, M.H.Schune, Treatment of Weighted Events in a Likelihood Analysis of Oscillations or CP violation BABAR *Note* # 132, 1997

[48] A.Gaidot, C.Yèche, M.Zito, Linear Discriminant Analysis and Neural Network Approach for Babar Tagging Tagging *Note* # 7, 1997

[49] A.Gaidot, C.Yèche, Tagging Studies for BaBar Experiment using Leptons with an Artificial Neural Network Approach, Tagging *Note* # 3, 1996

[50] R.A.Fisher, Annals of Eugenics **7**, 179, 1936

[51] F.Le Diberder, S.Versillé, Estimating the Tagging Performances: the Separation, Tagging *Note* # 11, 1997

[52] Details of the structure of the BABAR offline software can be found in the BABAR Work-Book, http://www.slac.stanford.edu/BFROOT/www/doc/workbook/workbook.html

[53] T.J. Champion, Using BetaTools for Physics Analysis, BABAR *Note* # 424, 1990

[54] M.B.Wall, GAlib: A C++ Genetic Algorithms Library, MIT, 1995

[55] F.Le Diberder, S.Versillé, Cornelius Multi-Purpose Fitting Scheme, Tagging *Note* # 10, 1997

[56] E.Frank, B.Jacobsen , Architecture of the BABAR Reconstruction System, BABAR *Note* # 379, 1997

[57] Study of $B^0 \to J/\psi K^0_S$ and $B^0 \to \rho^{\pm}\pi^{\mp}$, P.F. Harrison, BABAR *Note* # 218, 1995

[58] P.D.Strother, Design and Application of the Reconstruction Software for the BABAR Calorimeter, PhD thesis, Imperial College, London, 1998

[59] J.Back, Track-Cluster Matching for the Electromagnetic Calorimeter using a Simple Model, BABAR *Note* # 439; BABAR *Note* # 440, 1998

[60] A.E. Snyder, The Effect of Vertex Cuts on CP Reach, BABAR *Note* # 177, 1994

[61] C.Dallapiccola, Primary Vertex Finder, presentation given at BABAR Physics Workshop, Caltech, 1997

[62] Multigaussian function provided from the ideas and work of G.Lynch and P.F.Harrison

[63] A.Salnikov, Kinematic Fitting in Aslund and Beta, presentation given at BABAR Physics Workshop, Orsay, 1997

[64] Penguin Trapping with Isospin Analysis and CP Asymmetries in B Decays H.J.Lipkin, Y.Nir, H.R.Quinn, A.E.Snyder, 1991

[65] R.Godang *et al.,* (CLEO Collaboration), *Phys. Rev. Lett.* 80, 3456, 1998

[66] Uncertainties on the CP Phase Alpha due to Penguin Diagrams, R.Aleksan, F.Buccella, A.Le Yaouanc, L.Oliver, O.Pene and J.C.Raynal, hep-ph/9506260, 1995

[67] R.Aleksan, I.Dunietz, B.Kayser and F.Le Diberder, CP Violation Using Non-CP Eigenstate Decays of Neutral B Mesons , *Nucl. Phys.* B 361 141-165, 1991

[68] A.E.Snyder, H.R.Quinn, Measuring CP Asymmetry in $B^0 \to \rho\pi$ Decays without Ambiguities, *Phys. Rev. D* 48 2139, 1993

[69] A.Ryd *et al.,* EvtGen : A Monte Carlo Generator for B Physics, 1998

[70] CERN-PPE:97013 (submitted to Zeitschrift fur Physik C).

[71] T. Sjöstrand, PYTHIA 5.7 and JETSET 7.4 Physics and Manual, JETSET 7.4, CERN-TH 7111/93, 1993

[72] Precision on CP Violation Measurements and Requirement on the Vertex Resolution, F.Le Diberder, BABAR *Note* # 34, 1990

[73] Parameterization of Decay Length Distributions with Errors, W.Toki, BABAR *Note* # 35, 1990

[74] D.H.Perkins, Introduction to High Energy Physics, (Addison-Wesley), 1997

A

Appendix A : The Dalitz Plot

The characteristics of the 3π Dalitz Plot are a central aspect of the study of the $B^0 \to \pi^+\pi^-\pi^0$ mode. Therefore, it is appropriate to describe in some detail the general features of the Dalitz Plot, and its value for three-body decay modes.

Decays with three-body final states exhibit a well-defined kinematic behaviour. In the rest frame of the decaying particle, of mass M, the three final state particles, i, j, k, are constrained to lie in a plane, so their momenta are completely specified up to three degrees of freedom. Defining the mass and four-momentum of particle i as m_i and p_i respectively, and similarly for j and k, then the quantities p_{ij} and m_{ij} can be formed,

$$p_{ij} = p_i + p_j \,, \tag{A.1}$$

$$m_{ij}^2 = p_{ij}^2 = M^2 + m_k^2 - 2ME_k \,, \tag{A.2}$$

where E_k is the energy of particle k in the M rest frame.

It can be shown [14] that the partial decay rate, $d\Gamma$, of a particle of mass M into three bodies in its rest frame is given in terms of the Lorentz-invariant matrix element $\mathcal{M}$ by,

$$d\Gamma = \frac{1}{(2\pi)^3}\frac{1}{32M^3}|\mathcal{M}|^2 dm_{ij}^2 dm_{jk}^2 \,. \tag{A.3}$$

For a given value of m_{ij}^2, m_{jk}^2 has a range of values between the limiting configurations of $\mathbf{p}_i$ parallel or anti-parallel to $\mathbf{p}_j$.

Two representations of the Dalitz Plot are presented, each having their own merits. The symmetry of the top plot, Fig.A-1, allows direct comparisons to be made between the

three ρ bands, and highlights the suppression of the $\rho^0\pi^0$ mode. The bottom plot, Fig.A-2, can be more easily interpreted in terms of the limits of the phase space [74], and is perhaps more applicable to decay modes where different particle types are present, such as the Kπ mode shown here.

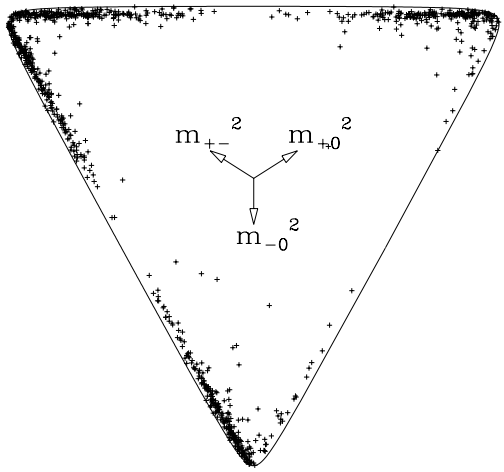

Figure A-1. *A Dalitz plot showing 1200 $B \to \rho\pi$ events, generated with the Small Penguins set of amplitudes. The $\rho^0\pi^0$ band is noticeably depleted. The events are concentrated at the ends of the ρ bands because of the longitudinal polarization of the ρ. [13]*

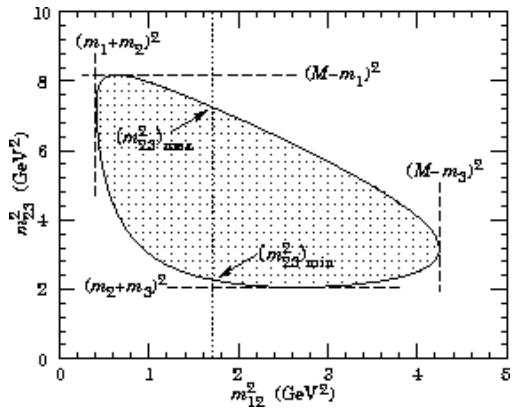

Figure A-2. *Dalitz Plot for the three-body final state $\overline{K^0}\pi^+p$ at 3 GeV. Four momentum conservation restricts events to within the boundary of the curve. [14]*